UNIVERSITÄT BAYREUTH

Lehrstuhl für Kristallographie

Structural aspects of pressure- and temperature-induced phase transitions in low-dimensional systems

Von der Universität Bayreuth
zur Erlangung des akademischen Grades eines
Doktors der Naturwissenschaften (Dr. rer. nat)
genehmigte Abhandlung

vorgelegt von
Maxim Bykov
aus Nowosibirsk, Russland

1. Gutachter: Prof. Dr. Sander van Smaalen
2. Gutachter: PD Dr. Karen Friese

Tag der Einreichung: 20.01.2015
Tag des Kolloquiums: 19.06.2015

Contents

Contents

Chapter 1

Introduction

Since the discovery of X-ray diffraction by Max von Laue in 1912 [1], this method became wide-spread among physicists, chemists, materials scientists, geologists, bio-chemists. The popularity of X-ray diffraction is related to the fact that it provides the comprehensive information about the crystal structures of materials, which in turn form the key to understand their physical and chemical properties. Solutions of crystal structures of DNA [2], proteins [3], ribosome [4] and high-temperature superconductors [5] have initiated breakthroughs in the corresponding scientific fields. During more than 100 years of X-ray diffraction many developments have been made to increase the range of available temperatures and pressures at which *in situ* diffraction experiments can be performed. So, in order to study the physics of superconductors an experimentalist has to cool the crystal down, while geologists may want to compress a mineral and heat it up to model the deep Earth interior conditions. Up to date, sample environments may vary in a range of $10^{-3} - 6 \cdot 10^3$ K and $10^{-12} - 6 \cdot 10^6$ bar [6–8].

This thesis reports on the investigation of low-dimensional systems MOCl (M = Sc, Ti, V, Cr, Fe) and $TiPO_4$ using single-crystal X-ray diffraction at non-ambient conditions. Transition metal oxychlorides MOCl are isostructural at ambient conditions. They crystallize in the FeOCl structure type with space group *Pmmn*. The structure of MOCl consists of double M–O layers separated from each other by bilayers of Cl atoms (Fig. 1.1). Studies of MOCl began with the report of Goldsztaub on the synthesis and the crystal structure of FeOCl in 1934 [9]. The systematic investigation of all MOCl systems was performed by Harald Schäfer in the 1950s [10–13]. He has found a way to produce and isolate pure MOCl compounds using chemical reactions between metal oxides and chlorides:

$$2TiCl_3 + TiO_2 \rightarrow 2TiOCl + TiCl_4, \tag{1.1}$$
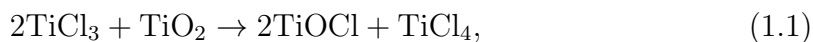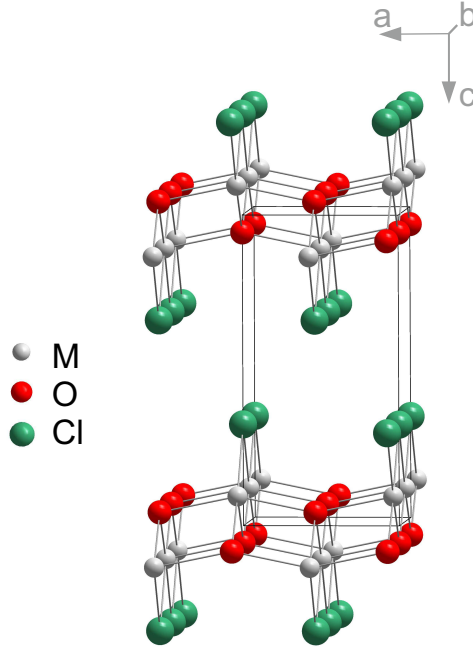
Figure 1.1: Crystal structure of MOCl at ambient conditions.

$$M_2O_3 + MCl_3 \rightarrow 3MOCl, \quad \text{for M = Cr, V, Fe.} \tag{1.2}$$

Later research was devoted to the improvement of synthetic techniques and to the investigation of magnetic properties of MOCl [14–18]. MOCl appeared to be good model systems for studies of the dependence of magnetic properties on the atomic magnetic moments of M^{3+} within a single structure type. FeOCl, CrOCl and VOCl reveal long-range antiferromagnetic order below 82.0, 13.5 and 80.3 K respectively [19–21]. At the same time TiOCl appeared to be different from other MOCl compounds, and its low-temperature behavior has been understood only in past ten years (see below). Another interest in MOCl compounds is related to the fact that their layered structure allows to intercalate various guest species like alkali metals, organometallic complexes or polymers in the interlayer space [22–28]. These investigations have been mainly restricted to FeOCl due to high oxidizing power of Fe^{3+}, which allows charge transfer mechanism of intercalation:

$$Fe^{3+} + nG \rightarrow Fe^{3+}_{1-n}Fe^{2+}_{n} + nG^+, \tag{1.3}$$

where G is a guest compound. Nevertheless, there are some studies of intercalated TiOCl, VOCl and CrOCl as well [18, 26, 29, 30]. Intercalated materials are of a potential use in lithium ion batteries [28, 31, 32] and may exhibit novel magnetic and electronic properties [24, 33].

5

A renewed interest in pure MOCl appeared immediately after Seidel et al. [34] have shown that TiOCl undergoes a spin-Peierls transition at a remarkably high temperature. Furthermore, unlike standard spin-Peierls systems, TiOCl undergoes two phase transitions: a normal-to-incommensurate transition at $T_{c2} = 90$ K and a lock-in transition at $T_{c1} = 67$ K towards a dimerized spin-Peierls state. Orbital order is responsible for the formation of quasi-one-dimensional spin chains in TiOCl. Each Ti atom is surrounded by four O and two Cl atoms forming a distorted octahedral environment. In a perfect octahedral environment the crystal field splits degenerate d orbitals into low-energy t_{2g} triplet and the higher energy e_g doublet. As was shown by Saha-Dasgupta et al. [35], in case of TiOCl, further splitting of the t_{2g} orbitals in a distorted octahedral environment leads to lower energy $d_{x^2-y^2}$ and higher energy d_{xz} and d_{yz} orbitals (the coordinate system has been chosen as $z \parallel \mathbf{a}$, $x \parallel \mathbf{b}$ and $y \parallel \mathbf{c}$). Therefore, in TiOCl, the degeneracy of the d-orbitals is completely removed, and the single d-electron of Ti^{3+} is located in the $d_{x^2-y^2}$ orbital. The $d_{x^2-y^2}$ orbitals form linear chains running along the $\mathbf{b}$-axis, linking Ti ions along these chains. Therefore, the exchange interaction between the electrons on neighboring Ti ions arises mainly from direct exchange. A detailed analysis of the low-temperature crystal structures of TiOCl has been performed by Shaz et al. [36] and Schönleber et al. [37]. Analysis of crystal structures allowed to attribute the origin of the incommensurate phase between 67 an 90 K to a frustration between spin-Peierls dimerization and elastic and magnetic interchain couplings.

The peculiar behavior of TiOCl has triggered reinvestigation of low-temperature phase diagrams of other MOCl compounds. MOCl (M = V, Cr, Fe) have more than one d-electron, and, hence, have strong magnetic interchain couplings. This does not allow a spin-Peierls state to develop. Recent temperature-dependent measurements on MOCl have shown that they possess monoclinic lattice distortions below T_N [19–21, 38], and new models of the low-temperature magnetic structures based on monoclinic symmetry have been developed [21, 39]. It was shown that anisotropic magnetic interactions, magnetic frustration and strong magneto-elastic coupling are responsible for a variety of complex magnetically ordered phases at low temperatures.

TiOCl is a Mott insulator with weak electron localization attributed to high nearest-neighbor exchange coupling. According to Goodenough [40, 41] an insulator-metal phase transition occurs when a critical metal-metal distance is reached. For Ti^{3+} the critical distance is 3.05 Å [42], and the shortest Ti–Ti distance in TiOCl at ambient conditions is 3.17 Å. Therefore, it was suggested that TiOCl is close to an insulator-metal transition and an application of pressure is an ideal tool to trigger

this transition [43], because it directly affects interatomic distances.

Initial high-pressure transmittance and reflectance measurements suggested that TiOCl undergoes an insulator-to-metal transition at ∼12 GPa [43]. Later Forthaus et al. [44] have performed electrical transport measurements and found that TiOCl does not transform to a metallic state, however there is a substantial change in the pressure-dependence of the band gap around 13 GPa. This indicated a change in the electronic structure of TiOCl. At the same time no structural changes were observed by means of energy-dispersive powder X-ray diffraction. Later Zhang et al. [45] have performed *ab initio* calculations and claimed two pressure-induced phase transitions to occur. The first transition leads to the two-dimensional metallic state with strong Ti–Ti dimerization. The dimerization is suppressed at the second transition, and TiOCl becomes a uniform metal.

The structural evidence for the first transition has been obtained by Kuntscher et al. [46]. Employing powder X-ray diffraction they have found additional reflections on the diffraction pattern above 15.5 GPa. However, no structural model has been proposed for the high-pressure phase. Later Blanco-Canosa et al. [47, 48] proposed that the high-pressure structure is a monoclinic $a \times 2b \times c$ superstructure with symmetry $P2_1/m$. A Rietveld refinement revealed formation of Ti–Ti dimers along the **b**-axis. Although the experiment results are supported by theoretical calculations, the accuracy of Rietveld refinement of TiOCl powders is rather questionable. Indeed, Ebad-Allah et al. [49] interpreted powder X-ray diffraction pattern of TiOCl in a different way. They suggested that above 15 GPa a mixture of ambient-pressure $Pmmn$ phase and a monoclinic $2a \times 2b \times c$ superstructure exists. Moreover, Ebad-Allah et al. have found a pronounced anomaly in all lattice parameters of the $2a \times 2b \times c$ superstructure and suggested that a second transition takes place at 22 GPa. However, no models were proposed for these high-pressure superstructures.

So, up to now no agreement has been obtained about a possible metallization of TiOCl at high pressures. Furthermore, no reliable structure models have been reported for high-pressure phases. The major reason for that is that it is not possible to produce good TiOCl powders for measurements in diamond anvil cells. Plate-like crystallites of TiOCl orient themselves to lie flat on the diamond culet, and, therefore the crystallographic **c**-axis become parallel to the primary X-ray beam. With that Rietveld refinements can't provide reliable results.

Some considerations about high-pressure behavior of TiOCl can be also applied to other MOCl, which are Mott insulators at ambient conditions and may undergo insulator-metal transitions at high pressures. Therefore, systematic investigation

of high-pressure behavior of MOCl is of great interest in order to understand the interplay between the number of d-electrons on the transition metal atom and phase diagrams of the compounds. No extensive high-pressure studies have been performed on MOCl other than on TiOCl so far. A single report is available on high-pressure behavior of polyaniline-intercalated FeOCl. It was shown that the charge transfer in polyaniline-intercalated FeOCl can be enhanced through the application of external pressure [27]. Therefore, studies of MOCl at high pressures may also bear relevance for the understanding of the stress properties of intercalated MOCl compounds.

The main goal of the work reported in this thesis is the characterization of the high-pressure phase diagrams of MOCl and the development of models for the mechanisms of the high-pressure phase transitions. For this purpose single-crystal X-ray diffraction in diamond anvil cells has been employed.

In Chapter 2 of this thesis a short introduction is given to the methodology of synchrotron X-ray diffraction experiments at non-ambient conditions.

Chapter 3 focuses on the procedure of processing of high-pressure single-crystal X-ray diffraction data using the computer program $CrysAlis^{Pro}$ [50].

It was believed for many years that on increasing pressure materials should adopt high-symmetry close-packed structures, however there are now many examples that complex superstructures or even incommensurately modulated structures may appear under compression [51]. Analysis of large superstructures is not a trivial task even if diffraction data are collected at ambient conditions. Additional restrictions on data completeness implied by the diamond-anvil-cell technique make conventional analysis of superstructures almost impossible. An elegant solution of this problem is to use the superspace approach [52]. Within this approach the superstructure may be interpreted as its basic structure with three-dimensional space group symmetry and a small unit cell, which is subjected to a periodic deformation. In Chapter 4 it is shown that the use of the superspace approach may help to overcome problems of data incompleteness which is inevitable for high-pressure diffraction experiments in diamond anvil cells, using high-pressure superstructures of FeOCl and CrOCl as examples.

Chapter 5 of this thesis is dedicated to the high-pressure behavior of FeOCl. Employing single-crystal X-ray diffraction it was shown that at $P \approx 15$ GPa a structural phase transition takes place. The transition is preceded by an extremely anisotropic lattice compression. The transition has been additionally investigated by Raman and Mössbauer spectroscopy techniques. The results of Mössbauer spectroscopy exclude magnetic order, while Raman spectroscopy indicates that the insulating behavior is retained at high pressures. The mechanism of the phase transition is
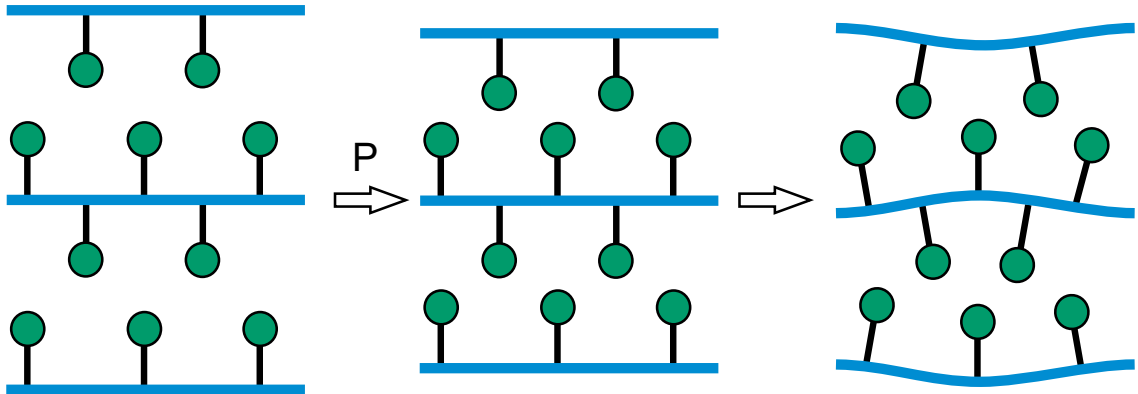
Figure 1.2: Schematic representation of the structural phase transition in MOCl (reproduced from Chapter 6).

related to an optimization of the packing of Cl atoms in the interlayer space and is not of electronic or magnetic origin. Therefore such transition type may be common for all MOCl compounds.

Chapter 6 reports the investigation of structural properties of CrOCl at high pressures. We have found that CrOCl undergoes a sequence of normal-incommensurate-commensurate phase transitions on compression. The distortions in the high-pressure structures of CrOCl are similar to those in FeOCl. We have estimated an empirical rule for the transition in MOCl. The transition occurs when interlayer $Cl\cdots Cl$ contacts reach the strongly repulsive region of the interatomic potential at $\sim$3 Å interatomic separation. At the same time intralayer $Cl\cdots Cl$ distance along $\mathbf{a}$ is determined by the geometry of the poorly compressible M–O bonds, and in all MOCl this distance is larger than twice Van der Waals radius of Cl. Therefore, there are voids within the structure, which allow Cl displacements along $\mathbf{a}$, and are used to prevent a considerable shortening of the interlayer $Cl\cdots Cl$ distances. Some voids are filled when neighboring Cl atoms move towards each other. Other voids are filled by Cl atoms of an adjacent slab when atoms neighboring along $\mathbf{a}$ move apart from each other (Fig. 1.2). A lock-in transition towards a six-fold $3a \times b \times 2c$ superstructure has been observed in CrOCl between 51 and 56 GPa. This superstructure coexists with a monoclinic $3a \times b \times 3c$ superstructure.

Chapter 7 describes the high-pressure behaviors of ScOCl, TiOCl and VOCl. In TiOCl an interplay between different structure distortions leads to extremely complex incommensurately modulated structures. Below 15 GPa enhancement of quasi-one-dimensional magnetism of TiOCl leads to the formation of the incommensurately modulated phase similar to the low-temperature incommensurate phase. Further increase of pressure leads to a structural phase transition as in FeOCl and
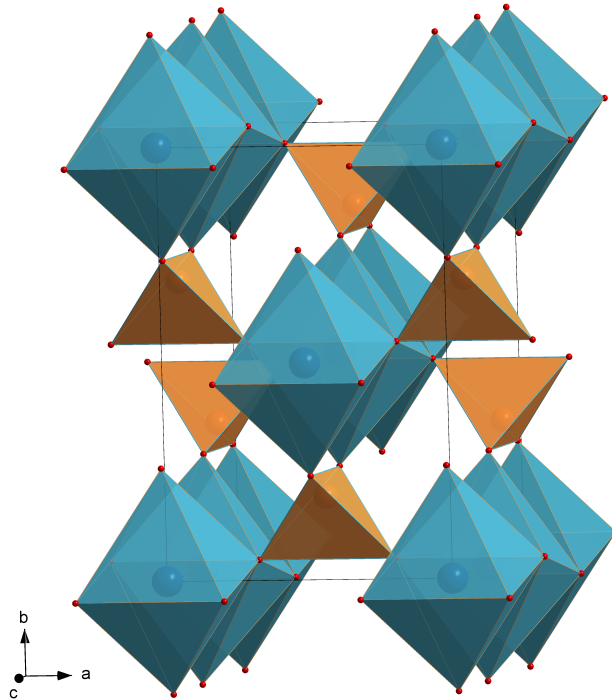
Figure 1.3: Crystal structure of TiPO$_4$ at ambient conditions.

in CrOCl, but now there is more than one distortion type: spin-Peierls-like distortion and slab buckling are present simultaneously. The structure model requires two modulation wave vectors for the description of atomic modulations. The high-pressure phase diagram of VOCl has been studied up to 50.5 GPa. Between 14.1 and 16.4 GPa it undergoes normal-to-incommensurate transition which is common for all MOCl. However, further compression leads to a transition to a $3a \times 3b \times 2c$ superstructure. The transition is accompanied by a volume drop, formation of triangular V clusters and interlayer V–Cl bonds. A phase transition in ScOCl towards a $6a \times b \times 2c$ superstructure has been detected at much lower pressure than the similar transition in other MOCl compounds. This allowed to improve the rule for the common transition for all MOCl, first described in the Chapter 6. Differences in high-pressure phase diagrams of MOCl are discussed in the Chapter 7.

Very recently Law et al. [53] have reported on the spin-Peierls state of TiPO$_4$ based on magnetic susceptibility, heat capacity, electron spin resonance and nuclear magnetic resonance techniques. The crystal structure of TiPO$_4$ at ambient conditions is presented on the Fig. 1.3. The major building blocks are distorted TiO$_6$ octahedra which share edges and build infinite chains along the **c** direction. These chains are interconnected by PO$_4$ tetrahedra. Law et al. have found that intrachain exchange interactions are much larger than interchain interactions. Thus, TiPO$_4$ is a

quasi-one-dimensional magnetic system and its low-temperature behavior appeared to be very much alike that of TiOCl. Two phase transitions have been detected at $T_{c2} = 111$ K and at $T_{c1} = 74$ K. Nevertheless, no structural proof of the spin-Peierls distortion could be obtained from in-house X-ray diffraction measurements.

Chapter 8 reports on the low-temperature single-crystal X-ray diffraction study of TiPO$_4$ using synchrotron radiation. A combination of the advantages of synchrotron radiation with advantages of point detector allowed us to detect very weak satellite reflections, which appear at low temperature and evidence the structural distortion. Crystal structure of TiPO$_4$ below T_{c1} appeared to be a $2a \times b \times c$ super-structure with symmetry *Pbnm*. The major structural distortion involves formation of Ti–Ti dimers within quasi-one-dimensional chains. The structure of TiPO$_4$ between T_{c1} and T_{c2} appeared to be incommensurately modulated. The incommensurate phase is ascribed to energetically almost degenerate phases resulting from a competition and frustration of the spin-Peierls transition due to elastic coupling between neighboring Ti chains.

Chapter 2

Experimental techniques

2.1 Sample environment

2.1.1 Closed-cycle He cryostat

For the single-crystal X-ray diffraction measurements at low temperatures (down to 10K) reported in this thesis (Chapter 8), a DE-202G cryostat from APD Cryogenics Inc. (SHI Cryogenics Group) was used. This cryostat is operated on a pneumatically driven two-stage Gifford-McMahon cycle [54]. The major components of the closed-cycle cryostat are the expander, compressor and vacuum shield. The expander (Fig. 2.1), where the refrigeration cycle takes place is connected to a compressor by high-pressure (supplying) and low-pressure (return) He gas lines. The Gifford-McMahon cycle consists of four steps [55]:

- The valve disk rotates and opens the high-pressure He gas inlet. The regenerators were cooled during the previous cycle, and cool the incoming He gas as it flows through.

- Pressure differential moves the displacer up, and creates an expansion space at the heat stations for gas that has passed through regenerators. While the displacer is moved up, the gas which didn't pass through regenerators is partially compressed and pushed into the surge volume.

- The valve disk rotates and opens the low-pressure gas return path. He gas expands in the expansion volume at the heat stations. This results in cooling of the heat stations.

- Cold He flows through the regenerating material and removes heat from it.

- As the pressure drops, partially compressed gas leaves the surge volume and
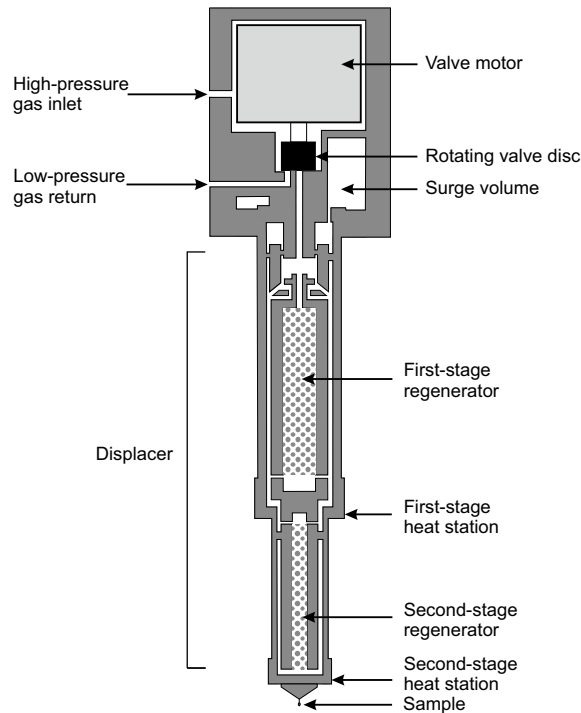
Figure 2.1: Simplified scheme of the closed-cycle He cryostat DE-202G. The figure is adapted from the user manual [55].

pushes the displacer down. The displacer moves down to its original position, and the valve closes.

The use of closed-cycle cryostat requires thermal conduction between the sample and the cold finger of the cryostat. Therefore, a conventional glass fiber support is not suitable. Instead, a crystal is glued to a carbon fiber that is attached to a copper pin. This pin is then attached to the second-stage heat station of the cryostat (Fig. 2.1). In order to prevent the formation of ice around the crystal and to reduce temperature gradients between the parts of the displacer, two beryllium domes are used. Vacuum is maintained in the areas between outer and inner domes as well as between the second stage heat station and the inner dome.

The closed-cycle cryostat has several significant advantages over open-flow He cryostats. First of all, it does not require continuous He supply. Secondly, it provides more precise temperature control at low temperatures, and does not suffer from gas turbulence problems. Among the disadvantages is that X-ray diffraction measurements suffer from Be diffraction rings, and it is almost impossible to use area detectors for such measurements. Another problem is that Be domes do not allow to observe the sample optically. This implies limitations on precise crystal centering,
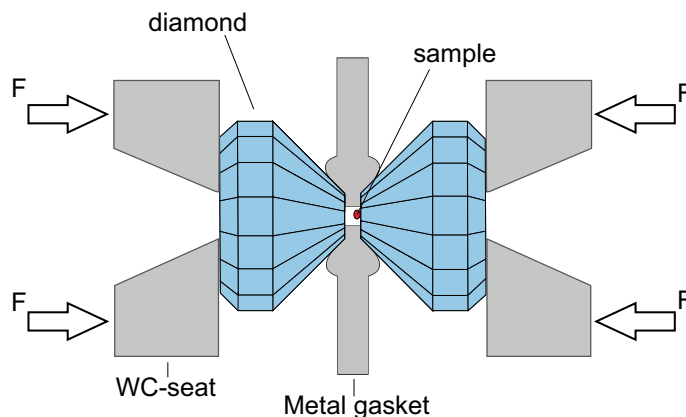
Figure 2.2: A principle of DAC construction. The figure is adapted from [57].

.

due to the shrinkage of some parts of the cryostat subjected to low temperatures (see section 2.2.2). Furthermore, the bulky construction of the cryostat significantly restricts the movements of the diffractometer axes, and hence, reduces the coverage of the reciprocal space. That is a crucial limitation in case of low-symmetry crystals, while for high-symmetry crystals this limitation mainly reduces the data redundancy.

2.1.2 Diamond anvil cell

A diamond anvil cell (DAC) is a device used to generate very high static pressures in the range 0.1–640 GPa [56]. A modern DAC consists of two opposing diamonds, which are driven towards each other by external force, and compress a sample between the culets (Fig. 2.2).

According to the most simple definition of pressure ($P = \frac{F}{S}$, where F is the applied normal force, and S is the area, to which the force is applied), there are two ways of reaching very high pressures. The first option is to increase the applied force, and the second is to decrease the area, to which the force is applied. The maximum force that can be applied is restricted by the mechanical strength of diamonds and seats, therefore in order to achieve extremely high pressures one should apply a moderate force (usually only several kN [58]) to a small area.

Nowadays diamonds with 500 μm and 250 μm culet diameters are exploited for routine measurements up to ~20 and ~80 GPa respectively. Ultra-high-pressure experiments require much smaller culet and sample size, that makes it necessary to use a unique equipment and synchrotron radiation. The highest static pressure in DACs (640 GPa) was recently achieved by the use of secondary diamond anvils [8].
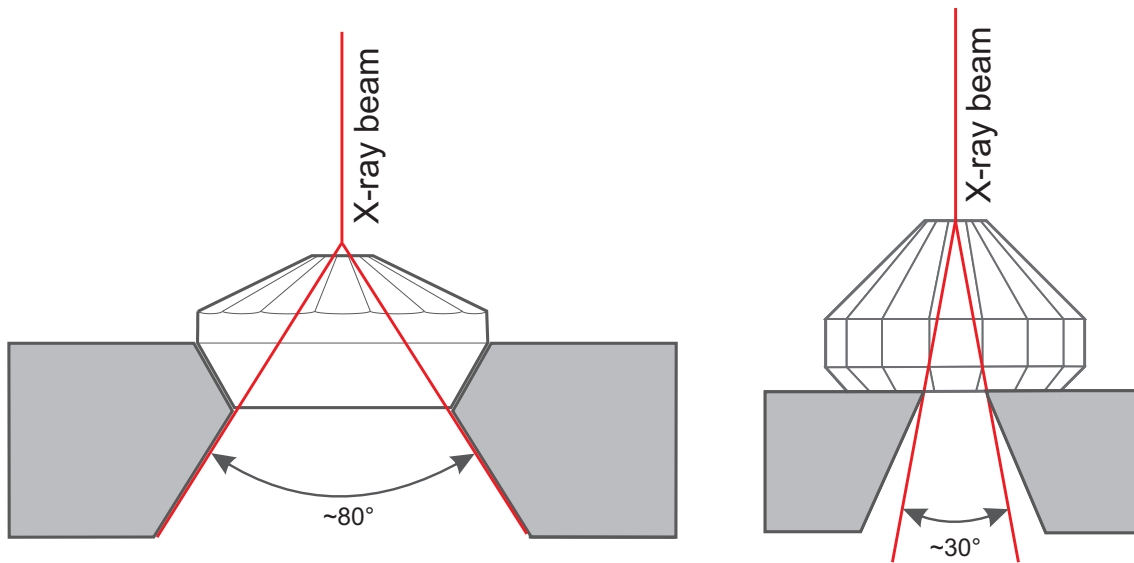
Figure 2.3: Comparison between Boehler-Almax (left) and normal-cut diamonds (right).
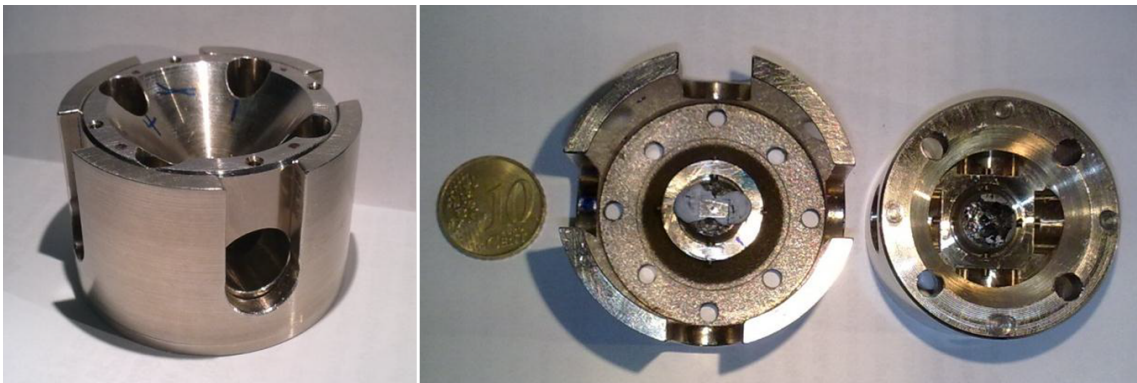
Figure 2.4: A photo of a BX90 diamond anvil cell.

Two types of diamonds were used for the experiments reported in this thesis. For single-crystal X-ray diffraction measurements Boehler-Almax type diamonds [59] were used. The main advantage of this design is a large opening angle of the DAC ($4\theta \sim 80°$), which allows the measurement of single-crystal X-ray diffraction up to high resolution. For Raman and Mössbauer spectroscopy measurements, a wide opening angle is not essential, so cheaper normal-cut diamonds may be used for these techniques (Fig. 2.3). Diamonds were glued by a super glue to the tungsten carbide seats, and placed into the BX90 diamond anvil cells [60] (Fig. 2.4).

2.2 Synchrotron radiation X-ray diffraction

All diffraction experiments reported in this thesis were performed with synchrotron radiation (SR) at beamlines D3 (Doris, DESY, Hamburg, Germany), P02.2 (Petra III, Hamburg, Germany), ID09A (ESRF, Grenoble, France) and 13IDD (APS, Argonne, USA). The choice of SR was dictated by its notable advantages over in-house X-ray sources. First of all, X-rays produced by a synchrotron are several orders of magnitude brighter than the X-rays from a sealed tube or a rotating anode source. It is crucial in case of weak diffraction data, typical, for example, for satellite reflections in incommensurately modulated structures (see Chapter 8) or for high-pressure experiments which usually require small sample volumes (Chapters 4, 5, 6). Secondly, SR provides an opportunity to choose a wavelength, that is most suitable for a certain application. So, for high-pressure diffraction one would prefer harder X-rays in order to collect more complete data, while for macromolecular crystallography longer wavelengths are used in order to avoid overlaps of diffracted peaks on the detector. Furthermore, variation of wavelength may be used to minimize crystal absorbtion and radiation damage. Finally, synchrotron X-ray beams can be well conditioned. So, a perfect parallel beam as well as a microfocused beam can be obtained.

2.2.1 High-pressure X-ray diffraction

In a typical high-pressure experiment a specimen in a form of a single crystal or powder and a pressure sensor are placed inside the hole in the preindented Re gasket, which was in advance attached to one of the diamonds by plasticine. Then the whole DAC is placed inside a chamber, which is then filled with Ne to a pressure of about 0.2 GPa. After that the DAC is closed by tightening of four screws, resulting in initial pressure in the range $1 - 5$ GPa [61].

Pressure in the DAC chamber can be determined by several optical and diffraction methods. One of the most convenient pressure indicator is ruby (Cr - doped Al_2O_3). In 1972 Forman et al. [62] have noticed that that the shift of ruby fluorescence lines with pressure can be effectively used for rapid pressure determination. Online ruby fluorescence systems are available at all high-pressure synchrotron stations and allow monitoring of the pressure without unmounting of the DAC from the experimental stage during the diffraction experiment. For all pressure measurements employing ruby fluorescence reported in this thesis, we have used the calibration made by Mao et al. [63] which is implemented in web-based tool available at http://kantor.50webs.com/ruby.htm.
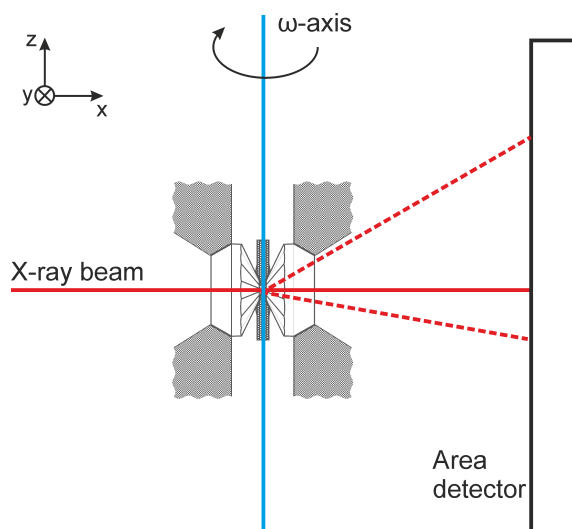
Figure 2.5: A scheme of the diffraction experiment in a diamond anvil cell.

Alternatively, pressure can be determined using the equation of state of Au (was used for powder XRD in Chapter 5) or Ne [64] (was used as a complementary pressure indicator at pressures above 15 GPa). In this way the unit-cell volumes of Au and Ne are determined from X-ray diffraction data, and are used in pressure calculations.

Among XRD experiments, two types may be distinguished: single-crystal and powder XRD. The use of powder simplifies the equipment required for the experiment. For example, no DAC rotation is necessary during the data collection. This increases the stability of the system and allows relatively easy combination of the DAC technique with bulky laser-heating systems or cryostats for temperature variation. The result of a powder XRD experiment is a two-dimensional Debye-Scherrer pattern, which is then integrated to provide a standard intensity versus 2θ ($I - 2\theta$) profile. These profiles may be suitable for lattice parameters determination and structure refinement, while *ab initio* structure solution is not a trivial task. Although there are plenty of studies, where high-pressure structures of materials were discovered by means of powder XRD, in many cases the interpretation of powder diffraction data is ambiguous. Nevertheless, powder XRD is the convenient technique for high-pressure studies of materials, exhibiting no phase transitions on compression. In case good quality single crystals of the material of interest can be obtained, single-crystal XRD is the method of choice for high-pressure studies. The resulting diffraction data are three-dimensional and do not suffer from problems typical for powder data [65].

A typical high-pressure X-ray diffraction experiment is performed as follows:
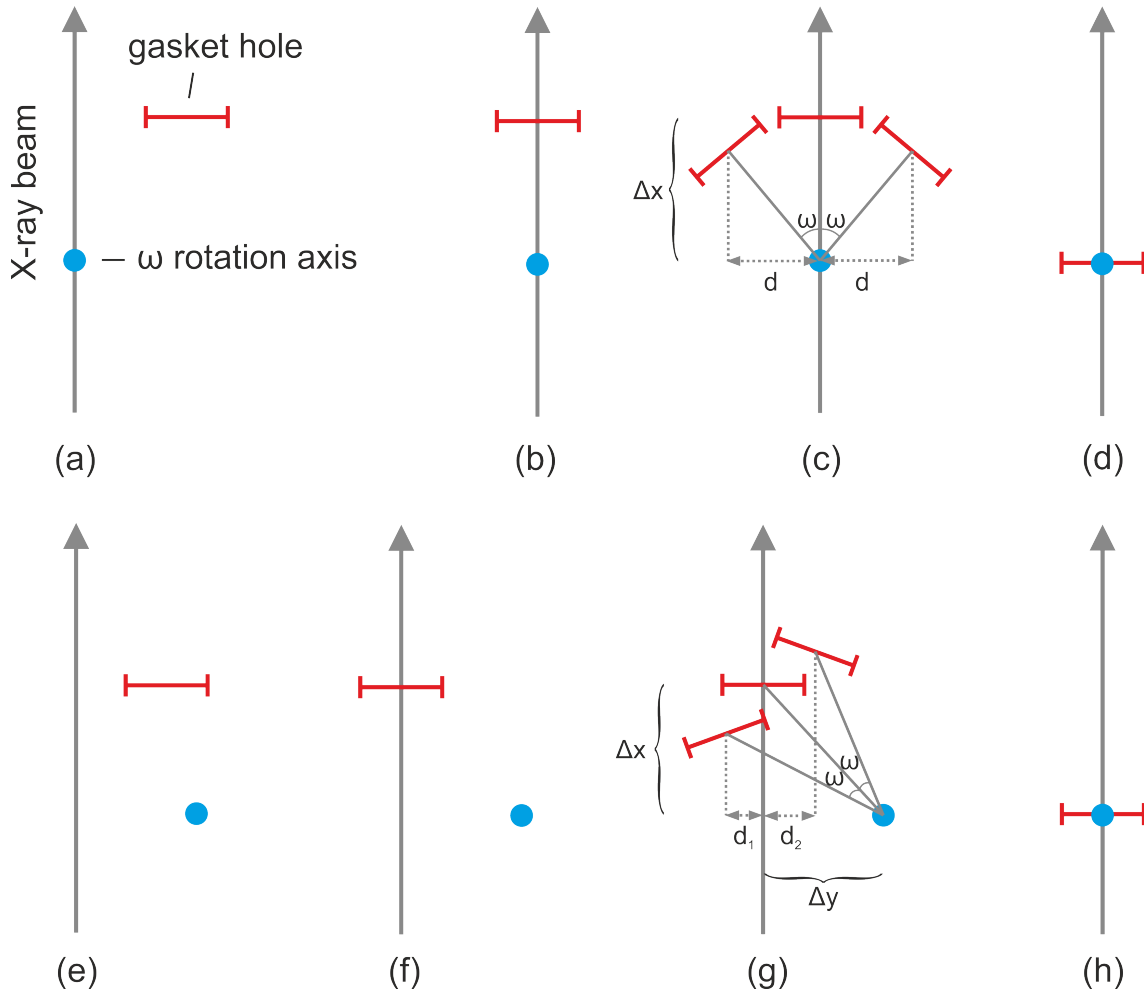
Figure 2.6: Typical process of sample centering shown in the projection along the vertical (z) axis. (a) initial state: gasket hole is away from the primary beam and from the ω rotation axis. (b) After several scans in the plane perpendicular to the primary beam direction the gasket hole is aligned with the beam. (c) DAC is rotated around the ω axis. Two horizontal scans are performed in order to determine the distance between the centers of the gasket hole at different ω positions. (d) The gasket hole is aligned with the primary beam and with the ω axis. (e) Second possible initial state: both gasket hole and ω axis are away from the primary beam. (f) After several scans in the plane perpendicular to the primary beam direction the gasket hole is aligned with the beam. ω axis is away from the beam. (g) DAC is rotated around the ω axis. Two horizontal scans are performed in order to determine the distance between the centers of the gasket hole at different ω positions. (h) The gasket hole is aligned with the primary beam and with the ω axis. ω axis is aligned with the beam.

18

- A DAC is placed on the sample positioning stack that has a motor, providing vertical translation, and two sets of motors providing horizontal translations above and below the ω rotation motor. The coordinate system is usually chosen as follows: $\mathbf{x}$ is parallel to the primary beam, $\mathbf{z}$ is a vertical axis and $\mathbf{y}$ is perpendicular to the $\mathbf{xz}$ plane (Fig. 2.5). The lower set of $\mathbf{xy}$ motors is used to bring the ω-axis to the intersection with the primary beam. The upper set of $\mathbf{xy}$ motors is used to bring the sample to the ω-axis.

- The sample is aligned in the X-ray beam by scanning the gasket hole in the plane normal to the X-ray path (Fig. 2.6). For that a semiconductor X-ray detector is placed between the DAC and the beamstop. Thus, if the primary beam coincides with the gasket hole, there will be noticeable intensity coming out of the DAC, while if the primary beam hits the gasket, it will be almost completely absorbed. A typical scan is presented in the Fig. 2.7.

  Alignment along the X-ray beam direction is performed by scanning the sample in horizontal direction at two different ω positions (Fig. 2.6(c)). From these scans the distance between the centers of the gasket hole at different ω positions ($2d$) can be calculated. Therefore, the correction that must be applied can be calculated using the formula $\Delta x_{\text{high}} = d/\sin\omega$ (subscript "high" means that the correction should be applied using the $\mathbf{x}$-translation motor above the ω motor).

  In case the ω axis is initially not aligned with the primary beam (Fig. 2.6(e)), additional corrections must be applied to bring the ω axis to the primary beam (Fig. 2.6(f)) using the horizontal motor below the ω-axis. In this case $\Delta x_{\text{high}} = \frac{d_1 + d_2}{2\sin\omega}$, $\Delta y_{\text{low}} = \frac{d_2 - d_1}{4\sin^2\frac{\omega}{2}}$ and $\Delta y_{\text{high}} = -\Delta y_{\text{low}}$.

- Usually the sample is placed in the center of the gasket hole, so that the centering of the gasket hole implies the centering of the crystal. If the crystal is well absorbing, its exact position can be established from the DAC scan (Fig. 2.7(b)), but for weakly absorbing crystals (like thin platelike crystals of MOCl (M = Sc, Ti, V, Cr, Fe) studied in this thesis) this procedure doesn't work very well (Fig. 2.7(c)). In this case an experimentalist must determine the offset of the crystal from the center of the gasket hole using an optical microscope, and then apply this correction after centering of the gasket hole.

- A wide omega scan ($\Delta\omega \approx 40°$) is performed. Diffracted intensities are analyzed in order to adjust the correct exposure time/filter/primary beam intensity for the data collection.

- Finally, a data collection is performed (Fig. 2.5). A series of frames is collected
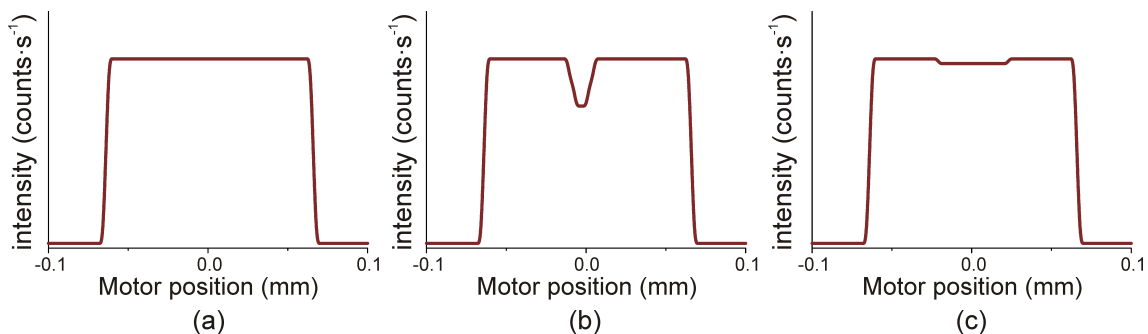
Figure 2.7: Schematic reproduction of typical DAC scans in the plane perpendicular to the primary X-ray beam. (a) Empty cell or very weak absorbing crystal. (b) Strong absorber. (c) Weak absorber.

with typical $\Delta\omega = 0.5 - 1°$ covering the total range of 80°. In order to increase the coverage of the reciprocal space a second data set can be collected with the DAC rotated around the primary beam direction by 90°.

2.2.2   Low-temperature X-ray diffraction

For low-temperature XRD experiments (Chapter 8) the closed-cycle He cryostat is mounted on the ϕ-axis of a four-circle Huber diffractometer equipped with a point detector. The orientation matrix of the crystal is determined before mounting the Be domes. For that, an image plate is used to record a two-dimensional image of the diffracted intensities from a wide ϕ scan. From this image, χ, ω and 2θ angles of several strong reflections can be calculated, and the ϕ angle is then determined from the wide ϕ scan at given positions of other angles using a point detector. After the positions of several strong reflections (usually at low 2θ values) are determined, one can find the preliminary orientation matrix. Once the orientation matrix is determined, it is possible to determine the positions of a number of strong reflections at higher 2θ values and to improve the precision of the orientation matrix and lattice parameters. Unfortunately, the experimental setup with a bulky cryostat doesn't allow to measure each reflection at several positions for precise lattice parameters refinement [66]. The next step is the mounting of two beryllium domes on the cryostat and pumping air out of the system to prevent heat transfer from the atmosphere to the crystal. After a good vacuum is reached ($\sim 10^{-5}$ mbar) cooling can be started.

In order to prevent radiation scattered by the Be domes to reach the detector, a detector collimator is used. It is a tube, that is mounted in front of the detector and allows to exclusively detect sample peaks (Fig. 2.8). However, at angles $2\theta < 13°$,
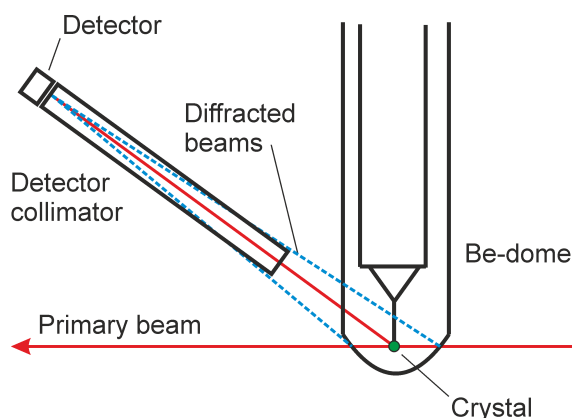
Figure 2.8: A simplified scheme of X-ray diffraction from a crystal and from a Be dome (only one Be dome is shown). Note that the X-ray beams diffracted from the Be dome (shown as dashed lines) don't reach the detector.

there is a significant increase of the background defined by diffraction from beryllium domes [67]. Another problem arises from the impossibility to center the crystal optically in the X-ray beam, when the crystal is cooled. The crystal is centered at ambient conditions when the Be domes are not mounted. Cooling induces the shrinkage of some parts of copper sample holder adapter and of a copper pin, and results in the moving the crystal away from the beam. A height correction, therefore, must be applied based on empirical knowledge from previous experiments.

Chapter 3

Single-crystal high-pressure X-ray diffraction: data processing

It is known that X-ray diffraction of crystals loaded in DACs suffers from shadows imposed by the DAC, strong diamond peaks, secondary diffraction effects (when the beam diffracted by the diamond hits the gasket), and diffraction from the pressure-transmitting medium (Fig. 3.1). Therefore, default procedures of data processing may often fail to produce reliable intensities of Bragg reflections. This chapter describes general procedures and the theoretical background for the analysis of high-pressure X-ray diffraction data using the $CrysAlis^{Pro}$ software package [50].

3.1 Image formats and their conversion

All high-pressure single-crystal X-ray diffraction data reported in this thesis have been obtained using synchrotron radiation at ID09A (ESRF, Grenoble, France) or P02.2 (DESY, PETRAIII, Hamburg, Germany). Single-crystal X-ray diffraction in DACs at synchrotrons is not standardized with respect to the software for beamline control as well as to detector systems. So, at ID09A a Mar555 flat panel detector is exploited, while at P02.2 a Perkin Elmer XRD 1621 flat panel detector is used. Both detectors are relatively modern and are not commonly used for routine in-house X-ray diffraction experiments. Therefore, the images they produce are not directly supported by the available data integration software.

$CrysAlis^{Pro}$ is the software package designed for Xcalibur/SuperNova X-ray systems and allows both instrument control and data analysis for these systems. With growing popularity of $CrysAlis^{Pro}$ many external detector frames formats were implemented (e.g. Mar, Dectris, Rigaku and Bruker detector images). In
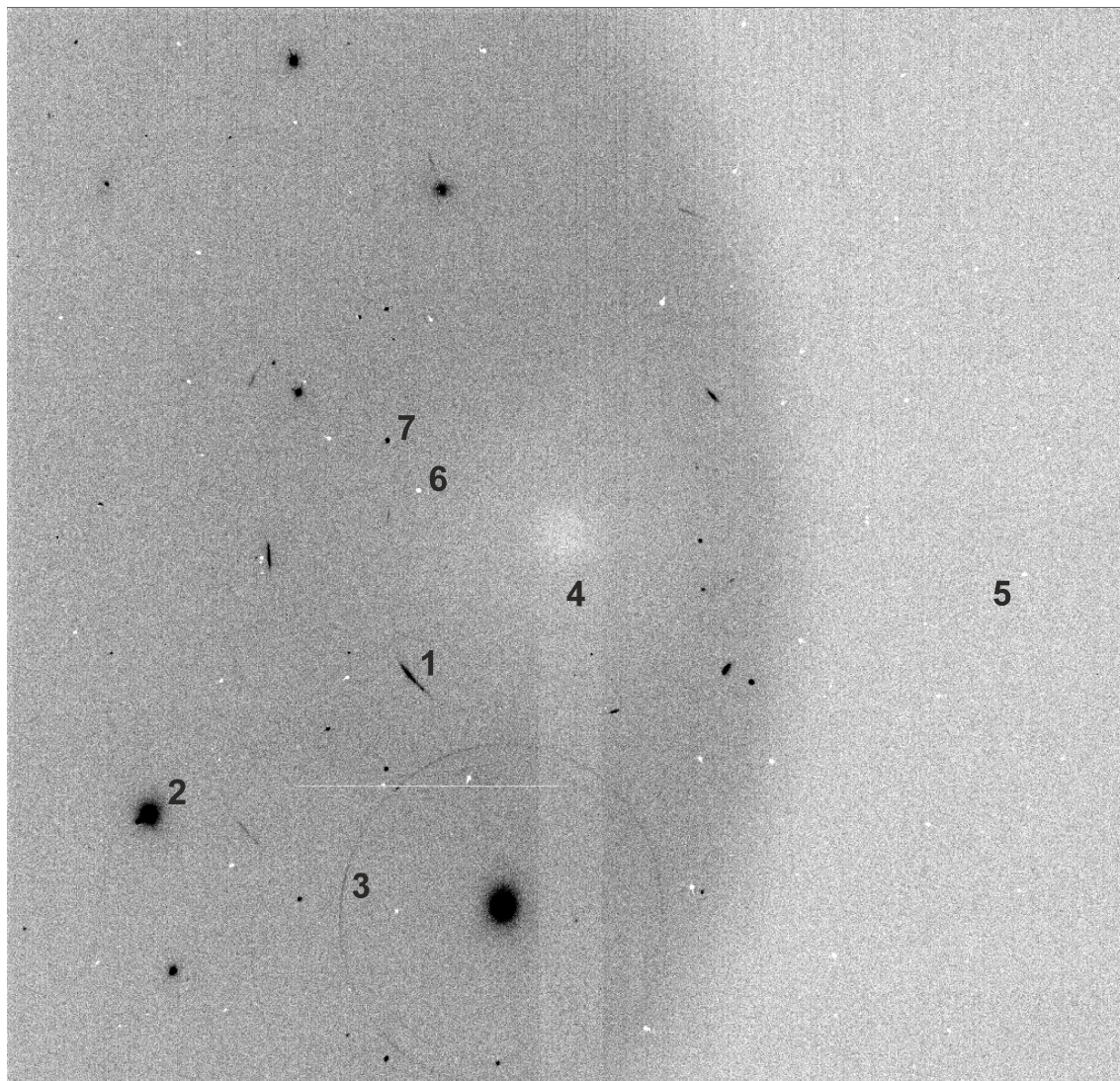
Figure 3.1: Typical X-ray diffraction image from a crystal loaded in a DAC. 1 - Diffraction line from the pressure-transmitting medium. 2 - diamond reflection 3 - secondary diffraction from the gasket or DAC body. 4 - beamstop shadow. 5 - region shaded by the DAC body. 6 - regions of reduced intensity, which appeared due to the ineffective detector cleaning from extremely overexposed peaks on previous images. 7 - sample diffraction peak.

this section, the procedures for the treatment of .mar2560 and .tiff images from the detectors installed at ID09A and P02.2 will be considered. The principal task is that the detector local coordinate systems must be appropriately transformed in order to match the $CrysAlis^{Pro}$ conventions for relations between laboratory and detector coordinate systems. Depending on the geometry of the diffraction experiment this may require various rotations or reflections of the recorded images.

Mar555 images (.mar2560)

The Mar555 flat panel detector installed at ID09A produces raw detector images in .mar2560 format, that have to be converted by the computer program $MAR555$ into .mar3450 images. The information for the transformation must be given in the MAR555.cfg file, an example of which is shown here:

```
# 2560       - Dimension X
# 3072       - Dimension Y
# 3450       - MAR format modifier
# crocl_p6_2 - file name template
# 80         - number of input files
# 1          - starting from number
# 140        - starting angle
# 1          - oscillation size in degrees
```

Converted images have .mar3450 format supported by $CrysAlis^{Pro}$. The dialog for quick generation of all necessary files for further data processing can be invoked from the $CrysAlis^{Pro}$ command shell (CMD) by typing **mar experimentsetup** in the command line (Fig. 3.2). First, one needs to specify first and last images of the run being imported. Detector distance, beam origin and wavelength can be modified here or on further steps. In the **Experiment interpretation** section choose **User settings**, **Monochromator/Polarisation: Polarisation= 1**, and **Image rotation:+90**. After clicking **Ok**, a list of available experiments appears.

A known bug in the $CrysAlis^{Pro}$ importer is that it does not set correctly the pixel size and the type of image rotation for frames converted by $MAR555$. So, **before** opening the newly created experiment file, one has to modify these parameters in marip.ini file located in the experiment directory.

```
PIXELSIZE          = 0.139
TYPEOFIMAGEROTATION = 3
```

After the modification is completed, the experiment can be opened. First step now is to import instrument model parameters from the .par file of the calibration
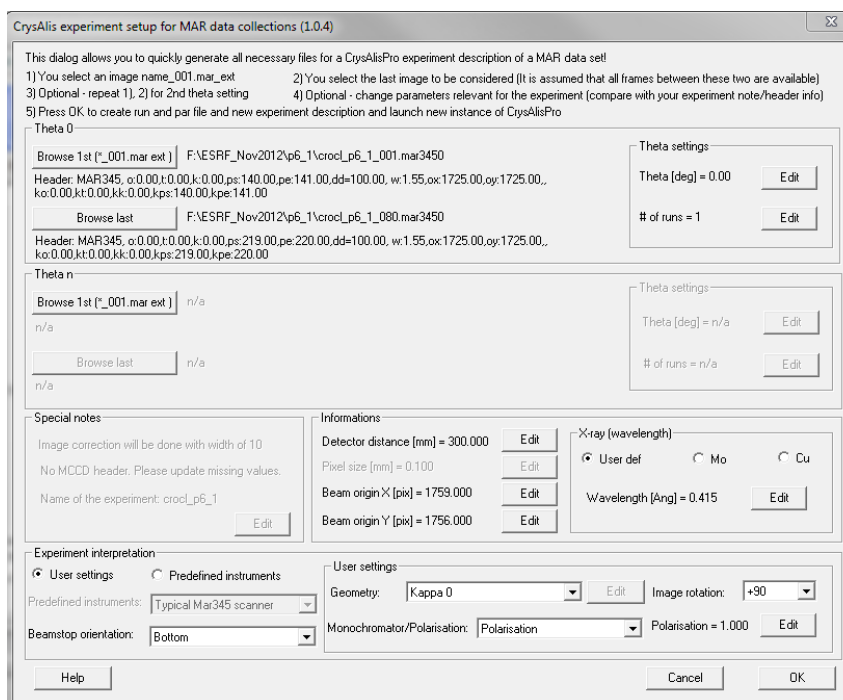
Figure 3.2: *CrysAlis* experiment setup for MAR data collections.

crystal. Type **rd p** in the shell command window, and select necessary .par file. Alternatively, the parameters can be defined in **CrysAlis RED program options** menu, which is activated by clicking the button **Options RED** in the CMD.

The *MAR555* program transforms .mar2560 images by extending its pixel dimensions from 2560×3072 to 3450×3450 by appending missing pixels with zero intensities. In order to exclude these dummy pixels from the analysis a command **dc rejectrect x0 y0 xw yw** should be used. It defines a rectangle area with coordinates of the lower left corner (x0, y0) and sides lengths given by xw and yw. This area will be omitted from the data integration process. An example of such rejection is given here:

```
dc rejectrect 0 0 594 3450
dc rejectrect 594 3160 2408 290
dc rejectrect 594 0 2417 283
dc rejectrect 2847 0 603 3450
```

Perkin Elmer images (.tiff)

The Perkin Elmer XRD 1621 flat panel detector installed at P02.2 produces detector images in .tiff format, that have to be converted by program *P02 Mar Rename* into
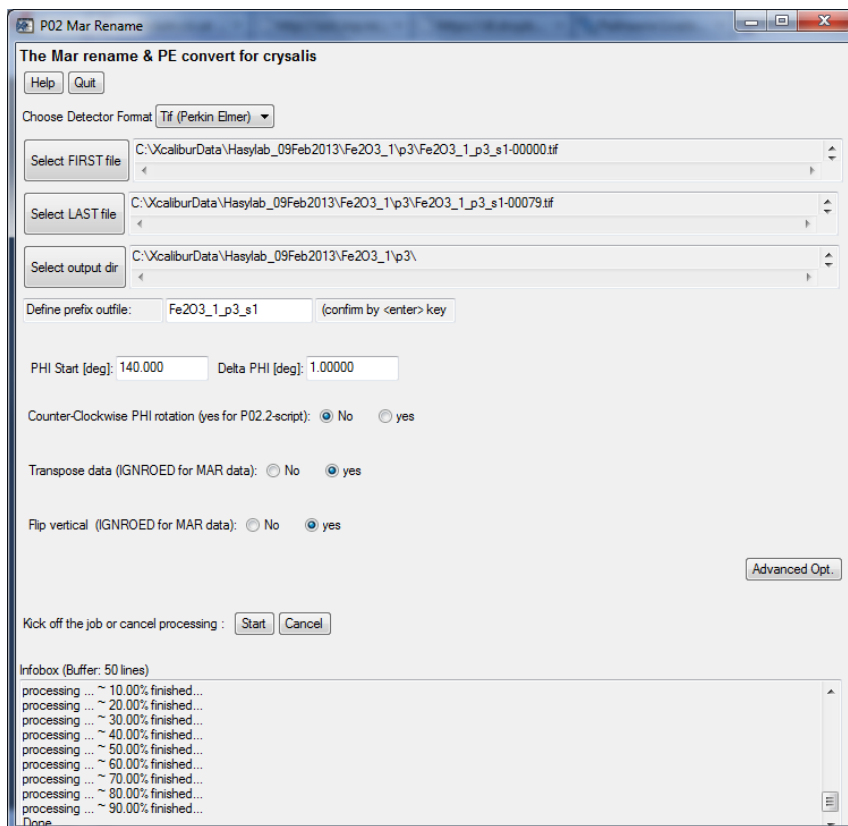
Figure 3.3: GUI for .tiff − .esperanto transformation.

.esperanto images. This image format was specially developed to provide a tool to interface unsupported image formats with $CrysAlis^{Pro}$. A detailed description of .esperanto format and *P02 Mar Rename* has been recently given by Rothkirch et al. [68].

A screenshot of the user interface is given in Fig. 3.3. For the transformation, the first and the last files of an image series need to be selected as well as an output directory, starting value for the ϕ angle and a step width of the scan. In addition, the tool makes it possible to select the scan direction and detector orientation by setting the flags **counter-clockwise rotation**, **transpose data** or **flip vertical**, respectively. The **Advanced Opt.** button offers different settings for modifying the header information.

Other images formats and options

During the preparation of this chapter a new version of $CrysAlis^{Pro}$ (137.37.31) was released [69]. It contains internal converter from many known (Mar, Sapphire, Saxi, Dtrek, Dectris) and generic image formats to .esperanto. It can be invoked form the
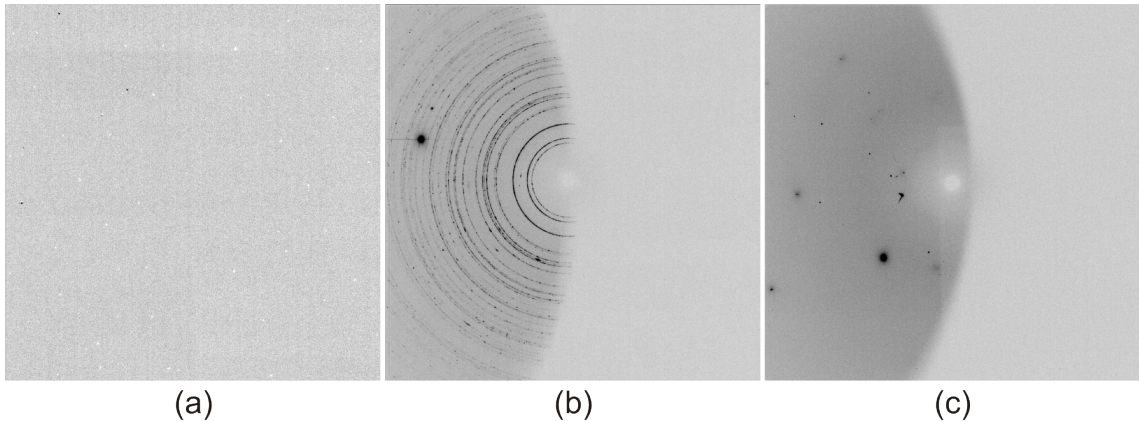
Figure 3.4: Typical appearance of the first or last frames in the data set collected in the DAC. (a) Fully shaded frame. (b) Frame containing diffraction from the gasket or(and) the DAC body. (c) Normal frame.

command line by typing **dc rit**. In the popup window a user can straightforwardly specify all parameters required for the .esperanto header creation. More information about **dc rit** command can be found in Ref. [70].

3.2   Peak search and indexing

Before the peak search procedure, the useful frame range must be determined. Usually, the data collection is performed in ω range from -40 to 40°, but very often the useful range is slightly smaller. So, first frames may contain diffraction from the DAC body or be completely shaded (Fig. 3.4). Fully shaded frames will not cause critical problems with unit cell finding if they are included into the peak search procedure, but they definitely must be excluded during the integration. At the same time, frames containing lots of diffraction rings may significantly complicate the unit cell determination. So it is strongly advised not to use such frames during both the final integration and the peak search procedure.

The peak search procedure is activated by typing **ph s** in the CMD or from the lattice wizard menu. In order to locate a peak $CrysAlis^{Pro}$ uses two parameters: threshold value and 7×7 average [71]. First, only image pixels with an intensity higher than the selected threshold are considered for peak localization. If such a pixel is found a series of neighborhood test are performed. The average intensities of 3×3, 5×5 and 7×7 pixel areas are computed. The central pixel is considered a peak if $I_{3\times3} > I_{5\times5} > I_{7\times7}$. Furthermore, $I_{7\times7}$ has to be higher than a user-specified value, and no pixel in 3×3 perimeter may have larger intensity than the central

pixel.

There are three options for the peak search. Automatic threshold and background detection, smart peak hunting and traditional peak hunting with user-defined threshold level and 7×7 average. It is noticed that automatic threshold and background detection works well with original Xcalibur data collections and detectors, while for external images and experiment types it may miss many sample reflections. It becomes especially crucial, if weak incommensurate peaks are not detected. For data collected with the Perkin Elmer detector in most of the cases **smart peak hunting** works well, while for the Mar555 images it is advised to use the traditional peak hunting with user-defined parameters.

In order to properly assign indices to each spot on a diffraction image, the orientation of the crystal in space must be known. For that one needs to relate the diffractometer coordinate system with the axes that define a diffraction pattern for a given sample. The orientation matrix **UB** defines the relation between the crystal vector $\mathbf{h} = h\mathbf{a}^* + k\mathbf{b}^* + l\mathbf{c}^*$ and the instrument vector $\mathbf{r_0}$:

$$\mathbf{r_0} = \mathbf{UBh}. \tag{3.1}$$

The matrix elements contain information about the unit cell and orientation of the crystal. The main problem for the indexing is the presence of diamond and pressure transmitting medium peaks in the peak table. There are different options of the indexing:

- Automatic indexing taking into account all found peaks.

- Search for a known unit cell taking into account all found peaks.

- Automatic indexing after "cleaning" of the peak table from diamond and pressure-transmitting-medium peaks.

- Setting the orientation matrix by hand (e.g. if known from previous pressure point).

- Manual selection of the unit cell using **Ewald Explorer**.

The first option usually works well if the sample unit cell has a rather large volume and if the diffraction data are collected at relatively low pressures, when the pressure-transmitting medium is not yet crystalline, so that the number of sample peaks in the peak table is significantly larger than the number of unwanted peaks. The commands **um ttt** and **um f** activate the auto-indexing routine employing different algorithms for indexing in direct and reciprocal space respectively. It is claimed that indexing in direct space employing a method described by Duisenberg
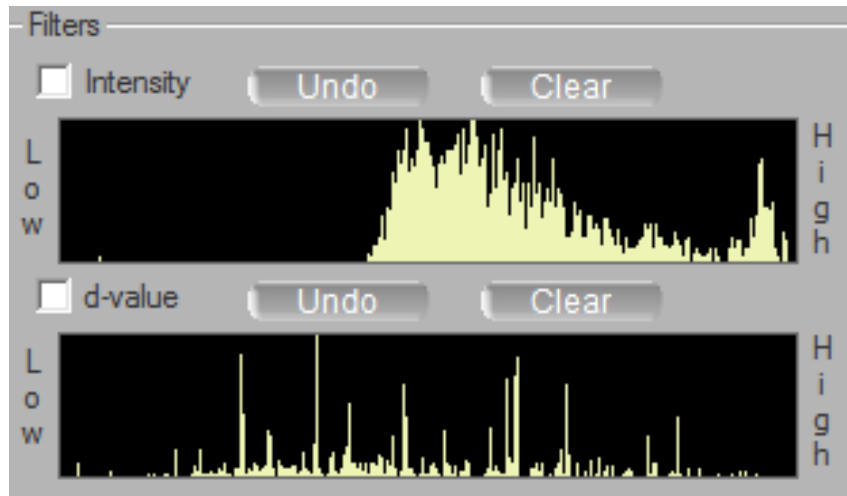
Figure 3.5: Histograms showing intensity and *d*-value distributions.

[72] works more reliable in difficult cases like incommensurate crystals, twin lattices, fragmented crystals or unreliable data.

If automatic indexing failed, but the approximate lattice parameters are known, there is a possibility to search for the known unit cell using the command **um searchcell**. In the popup window a user specifies the lattice parameters, number of reflections which will be considered at each step of the search. The search is stopped if more peaks than in the **Stop if percentage** field are found. The default value is 90 %, however for high-pressure data this number must be significantly lower (30-50 %).

If the search for a known cell doesn't lead to a reasonable result (in case of very large number of peaks which do not belong to the sample), or the lattice parameters are not known, a user should try to determine, which peaks belong to diamond or to pressure-transmitting medium and delete them. First of all, it is reasonable to inspect the peak table by typing **pt e** in CMD. Many diamond peaks are usually overexposed. The peaks may be sorted by intensity and overexposed ones should be deleted.

A very useful tool for separation of sample peaks from diamond and pressure-transmitting medium peaks is so-called **Ewald Explorer**, that can be activated by typing **pt ewald**. First of all, histograms showing the distributions of intensities and *d*-values should be examined (Fig. 3.5). So a group of very intense reflections in the upper histogram in the Fig. 3.5 most probably corresponds to diamond peaks, while numerous peaks at certain *d*-values (lower histogram on the Fig. 3.5) are often contributions of the pressure-transmitting medium, which produces numerous and intense reflections at the same *d*-values. These reflections can be deleted by dragging
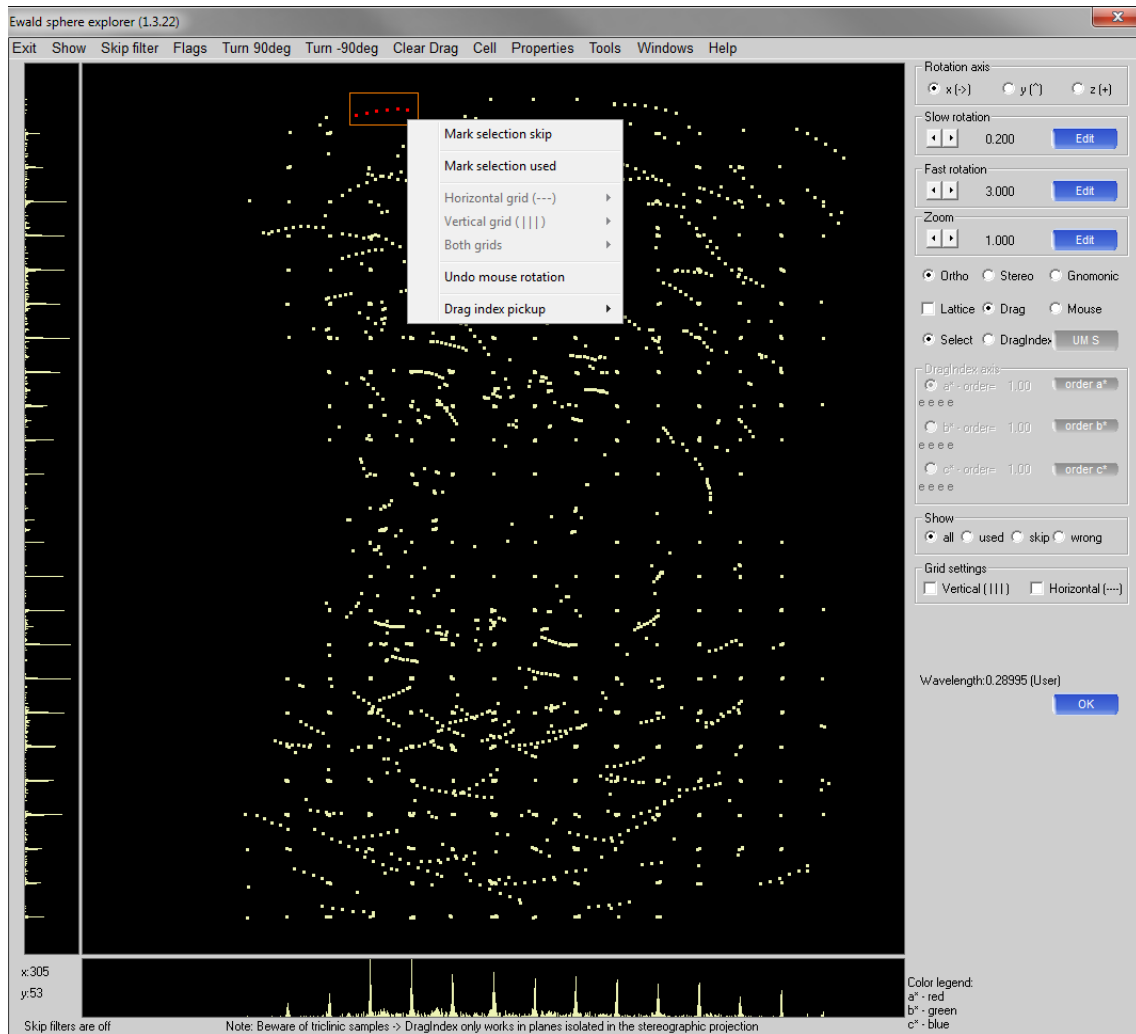
Figure 3.6: Unit cell search in Old Ewald Explorer.

mouse on the corresponding histograms.

Diamonds in DACs are large single crystals with very large mosaicity, and therefore, diamond reflections usually appear on several consecutive frames. Furthermore, the diamonds are not on the ω-rotation axis, and therefore, parts of one diamond reflection on adjacent frames may have different apparent 2θ values. Because of this reason the peak search procedure may assign one diamond reflection to multiple peaks. This produces arcs in the reciprocal space. Since many peaks constituting the arcs have different d-values, they are not effectively cleaned using the distribution histograms, and should be removed by hand. The most convenient option for this is to use **Old Ewald Explorer**, that can be launched in a sequence **Lattice wisard** - **Ewald Explorer** - **Old Ewald Explorer**. The reciprocal space can be rotated
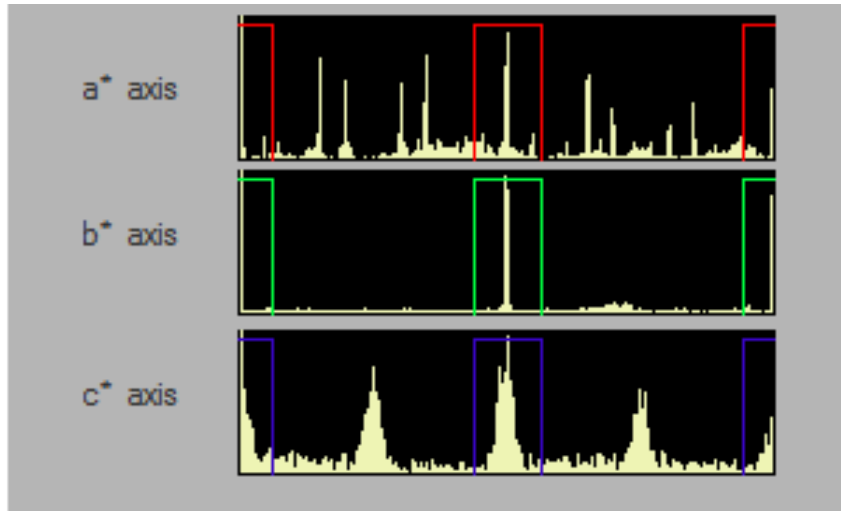
Figure 3.7: Intensity distribution diagrams typical for incommensurate crystals. Colored boxes are at the positions of the main reflections.

in a way that one can see the rows of the sample peaks (Fig. 3.6). Then unwanted peaks (e.g. arcs as in the Fig. 3.6) should be skipped (right mouse button – **Mark selection skip**). Peaks flagged **skip** will not be considered for the unit cell finding.

If the orientation matrix is known from previous pressure point it can be imported to the current experiment and refined. The command **ty u** prints the orientation matrix, and the command **um s** is used to set the orientation matrix for the current data set. The matrix can be refined by the command **um i**.

A very important step is to check the correct selection of the unit cell and to visualize reciprocal space. In case of a standard data collection an indication of possible twinning or incommensurate structures is that a noticeable number of peaks from the peak search procedure can not be indexed. In case of HP data, lots of unindexed peaks are usually "rubbish". So, in case of HP data collection, it is absolutely necessary to make reconstructions of the reciprocal lattice planes. The command **dc unwarp** starts the guided wizard. The first window shows the current orientation matrix, which will be used for the reconstruction. The dialog in the second window allows to adjust the number of frames which will be used in the reconstruction. The layers to be reconstructed are defined in the third window. For default reconstruction, one should click **Generate layers**, and input two numbers in the pop up window: the max order for the generation (e.g. 1) and its resolution (e.g. 0.8). This will generate a number of hkl planes with h,k,l varying from -1 to 1 (-1kl, 0kl, 1kl, h-1l, h0l, h1l, hk-1, hk0, hk1) at 0.8 Å resolution.

In case if one wants to make nonstandard planes or to use nonstandard options
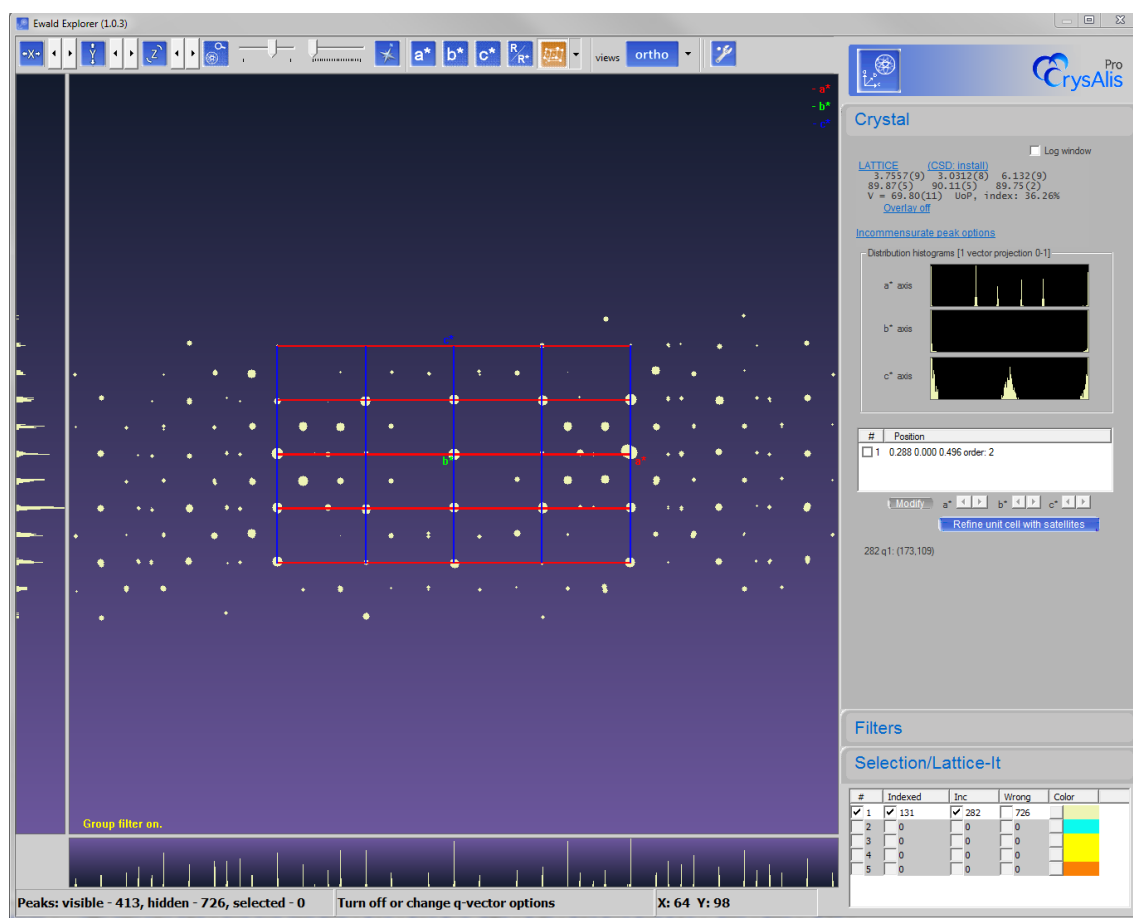
Figure 3.8: $CrysAlis^{Pro}$ Ewald Explorer.

(e.g. for reconstruction of reciprocal lattice planes with non-integer indices) the information for the reconstruction should be given manually (command **New layer**) The plane is defined by L1, L2 layer vector and O - origin vector. The next dialog allows to activate the background subtraction. The same values of **Re** and **Fr** as for data integration should be used (see section 3.3).

In the last dialog the appropriate image scale should be defined. The most suitable scale depends on the detector, exposure time and primary beam intensity, so one may need to repeat the reconstruction several times. As starting values one may use 1 for Perkin Elmer images, 50 for Mar555 images and 30 for in-house data collection using Mar345 image plate detector.

Indexing in case of incommensurate structures

$CrysAlis^{Pro}$ can handle diffraction data of incommensurate crystal structures. Additional satellite reflections may be found on the reconstructed reciprocal planes or
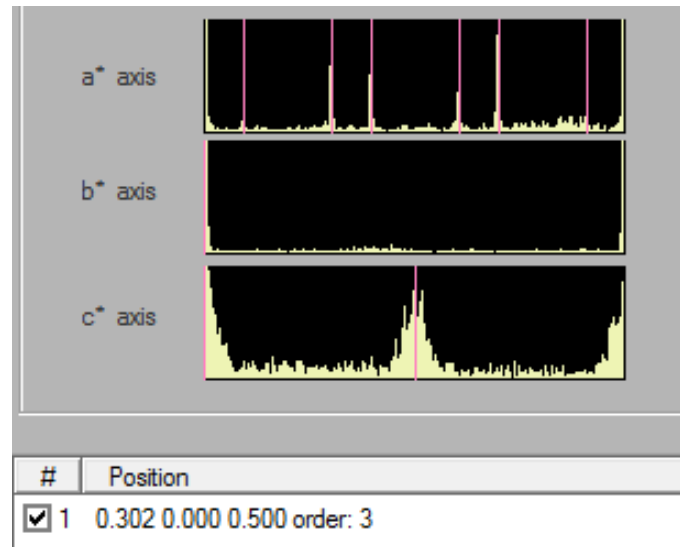
Figure 3.9: Intensity distribution diagrams typical for incommensurate crystals. Vertical lines represent the calculated position of satellite reflections of different orders.

by inspecting intensity distribution diagrams projected on the reciprocal average unit-cell axes (Fig. 3.7)

In **Ewald Explorer** (Fig. 3.8) press **Activate incommensurate peaks** and give initial values for the **q**-vector components, using the distribution histogram (Fig. 3.9). Press **Refine unit cell with satellites** and define the maximal order of satellites **mmax**, and indexing tolerance **crithkl**.

3.3 Profile fitting

There are two different procedures for determining the integrated intensities: summation integration and profile fitting. Summation integration implies adding intensity values for all pixels lying within the area of a spot, and then subtracting the estimated background contribution. Profile fitting assumes that the spot shape is known, and the intensity is derived by finding the scale factor that gives the best fit to the observed spot profile [73]. $CrysAlis^{Pro}$ employs a profile fitting method.

The evaluation of integrated intensities of Bragg reflections in $CrysAlis^{Pro}$ is based on the three-dimensional reconstruction of the peak profile. So, the integration is performed as a function of the area detector coordinates (x, y) and the scanning direction (ω) [71]. A fundamental requirement for the integration is that it should distinguish between signal and background. For weak reflections this cannot be done reliably. The assumption adopted by most data-processing packages is that

both weak and strong reflections have the same profile shape models. The profile shape depends on the following factors:

- path of the reflection through the Ewald sphere;

- angle of incidence of the diffracted beam;

- crystal mosaicity;

- point spread function of the detector;

- beam divergence;

- scan width;

- wavelength split of $K_{\alpha 1} - K_{\alpha 2}$.

So, if the profile shapes of the strong peaks are learned, the profile shapes for weak reflection can be modelled analytically. Unfortunately, the user manual does not contain information about explicit formulas for the profile fitting algorithm used in the $CrysAlis^{Pro}$. Nevertheless, the general idea is the following. The reflection intensity I can be calculated as [73]:

$$I = \frac{\sum_i (c_i - b_i) p_i / \nu_i}{\sum_i p_i^2 / \nu_i}, \tag{3.2}$$

which minimizes the function:

$$\psi(I) = \sum_i (c_i - I \cdot p_i - b_i)^2 / \nu_i, \text{ with normalization condition } \sum_i p_i = 1 \tag{3.3}$$

where b_i is the predicted value of the background, c_i is the observed intensity in pixel i, p_i is the predicted profile and ν_i is a variance of c_i. The index i represents all pixels in a profile. Implementations of the method differ usually in the assumptions about the variances ν_i [73].

Profile fitting dialog is invoked by a command **dc proffit**. The parameters for peak profile fitting should be given in 6 consecutive steps, which are described in detail below.

Step1 - Orientation matrix

In step 1 the orientation matrix, that will be used for the data reduction, is shown. Additional information may include **q**-vectors or twin lattices if relevant. At step 1 it is possible to choose the lattice type in **Lattice extinctions** field.

For incommensurate structures in case of a single **q**-vector, which was previously refined, it will appear by default in the field **Incommensurate structures**. In case of multiple **q** vectors, one must specify the data reduction options. Select **Other(reduction list)** and press the button **Generate**. The window appears, in which one can choose the type of data reduction list (hklm, hklmn, hklmno for 1d, 2d, 3d - incommensurate structures respectively). Furthermore, here one should give the maximal satellite orders and cross **q**-vector reflections.

It is important, that in case of more than one **q**-vector, the program doesn't respect the standard lattice extinctions. A user must specify them in advance by using the command **dc extinct**. For example, the command **dc extinct hklmn 1 1 0 0 0 2 1** implies the extinction condition $1 \cdot h + 1 \cdot k + 0 \cdot l + 0 \cdot m + 0 \cdot n = 2p + 1$ and corresponds to a C-centering of the lattice.

Step2 - Experiment run list

During the step 2 you should specify the frame range which will be considered for the integration. In general, this range is the same as that used for the peak search (see section 3.2).

Step3 - Algorithm parameters

The algorithm parameters are adjusted in step 3. Click **Edit special pars** to enter the special parameters menu. First of all set the opening angle of the DAC in **Edit DAC angle**. For usual BX90 DACs, the value of 38–39° is used. In case of large uncertainties in the orientation matrix, or large strain gradients in the crystal, you may want to adjust the integration masks in the group **Profile fitting**. Press `Alt+E` to access the hidden parameters. Generally it is recommended to skip instrument model refinement. This option can be activated in **Hidden parameters** menu. Usually, the instrument model is refined precisely based on the standard crystal with large unit-cell volume. In case of any detector movement, calibration is repeated.

Step4 - Background evaluation

In the step 4 the background subtraction parameters are defined. There is an option to choose between two algorithms of background determination. The default one is the average background, which is claimed to be a better choice for low stable background and strong data. The so-called smart background algorithm computes a running average of the background by using adjacent frames. It is the better
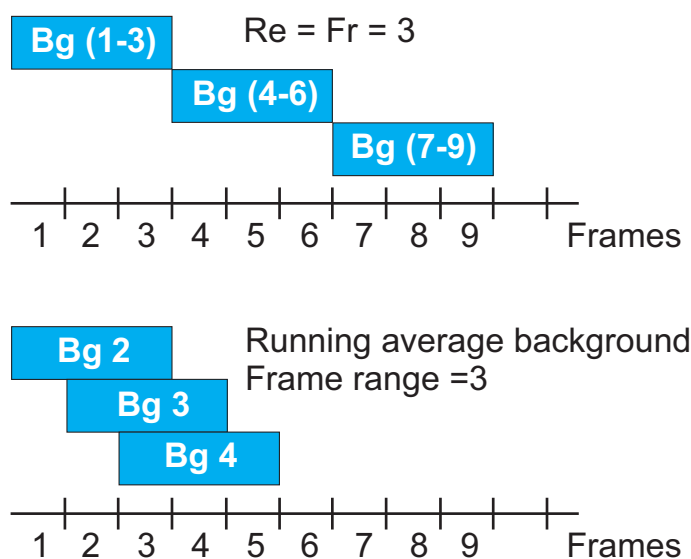
Figure 3.10: Differences in background evaluation algorithms between average background option with Re=Fr=3 and running average background with frame range $= 3$. The figure is adapted from $CrysAlis^{Pro}$ manual.

choice for high and fluctuating background and weak data. However this algorithm is computationally more demanding than the average background algorithm.

In case of high-pressure data, in fact, both options can be used. In $CrysAlis^{Pro}$ the procedure of average background determination is controlled by two parameters: the evaluation range **Re** and the repeat frequency **Fr**. The evaluation range defines the number of frames which are used to compute a single background image, and the repeat frequency is the frequency with which the procedure is repeated. By default values of **Re**=**Fr**=25. For high-pressure data these values must usually be significantly lower. For example, in case of high-pressure data collection of FeOCl (see chapter 5) using Mar345 detector with more or less stable background, **Re**=**Fr**=5 was used.

However, for Perkin Elmer and Mar555 detectors, the use of running average background is suggested. After selecting "Smart" background option the **Frame range** parameter must be specified. This parameter is always an odd number. So if it equals 1, only the local background from single frame will be evaluated. Value of 3 means that also adjacent frames will be used for background determination (Fig. 3.10).

Step5 - Outlier rejection

Although, high-pressure data are usually not very redundant, in case of high-symmetry structures it is still possible to apply outlier rejection based on the algorithms reported by Blessing [74]. The identification and rejection of these outlying intensities is crucial for a satisfactory structure solution and refinement of high pressure data. This option can be chosen at step5 of the data integration wizard. Click **Use outlier rejection** and specify the Laue group. If you are not yet sure about the correct symmetry don't use this option. Final analysis of outliers can be performed using recently implemented options in Jana2006. These procedures are described in Ref. [75] in detail.

Step6 - Output

At the step6 choose the output file name (use different name for each integration). In **Finalization options** you usually may wish to edit only the compound chemical formula for the further absorption correction, while other options like space group determination or automatic structure solutions will be done later using external programs.

3.4 Data finalisation and absorption correction

Generally **dc proffit** performs completely automatic data reduction including frame scaling and multiscan absorbtion correction. However, if you would like to adjust some parameters, to perform numerical absorption correction, or to filter and truncate the data, a data finalization tool is implemented into $CrysAlis^{Pro}$.

First, open **Data finalization** window by clicking the tab on the left window panel. Apart from R_{int} and R_σ statistics this window contains all relevant information about data coverage, completeness, detected outliers, absorption correction model and about all problems and warnings that occurred during the data integration.

Click on the tab **Graphs** to visualize frame-by-frame plots for a number of parameters. For instance, the common problem for synchrotron data collections is related to the improper crystal centering. Accordingly, during the ω-scan the crystal may leave the X-ray beam. This results in the loss of diffracted intensities and can be detected by the inspection of the scaling coefficients (absscale) plot (Fig. 3.11). So, if data processing is done immediately after the data collection, the crystal may be recentered. Otherwise, some first and last frames should be removed.
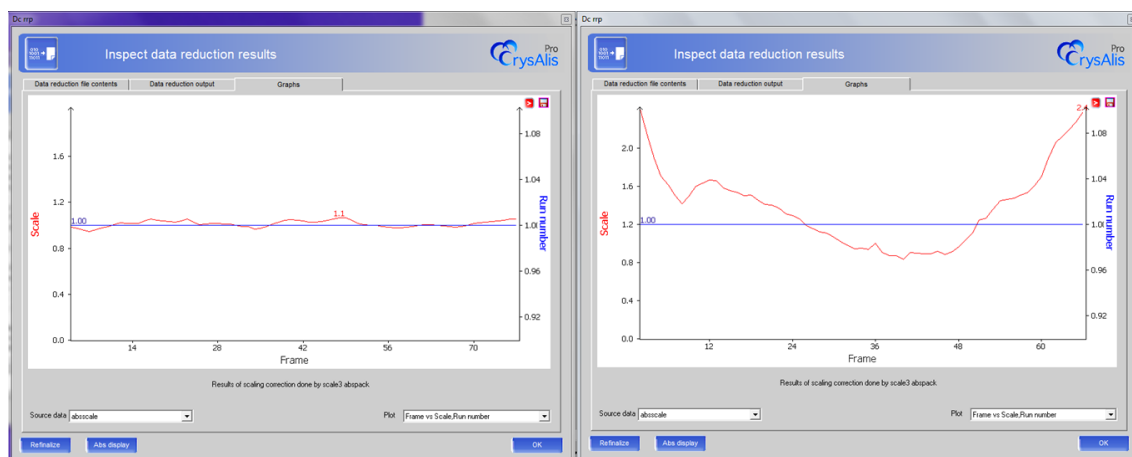
Figure 3.11: Frame scaling coefficients plots corresponding to a well centered crystal (left) and a badly centered crystal (right).

The inspection of R_{int}-frame number plot may help to detect missed overlaps of sample and diamond reflections. For instance, the plot on the Fig (3.12) shows 100% R_{int} at the last frame, and R_{int} exceeds 20% at the frames 53, 55 and 64. At the same time we see in the data reduction output, that for resolution shell 0.58-0.54 Å, the R_{int} is significantly larger than for other shells. Therefore, the overlaps can most probably be found within the 0.58-0.54 Å shell on the frames 53, 55 and 64, while the last frame should be removed from the final integration.

Press **Refinalize** to access the finalization dialog (Fig. 3.13). In the **Sample** group edit the chemical formula and the number of formula units in the unit cell (if it has not been done on the previous stage). In **Corrections** field choose the type of the absorbtion correction. Empirical absorption correction is performed by the *SCALE3 ABSPACK* program. If you would like to adjust the parameters, press **Manual**, and click the button **Advanced**. Default parameters usually work fine the high-pressure data, but in case of very weak absorbers, you may want to reduce the max harmonic order.

3.5 Final integration

Before the final integration one should take care of several things:

- Skip regions shaded by additional equipment (e.g. membrane DAC pipes or laser heating system holder).

- Define the beamstop mask properly.

38
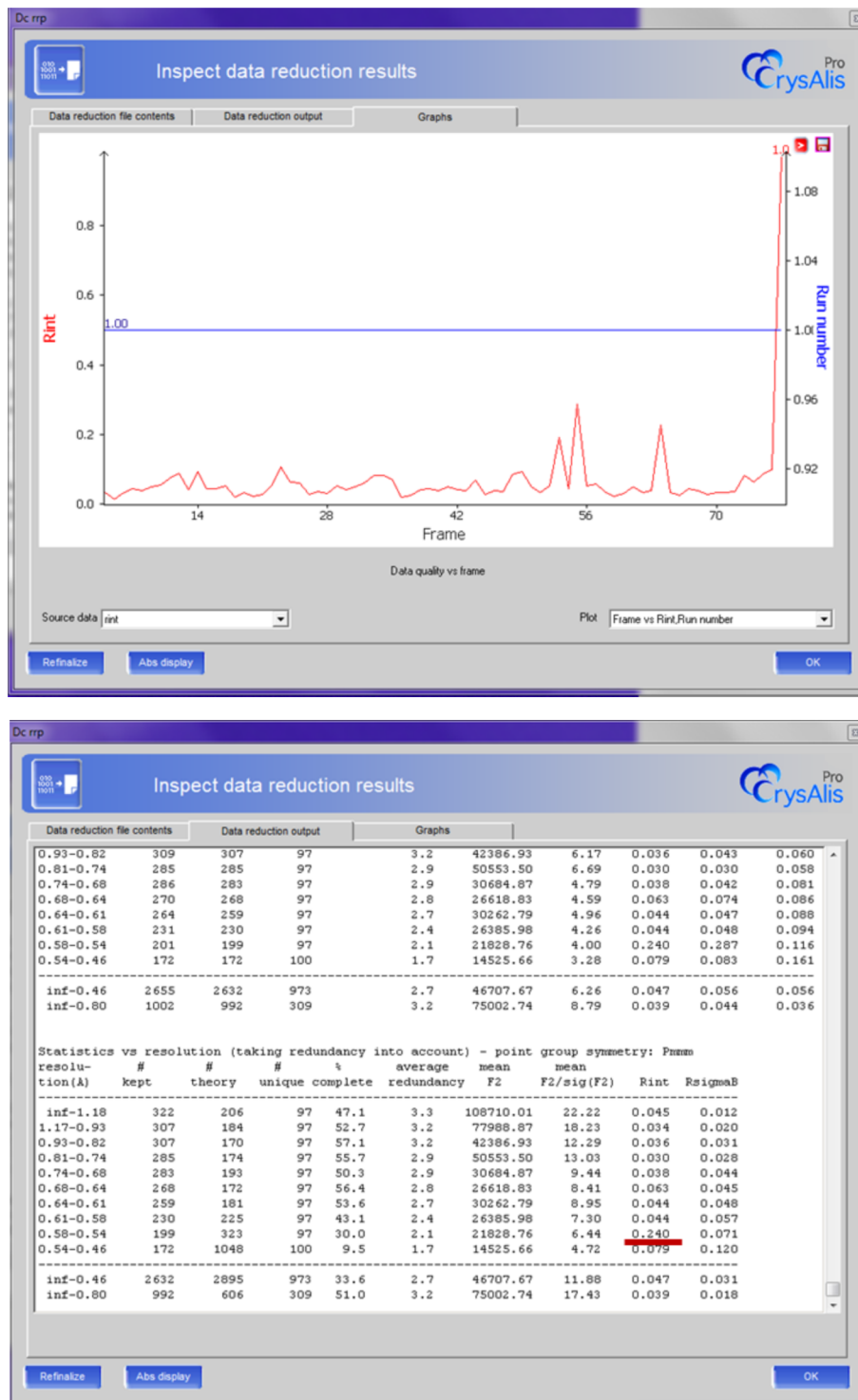
Figure 3.12: R_{int} plot revealing anomalies at the frames 53, 55 and 64 (top) and corresponding data reduction output (bottom).
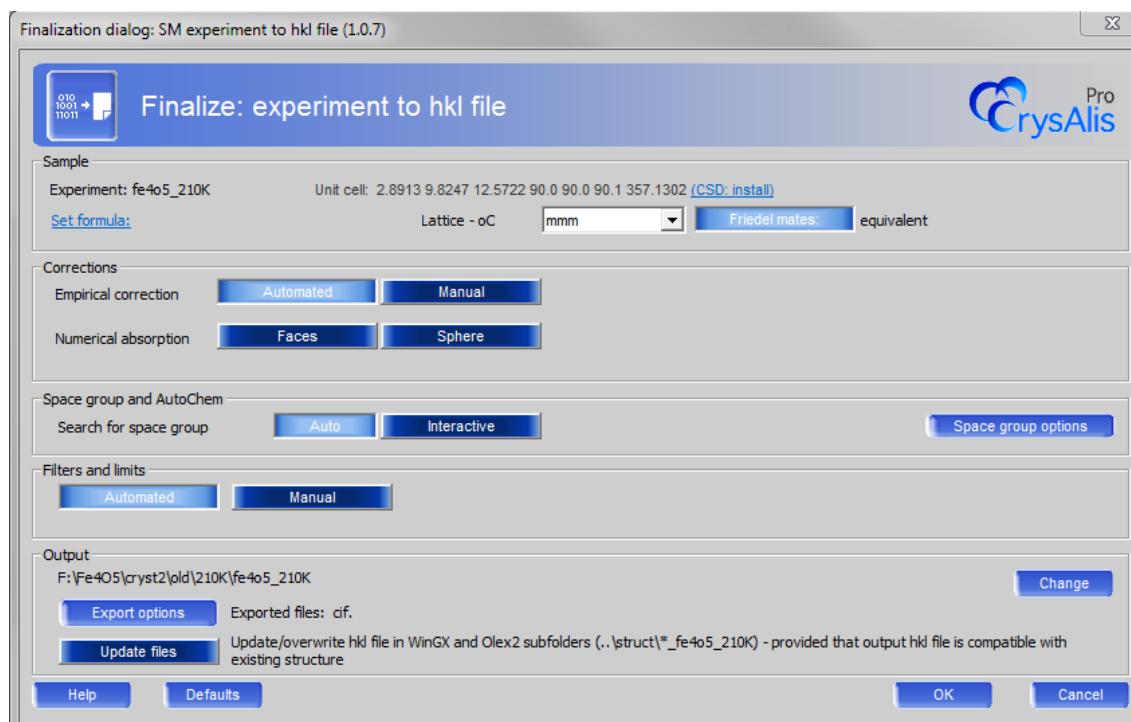
Figure 3.13: $CrysAlis^{Pro}$ data finalization dialog.

- Thoroughly search for overlaps between sample reflections and those from diamond or pressure-transmitting medium.

- Be sure that the set of parameters, used for the final integration is the most appropriate for the current data.

To skip the shaded region use the command **dc rejectrect** which was discussed in section 3.1. To define the beam stop click **Options RED** in CMD, select the tab **Beam stop** and activate **Put beam stop overlay on**. Adjust beam stop orientation and dimensions using the tabs in the same window.

To search for reflection overlaps, press the button **Overlay spot predictions on the diffraction image** and select **Predict peaks from UB**. Fig. 3.14 shows the part of the diffraction image without (on the left) and with (on the right) predicted peak positions, indicated by crosses. It appeared that one of nine predicted reflections overlaps with diamond reflection, so it must be rejected. The information about the indices of this reflection can be obtained by pressing button **Information cursor** and moving the cursor to the predicted position. Note all such reflections (fortunately, there are usually not more than 80 frames to inspect), go to the peak table editing dialog (command **pt e**), select these reflections and press the button **Reject**. Save the file with rejected reflections. Type **dc rejectrfxy** to load the rejection file before the
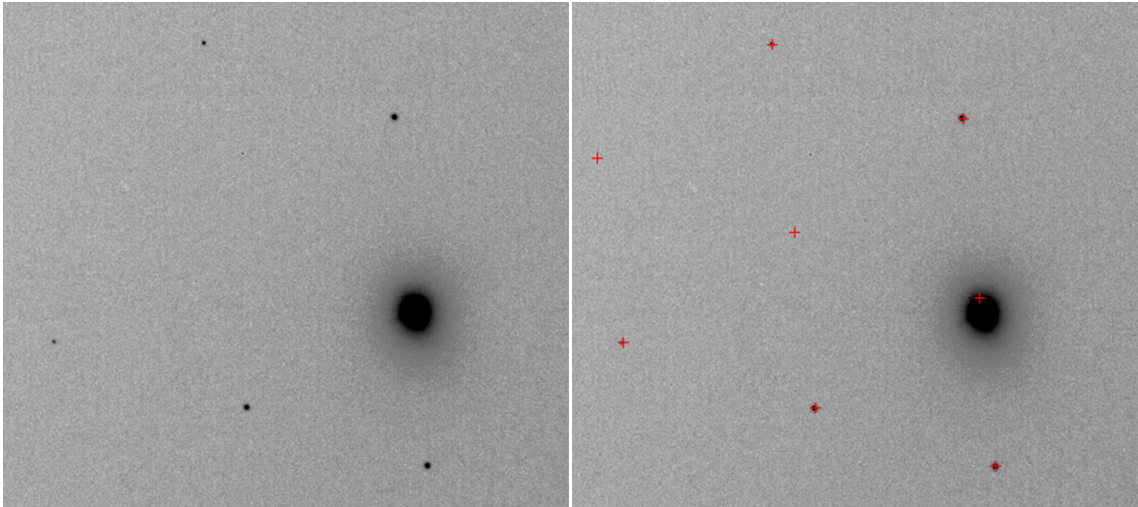
Figure 3.14: Visual inspection of reflection overlaps. See text for more details.

final integration. Incorrect outlier rejection may significantly influence the quality of the empirical absorbtion correction and scaling, therefore, should be performed before the final integration.

In order to choose the best set of algorithm parameters you may use the command **xx proffitloop** which will create the script for a number of alternative integrations starting from the same orientation matrix and instrumental model parameters, but using different algorithm parameters (e.g. different background evaluation parameters, peak integration mask size). The user then may choose the best integration parameters by inspecting the output files.

3.6 Dealing with several data sets

In order to increase the data completeness the DAC can be rotated by 90° around the primary beam direction. Also, especially in case of incommensurately modulated structures, the dynamic range of the detector is usually not high enough to detect weak satellite intensities together with strong main reflections simultaneously. Therefore, diffraction data may be collected using different exposure times or filters. So, in the best case, four data sets are available for each pressure point. $CrysAlis^{Pro}$ doesn't reliably work with several data sets if they are collected not at Xcalibur diffractometer. Therefore, each data set has to be integrated individually. The resulted reflection files can be merged in Jana2006. A scale is determined on the basis of reflections which are common for the data sets. The user can specify the $I/\sigma(I)$ threshold for the reflections which should be used for scale determination.

By default only reflections with $I/\sigma(I) > 10$ are used.

3.7   Conclusions

Nowadays modern crystallographic software can process the standard X-ray diffraction data set and provide a reliable-quality reflection file in "one click". This is not yet true, however, for high-pressure data, where a user involvement in choosing the proper integration parameters is much more crucial.

Chapter 4

Superspace approach to high-pressure superstructures[1]

4.1 Introduction

X-ray diffraction in a diamond-anvil cell (DAC) is a powerful tool for studying materials at high pressures [56, 76]. The application of external pressure leads to various phenomena including insulator-metal transitions [77, 78], high-spin to low-spin transitions [79], enhancement of superconductivity [80], and normal-to-incommensurate phase transitions in elemental metals [51]. A group of phase transitions between a high-symmetry form, and a low-symmetry distorted form stable at higher pressures represent a significant part of pressure-induced processes [81–84].

High-pressure X-ray diffraction usually suffers from undesirable diffraction from diamonds, gasket and pressure-transmitting medium, insufficient data resolution and low coverage of the reciprocal space. To increase the coverage, several crystals in different orientations may be placed into a DAC. However sometimes the morphology of the crystal, *e.g.* in case of plate-like crystals predefines its orientation. In this sense, the conventional analysis of complex superstructures may be quite difficult due to the very small ratio between the number of independent reflections and the number of refined parameters.

The superspace approach is an established method to describe incommensurate and commensurate superstructures [52, 85, 86]. Furthermore, in the last years a number of computer programs were developed for convenient data processing, struc-

---

ture solution and refinement. Among them are *SUPERFLIP* [87], the program for the structure solution in arbitrary dimensions, *JANA2006* computing system for structure refinements and analysis [88], and *EVAL15* integration software [89].

The main idea behind the superspace description is that the superstructure may be interpreted as its basic structure with three-dimensional space group symmetry and a small unit cell, which is subjected to a periodic deformation. Modulation functions are characterized by a wave vector $\boldsymbol{q}$, whose components are given with respect to the basis vectors of the reciprocal lattice of the basic structure:

$$\boldsymbol{q} = \sigma_1 \boldsymbol{a}^* + \sigma_2 \boldsymbol{b}^* + \sigma_3 \boldsymbol{c}^* \tag{4.1}$$

Commensurate modulations are described by modulation wave vectors with only rational-valued components. Therefore, an integer N exists, for which $N\boldsymbol{q}$ is equal to reciprocal lattice vector of the basic structure.

Within the superspace approach, the position ($\boldsymbol{x}$) of the atom μ is defined by its position in the basic structure ($\bar{\boldsymbol{x}}$) plus a displacement:

$$\boldsymbol{x} = \bar{\boldsymbol{x}} + \boldsymbol{u}^\mu(\bar{x}_4), \tag{4.2}$$

where $\bar{x}_4 = t + \boldsymbol{q} \cdot \bar{\boldsymbol{x}}$, with t being the phase of modulation and $\boldsymbol{u}^\mu(\bar{x}_4)$ is the modulation function of atom μ. In principle, the only requirement on the modulation functions is that they are periodic, so that $\boldsymbol{u}^\mu(\bar{x}_4) = \boldsymbol{u}^\mu(\bar{x}_4 + 1)$. However, it is convenient to represent atomic modulation functions as Fourier series:

$$u_i^\mu(\bar{x}_4) = \sum_{n=1}^{n_{max}} A_i^n(\mu) \sin(2\pi n \bar{x}_4) + B_i^n(\mu) \cos(2\pi n \bar{x}_4), \tag{4.3}$$

for $i = x, y, z$. Therefore, for the structural analysis in superspace A_i^n and B_i^n are the parameters that must be determined along with the atomic coordinates in the basic structure.

In case of commensurate modulations, the model described in superspace might need less parameters than the supercell in three-dimensional (3D) space, because it is usually possible to concentrate on the most important parameters, like low-order harmonics in the Fourier expansions of the modulation functions, while higher-order modulation parameters may be not substantial for the distortion. This reduction in the number of independent parameters is especially important for highly incomplete high-pressure data. Despite the obvious usefulness of superspace description of superstructures, it is rarely applied by high-pressure crystallographers. One of the few examples is the high-pressure phase of Ga, that seems to be rather complex at first sight but can be described with a simple distortion of the average structure

using 4 modulation parameters instead of the 38 parameters needed when using a conventional approach [90]. Another method to reduce the number of parameters is to use symmetry mode analysis and to refine the amplitudes of the most important modes only. However, especially in case of large superstructures a mode decomposition may be less efficient [91]. Here we will demonstrate the usefulness of the superspace approach on the examples of isostructural layered FeOCl and CrOCl, forming different superstructures above 15 GPa.

4.2 High-pressure superstructures of transition metal oxychlorides

4.2.1 Experiment preparation and data collection

The use of synchrotron facilities is a preferable choice for any high-pressure X-ray diffraction experiment. The high-energy of the synchrotron X-ray photons allows to significantly increase the angular resolution compared to conventional in-house sources. Small focus size allows to get rid of gasket diffraction and of strain gradients within the crystal. High intensity reduces data collection times and enables detection of weak superstructure reflections in case of small distortions.

We have performed single-crystal X-ray diffraction experiments on the high-pressure phases of FeOCl and CrOCl at beamlines P02.2 (DESY, Hamburg) and ID09A (ESRF, Grenoble), respectively. The data collection for FeOCl was performed using a wavelength of 0.29004 Å and a Mar345 image plate detector, while the data collection for CrOCl was performed using a wavelength of 0.4144 Å and a Mar555 flat panel detector. For both experiments we have used the combination BX90 DACs [60] with Boehler-Almax anvils [59] which provide a large opening angle of $80°$ in 4θ. Such a large X-ray opening is extremely important for single-crystal X-ray diffraction, in order to increase reciprocal space coverage. Perfect quality single crystals of FeOCl and CrOCl were loaded in a 125 μm hole of an preindented rhenium gasket along with ruby spheres for pressure determination [63]. The DACs were loaded with neon as pressure-transmitting medium using the BGI gas loading system [61]. For each sample, 80 independent frames in an ω-scan range of -40° to +40° were collected (1° scanning step size) with an exposure time of one second.
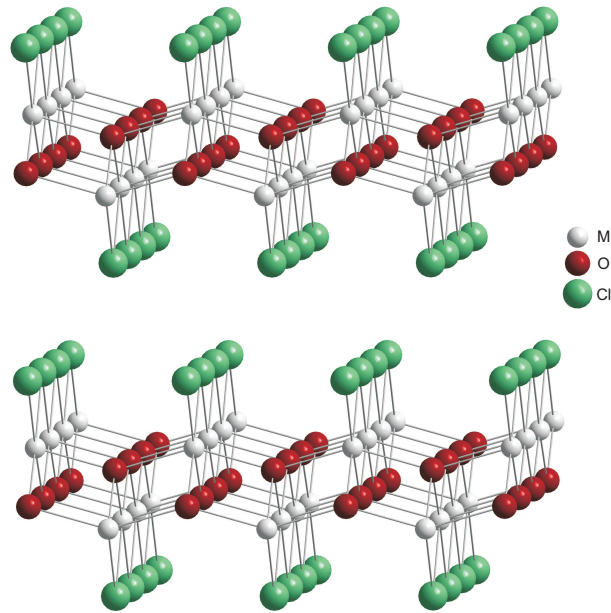
Figure 4.1: Crystal structure of MOCl at ambient conditions.

4.2.2 Indexing and integration of diffraction patterns

FeOCl and CrOCl belong to a group of isostructural layered transition metal oxychlorides, MOCl (M = Ti, V, Cr, Fe), which have recently been investigated due to their low-dimensional magnetic properties [19–21, 34]. At ambient conditions MOCl possess the orthorhombic space group $Pmmn$. Their structure consists of double M-O layers, separated by Cl bilayers (Figure 4.1). Highly anisotropic compression of these compounds leads to structural instabilities at high pressure and they undergo a phase transition in the vicinity of 15 GPa, which is accompanied by an appearance of weak superlattice reflections. The diffraction pattern of FeOCl at 22.7 GPa may be indexed with the orthorhombic lattice as valid for the low-pressure phase and a modulation wavevector $\boldsymbol{q}^{Fe} = (\frac{1}{4}, 0, \frac{1}{2})$, employing four integers ($hklm$) (see Figure 4.2 (a),(b)). The fourfold superstructure features rows of three satellite reflections between main reflections. Thus, reflection ($hklm$) may be equally indexed as ($h + 1$ k $l + 2$ $m − 4$), and for a unique indexing, the range of m values should be restricted to $−1, 0, 1, 2$. The conventional indexing with three indices would require a primitive monoclinic unit cell as shown on Figure 4.2(c). Finally, the structure may be described with a non-standard $4a \times b \times 2c$ B-centered supercell (Figure 4.2(d)).

The diffraction pattern of CrOCl at 22.9 GPa is more complex. It can be in-
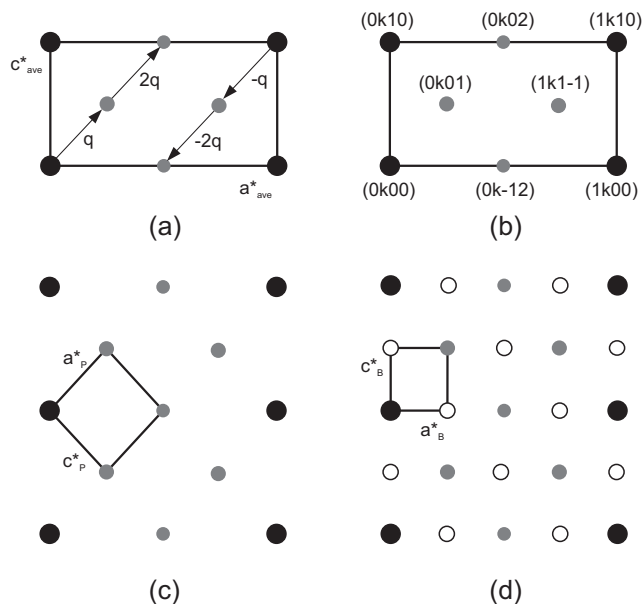
Figure 4.2: Different ways of indexing. Shown are reciprocal lattice planes perpendicular to **b***. (a),(b) - Schematic depiction of the diffraction pattern of FeOCl with main and satellite reflections depicted as black and grey circles respectively, and modulation wavevector $q = \frac{1}{4}a^* + \frac{1}{2}c^*$. (c) Indexing by a monoclinic primitive unit cell (d) Indexing with pseudoorthorhombic non-conventional B-centered $4a \times 1b \times 2c$ supercell.

dexed with the unit cell of the basic structure and $q^{Cr} = (\frac{2}{7}, 0, \frac{1}{2})$ or with a 14-fold orthorhombic supercell (Figure 4.3).

For any commensurately modulated structure, data integration may be performed on the basis of the supercell indexing. Later the supercell–superspace indices transformation can be performed during data importing into *JANA2006*. Data integration and reduction were performed with *CrysAlisPro* program suite which contains useful features for high-pressure data measured in a DAC [50]. For example, it is possible to introduce the DAC opening angle for the correct treatment of DAC shadowing. The built-in explorer of the reciprocal space simplifies the process of the unit cell finding. Furthermore, *CrysAlisPro* is compatible with several instruments and detector types. The in-house software, which allows to convert images to required formats is available at beamlines P02.2 and ID09A. In case of incommensurate structures one can use built-in procedure *NADA* for the simultaneous refinement of the orientation matrix and modulation vector [92].

Special care must be taken for the correct rejection of outlying reflections because standard procedures that work well for conventional data sets, may fail to recognize a significant number of outliers in case of high-pressure data. In the last years several
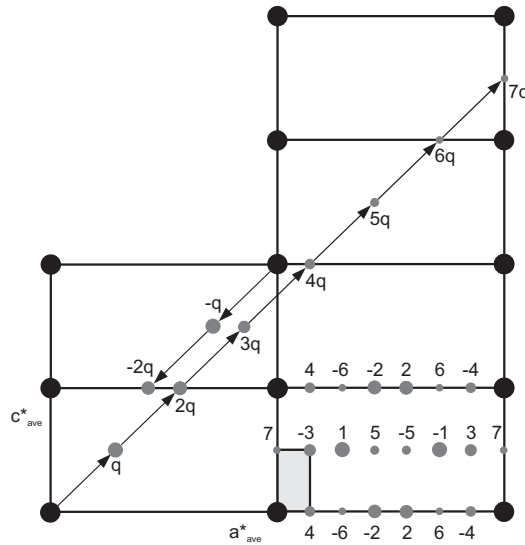
Figure 4.3: Schematic drawing of the diffraction pattern of CrOCl at 22.9 GPa. Only selected superlattice reflections are indicated. The indexing with multiples of the modulation wavevector $\boldsymbol{q} = \frac{2}{7}\boldsymbol{a}^* + \frac{1}{2}\boldsymbol{c}^*$ is demonstrated. The right-lower reciprocal unit cell shows all superlattice reflections of orders $m = \text{-6 .. 7}$. The volume of the superstructure unit cell is 14 times larger than that of the unit cell of the average structure. The reciprocal 3D supercell is indicated.

procedures for outlier identification during the structure determination process were implemented into *JANA2006* program [75].

4.2.3 Structure solution and refinement

The first step in the process of the structure solution is the determination of the symmetry. Usually, the superspace groups compatible with the symmetry of the data are proposed by *JANA2006*. In the present case this leads to two possible superspace groups: $Pmmn(\sigma_1 0\frac{1}{2})00s$ and $Pmmn(\sigma_1 0\frac{1}{2})000$, which in fact are the different settings of $Pmnm(0\frac{1}{2}\sigma_3)000$ (No. 59.1.10.6)[93, 94]. So, all possibilities must be probed for the structure solution. For both CrOCl and FeOCl $Pmmn(\sigma_1 0\frac{1}{2})00s$ appeared to be the true superspace symmetry.

The superspace analysis immediately shows that the high-pressure phases of CrOCl and FeOCl can be obtained as different distorted variants of the ambient-pressure phase. In principle, when the crystal structure of the non-distorted phase is known, the *ab initio* solution of the superstructure is not required, because atomic coordinates in the parent structure can be used as a starting point for the super-
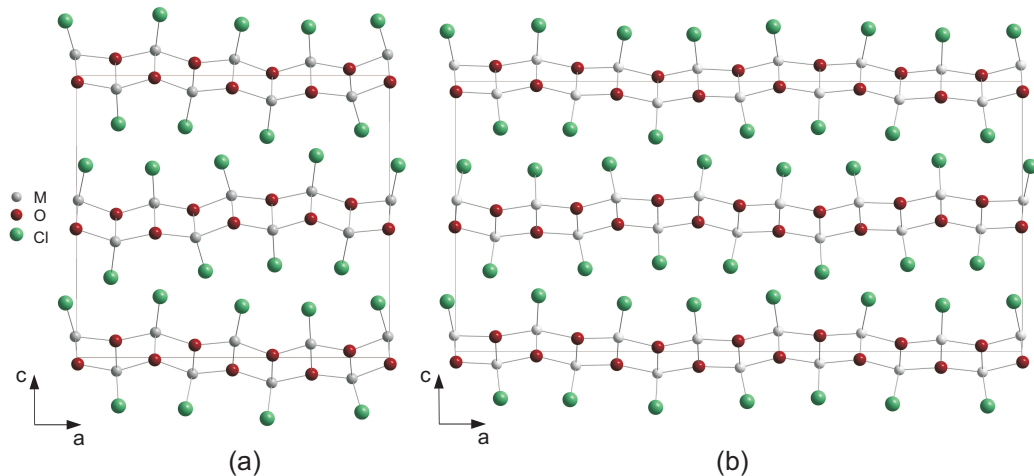
Figure 4.4: Superstructures of FeOCl (a) and CrOCl (b) at 23 GPa.

structure refinements. In general, a fourfold superstructure (in case of FeOCl) would require only up to second-order harmonics for a complete description. However, non-trivial point symmetry requires higher-order harmonics [52]. Thus, the value of n_{max} (see Eq. 4.3) was determined for every atom individually. One must take care that introduction of higher-order harmonics is justified by a significant drop in the agreement factors and that their refined values are meaningful.

For a commensurate modulation, one superspace group corresponds to different 3D structures. Accordingly, different sections $t = t_0$ of superspace lead to different symmetries of the $4a \times b \times 2c$ supercell in 3D space. They are Bm, $B2_1/m$ (both are b-unique) and $Bmm2$. The best fit to the diffraction data was achieved using $t_0 = \frac{1}{16} + \frac{N}{4}$ ($N = 0, 1, 2, 3$), which corresponds to the centrosymmetric, monoclinic space group $B2_1/m$ (No. 11 with standard setting $P2_1/m$) [95].

Employing the superspace approach, we consider the basic structure of FeOCl containing only three independent atoms on the $mm2$ positions. Symmetry restrictions on the modulation functions lead to 14 independent amplitudes resulting in 17 positional parameters to be refined. 19 more parameters were used for the atomic displacement parameters. As a result, together with scale factor and the twin volume ratio, 38 parameters have been refined (Table 4.1). At the same time the conventional refinement in the supercell failed with 62 refinable parameters.

In case of CrOCl the situation is slightly different. The 14-fold superstructure would allow satellites up to 7th order, however only first and second order satellites were observed. As a consequence it is impossible to distinguish between incommensurate and commensurate modulations, and between structures with different values
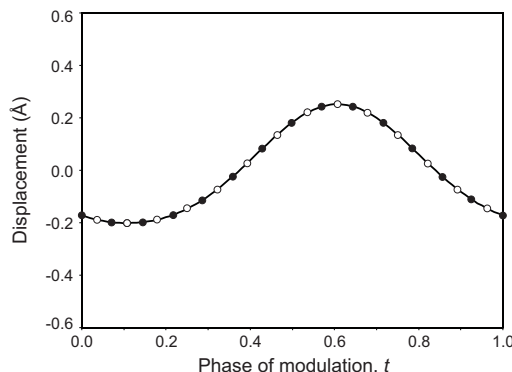
Figure 4.5: t-plot for z-displacement of Cl atom in CrOCl at 22.9 GPa. Filled and opened circles represent values for commensurate $Pcmn$ and $Pmmn$ models respectively.

of t_0. The possible symmetries of superstructures are $Pcmn$ for $t_0 = 0 + \frac{N}{14}$, $Pmmn$ for $t_0 = \frac{1}{28} + \frac{N}{14}$ and $P2_1mn$ for general t-section. According to the structure refinement $Pcmn$, $Pmmn$ and incommensurate models have the same agreement factors (Table 4.1). In this case the determination of the true structure and its symmetry is impossible, but the treatment of the structure as an incommensurate may serve as a good approximation to the real structure. Thus, there are not just 14 specific values for $e.g.$ interatomic distances between two atoms, but a range of values with a minimum, a maximum and an average value. Since atomic modulation functions include harmonics only up to second order and do not reveal local features, these 14 values perfectly define the curve and cover the same range (Figure 4.5). As a consequence, the crystal-chemical analysis doesn't suffer much from this uncertainty. The structure of CrOCl can be described with only 23 structural parameters, while 106 parameters are required for 3D superstructure models.

4.2.4 Crystal-chemical analysis

The superstructures of FeOCl and CrOCl are presented on Figure 4.4. Both structures reveal the antiphase buckling of M-O bilayers with pronounced variation of interlayer distances. For the crystal-chemical analysis of superstructures so-called t-plots may be used. They represent the variation of interatomic distances, bond angles, bond valences or the values of the modulation functions themselves with the phase of modulation. Furthermore, it is important to study the correlations between t-plots of different quantities. Selected t-plots are presented on the Figure 4.6. For FeOCl structural distortions lead to the formation of the fourfold superstructure and resulted in the appearance of four crystallographic sites for each atom, thus

Table 4.1: Structure refinement data.

	FeOCl	CrOCl
Number of parameters refined	38	23
R_{int} (obs/all)	5.00/5.15	6.65/6.74
No. of reflections		
(measured/unique):		
All	966/404	724/231
Main	241/101	140/44
1st order satellites	484/201	331/96
2nd order satellites	241/102	253/91
No. of observed reflections		
(all/unique):		
All	802/311	549/154
Main	211/84	126/39
1st order satellites	393/155	259/65
2nd order satellites	198/72	164/50
Robs/Rall:		
All	5.29/6.95	4.08/5.94
Main	4.00/4.60	3.69/3.94
1st order satellites	6.93/8.68	4.45/6.77
2nd order satellites	5.41/9.68	4.31/8.65

there are four points on the *t*-plots corresponding to the real structure indicated by vertical dashed lines. The largest displacements of Fe and O atoms were found along $\boldsymbol{z}$ (Figure 4.6 (a)). These displacements define the buckling of Fe-O layers. It could be noticed that the Cl atom perfectly follows the displacements of Fe. The O atom has comparable displacement amplitudes, but a different phase.

Fe and O atoms don't possess large displacements along $\boldsymbol{x}$ due to rigidity of the layers, but the Cl atom is relatively flexible within the interlayer gap (Figure 4.6(b)). While the magnitudes of atomic displacements are about 1 Å, they are correlated in a way to prevent very unfavorable short bond lengths (Figure 4.6(c)–(f)). The largest variation of bond length found is ∼0.08 Å for Fe-O bond along $\boldsymbol{y}$, which is at its longer limit at ambient pressure and therefore has more freedom. Exactly the same considerations are valid for the description of the CrOCl structure (Figure 4.6(g)–(l)). Actually, the superstructures of FeOCl and CrOCl differ only in the period of the modulation, but have similar modulation functions and can be described by the
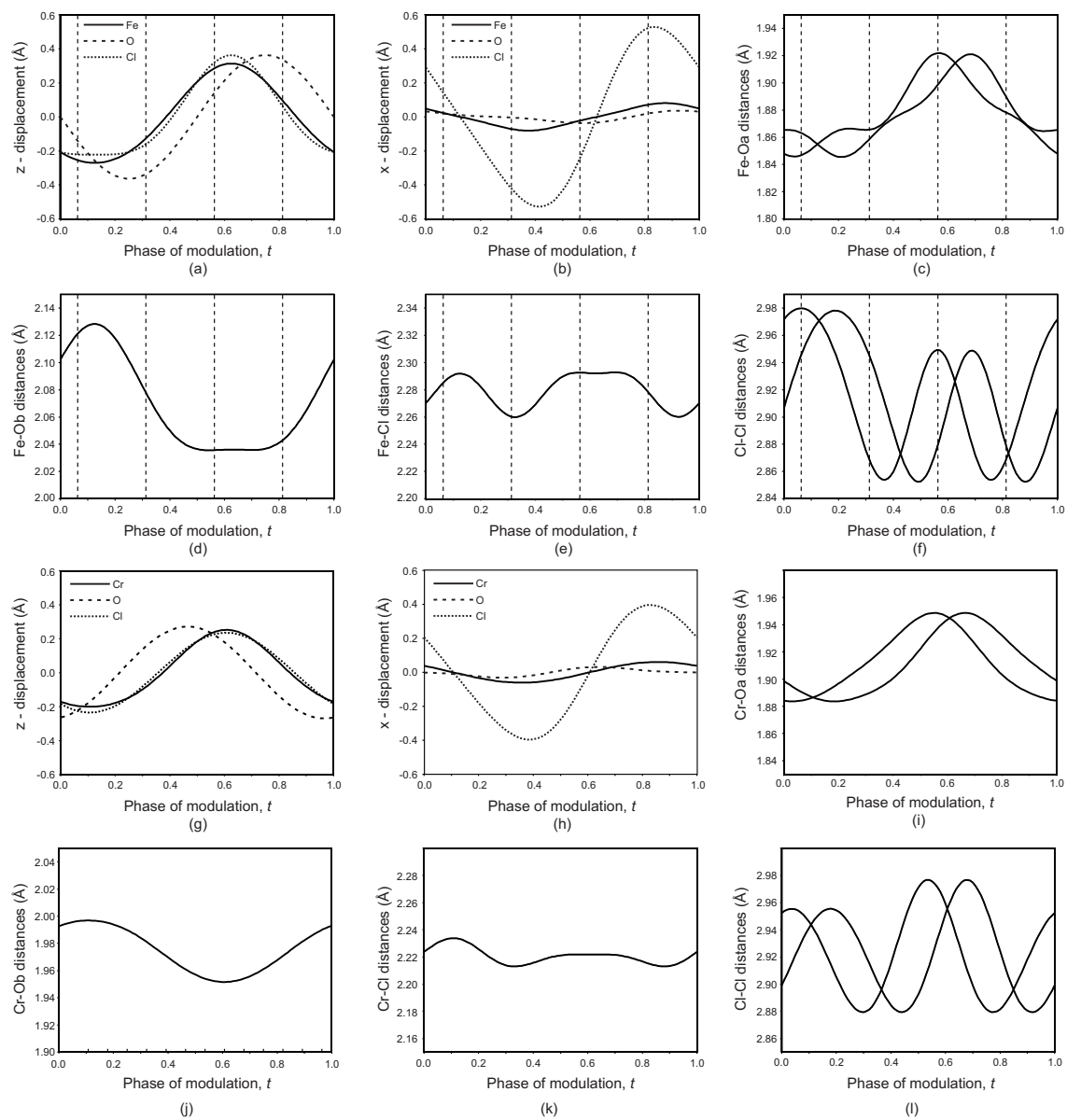
Figure 4.6: t-plots for selected interatomic distances and atomic displacements for FeOCl (a)–(f) and for CrOCl (g)–(l). Vertical dashed lines indicate commensurate t-sections. For further explanations see text.

same superspace group, since the distortion mechanism is the same.

A detailed study of t-plots of CrOCl and FeOCl towards understanding the mechanisms of the phase transitions will be given elsewhere.

4.3 Conclusions

We have demonstrated that the application of the superspace approach is useful in the analysis of high-pressure superstructures. Firstly, it helps to significantly reduce the number of refined structural parameters and to get a reliable structural model in cases when conventional structure refinement fails. Secondly, superspace tools provide an elegant way of crystal-chemical analysis. It is possible to study direct relations between the parent and distorted phases as well as between distorted phases with different modulation periods.

Chapter 5

High-pressure behavior of FeOCl[1]

5.1 Introduction

The class of isostructural layered compounds MOX (M = Ti, V, Cr, Fe; X = Cl, Br) has been recently studied for their low-dimensional magnetic properties. It was shown that the behavior strongly depends on the number of d electrons of the transition-metal atom. While FeOCl, VOCl and CrOCl exhibit antiferromagnetic ordering with different types of superstructures at low temperatures [14, 15, 17, 19–21, 38], TiOCl undergoes two phase transitions forming a spin-Peierls state below 67 K [34, 36, 37].

High-pressure studies on TiOCl and TiOBr have led to the discovery of two high-pressure phase transitions [43–45, 47, 49, 96–99]. The transition at $P_{c1} \approx$ 13–15 GPa is characterized by a sudden decrease of the semiconducting band gap and the formation of a twofold superstructure [43, 44, 47, 49]. A second pressure-induced phase transition was predicted by theory and it has been observed through the occurrence of additional superlattice reflections in X-ray powder diffraction at pressures above $P_{c2} \approx 22$ GPa [45, 49]. The origin of these phase transformations is still under discussion, but it is clear that the natures of low-temperature and high-pressure phase transitions are different.

FeOCl is a low-dimensional Mott insulator at ambient conditions [100]. The compound undergoes a paramagnetic-to-antiferromagnetic phase transition at $T_N =$ 81 K [14, 15, 17, 19]. The transition is accompanied by a monoclinic distortion of the orthorhombic lattice and the formation of an incommensurate magnetic super-

---

[1]This chapter has been published as M. Bykov, E. Bykova, S. van Smaalen, L. Dubrovinsky, C. McCammon, V. Prakapenka, and H.-P. Liermann. High-pressure behavior of FeOCl. *Phys.Rev.B* **88**, 014110 (2013).

structure [19].

Another interest of FeOCl is related to its intercalation properties. Among layered compounds with a van der Waals gap metal oxyhalides have been widely used as host lattices [23–27, 101, 102]. Intercalation enables confining guest molecules or polymer chains in a well-defined environment. The resulting intercalation hybrids often exhibit novel magnetic and electronic properties. From this point of view, application of high pressure can provide a controlled method for varying material properties. Recently it was shown that the charge transfer in polyaniline-intercalated FeOCl can be enhanced through the application of external pressure [27]. A pressure-induced increase in conductivity in the FeOCl intercalated compounds could be of interest for their application as cathode materials. Although such intercalated systems are intensively studied, there is no information on the behavior of pure FeOCl under high pressure.

Here we report the discovery of a pressure-induced phase transition of FeOCl at $P_c = 15 \pm 1$ GPa, which is preceded by extremely anisotropic lattice compression. X-ray diffraction is used to show that the high-pressure phase is a fourfold superstructure of the structure below P_c, while its lattice symmetry is reduced from orthorhombic to monoclinic. The mechanism of the phase transition is related to an anti-phase buckling of consecutive layers, resulting in regions of increased packing density of chlorine atoms of single layers and regions with interpenetrating chlorine layers, similar to soft layered materials [103]. The lowering of the symmetry at the phase transition is corroborated by Raman and Mössbauer spectroscopy. Furthermore, Mössbauer spectroscopy excludes magnetic order, while Raman spectroscopy indicates that the insulating behavior is retained at high pressures.

5.2 Experiment

Single crystals of FeOCl were prepared by gas transport from a stoichiometric mixture of $FeCl_3$ (purity 99.99%) and Fe_2O_3 (purity 99.999%) [10, 19]. Samples for the Mössbauer experiment ($\sim 66.6\%$ enriched in ^{57}Fe) were synthesized using a mixture of $FeCl_3$ and $^{57}Fe_2O_3$.

Pressure-dependent angle-dispersive powder X-ray diffraction measurements were carried out at beamline 13ID-D of the Advanced Photon Source (Chicago, USA) using monochromatic radiation of wavelength 0.3344 Å. The sample was put into a diamond anvil cell (DAC) with 250 μm diamond culets. A Re gasket with initial thickness 29 μm and 125 μm hole diameter was used. Ne served as a pressure-transmitting medium. Pressure was determined by the change of the

lattice parameters of Au using the equation of state reported by Fei et al. [64]. Diffraction patterns were collected with a Mar165 CCD detector and integrated with FIT2D [104]. Le-Bail fits were performed with the JANA2006 [88] for the determination of the lattice parameters as a function of pressure.

A single-crystal X-ray diffraction experiment was performed at beamline P02.2 of PETRA III (Hamburg, Germany), employing a wavelength of 0.29004 Å and pressures of 15.0 and 22.7 GPa. A BX90 DAC [60] with a large opening angle of 4θ = 80° was used together with 250 μm Boehler-Almax diamonds, a Re gasket with 29 μm initial thickness and 130 μm hole, and Ne as a pressure-transmitting medium [61]. Diffracted intensity was collected on a Mar345 image plate detector and then processed with the $CrysAlis^{Pro}$ software package [50], resulting in integrated intensities for 106 main reflections and 200 first-order satellite reflections (15 GPa data set), and 101 main reflections, 201 first-order and 102 second-order satellite reflections (22.7 GPa data set).

Raman scattering experiments were performed with a LabRam spectrometer (resolution 2 cm^{-1}), equipped with a 15 mW HeNe laser (wavelength 632.8 nm) and a 50X objective. The pressure was measured by ruby fluorescence [63]. Raman spectra were measured with the sample in a DAC at 13 selected pressures in the range 3–38 GPa.

^{57}Fe Mössbauer spectra were recorded at room temperature in transmission mode on a constant acceleration Mössbauer spectrometer with a nominal 370 MBq ^{57}Co source in a 12-μm-thick Rh matrix. The velocity scale was calibrated relative to a 25-μm-thick α-Fe foil. Spectra were measured at five selected pressures between 0 and 19.5 GPa. Each spectrum took 4 to 7 days to collect. Peaks were described by Lorentzian line shapes using the software package MOSSA [105].

5.3 Results

5.3.1 Powder X-ray diffraction

The powder X-ray diffraction patterns could be indexed according to the orthorhombic FeOCl lattice with space group $Pmmn$ (Fig. 5.1). However, a significant broadening of the diffraction maxima was observed in patterns collected at pressures above 15 GPa. Furthermore, the pressure dependencies of the lattice parameters exhibit small anomalies at the same pressure, resulting in apparently different compressibilities above and below 15 GPa (Fig. 5.2(c)). Most notable is the very small pressure dependence of a at high pressures, with a nearly constant value within the range
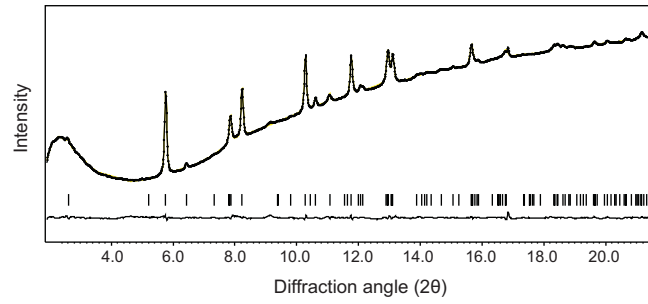
Figure 5.1: Powder X-ray diffraction diagram at 4.9 GPa together with the Le Bail fit and the difference between measured and calculated intensities (lower trace). Vertical bars show the calculated peak positions.
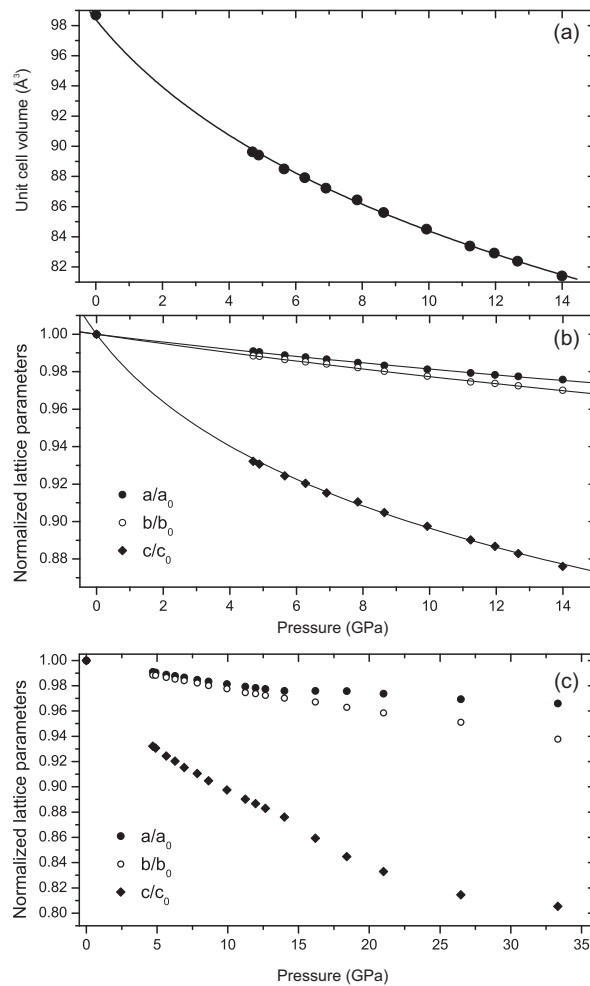
Figure 5.2: (a) Pressure dependence of the unit cell volume. (b) Pressure dependence of normalized lattice parameters in the range 0–15 GPa. Solid curves represent the fits of Eq. (5.1) to the experimental data. (c) Pressure dependence of the normalized lattice parameters over the whole pressure range studied.

Table 5.1: Linear and volume bulk moduli of FeOCl.

	K_0 (GPa)	K_0'
Volume	36(3)	8.2(8)
a-axis	153(4)	5.3(9)
b-axis	127(6)	4.0[1]
c-axis	13.0(5)	4.9(2)

[1] fixed

15–18 GPa.

These effects suggest the occurrence of a phase transition at ∼15 GPa, as it is confirmed by Raman and Mössbauer spectroscopies and single-crystal X-ray diffraction (see below). However, the weak anomalies do not constitute proof of a phase transition by themselves, because non-hydrostatic conditions above 15 GPa for neon as pressure-transmitting medium [106], might also contribute to apparent anomalies in pressure-dependent experiments. In addition, the present powder X-ray diffraction experiments failed to detect the structural changes as observed by single-crystal X-ray diffraction (Section 5.3.3), mainly due to extremely preferred orientation of the sample, with the platelike crystallites lying flat on top of the diamonds, resulting in the **c**-axis being parallel to the X-ray beam.

The volume-pressure dependence up to 14 GPa was described with a third-order Birch-Murnaghan equation of state (Fig. 5.2(a)) [107]:

$$P = 3K_0 f_E (1 + 2f_E)^{\frac{5}{2}} (1 + 3/2(K_0' - 4)f_E), \tag{5.1}$$

where $f_E = [(V/V_0)^{-2/3} - 1]/2$. The fit to the data resulted in the bulk modulus $K_0 = 36\,(3)$ GPa, zero-pressure volume $V_0 = 98.3\,(4)$ Å^3 and $K_0' = 8.2\,(8)$.[1]

For the description of linear compressibilities the parametric form of the Birch-Murnaghan equation of state was used, substituting the cube of the lattice parameter for the volume [108]. Both the graphical representation (Fig. 5.2(b)) and the bulk moduli (Table 5.1) indicate an extremely anisotropic compressibility.

5.3.2 Raman spectroscopy

The full representation of the vibrational modes of FeOCl in space group *Pmmn* is:

$$\Gamma_{tot} = 3A_g + 2B_{1u} + 3B_{2g} + 2B_{2u} + 3B_{3g} + 2B_{3u}. \tag{5.2}$$

---

[1]Ambient-pressure lattice parameters were taken from Ref. [19], where crystals of FeOCl were synthesized employing the same technique, equipment and reagents as in the present study.
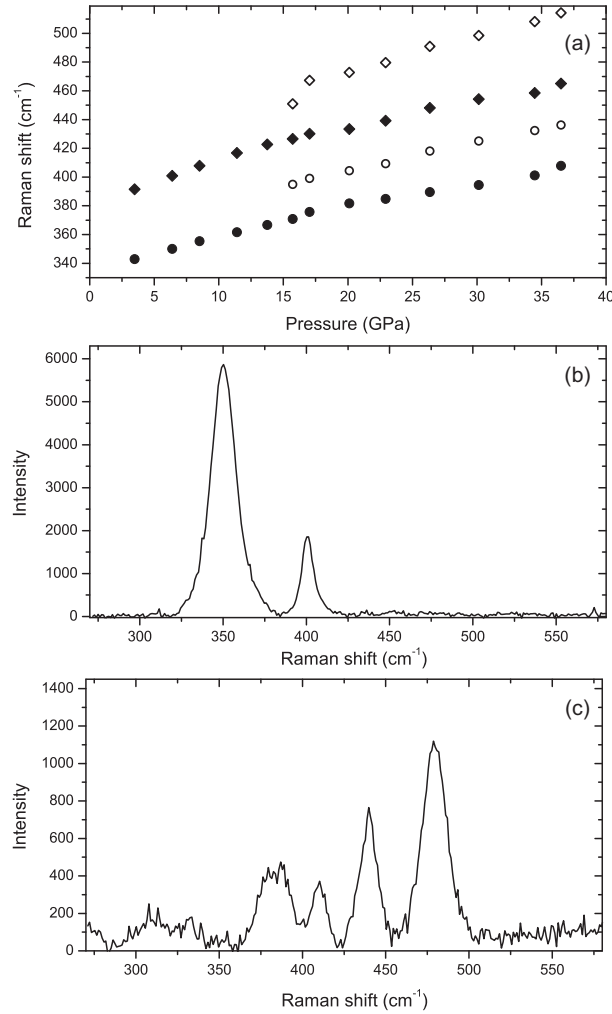
Figure 5.3: (a) Pressure dependence of Raman peak shifts of FeOCl. At pressures above 15 GPa, additional peaks were observed (open symbols). (b) Raman spectra at 6.4 GPa and (c) at 23.0 GPa.

The modes with symmetries A_g, B_{2g}, and B_{3g} are Raman active. Two strong modes have been observed in the Raman spectra taken at low pressures (Fig. 5.3(b)). They can be identified with A_g modes according to Ref. [109]. Their Raman shifts gradually increase with pressure up to 15 GPa (Fig. 5.3(a)). Two additional modes are present in Raman spectra at pressures above 15 GPa (Fig. 5.3(a,c)). This confirms a phase transition at $\sim$15 GPa, and it suggests a lowering of crystal symmetry at the transition, in agreement with the results of single-crystal X-ray diffraction.

The observation of resonance peaks in the Raman spectra indicates that FeOCl is non-metallic at all pressures. Visual inspection of the sample within the DAC showed FeOCl to remain transparent, a further indication for the insulating character at all

pressures.

5.3.3 Single-crystal X-ray diffraction

Superlattice reflection were observed in the diffraction at both pressures, 15.0 and 22.7 GPa. Most conveniently, the superstructure can described by a non-conventional B-centered, eightfold $4a \times b \times 2c$ pseudo-orthorhombic supercell. Due to unavoidable incompleteness of the data arising from limitations imposed by the DAC, the superspace approach [52, 110] can be used to increase the ratio between the number of unique reflections and the number of refined parameters. Within this approach the high-pressure structure of FeOCl can be described by the orthorhombic superspace group $Pmmn(\sigma_1, 0, \frac{1}{2})00s$ (No. 59.1.10.6 with standard setting $Pmnm(0, \frac{1}{2}, \sigma_3)000$) [93, 94] and commensurate modulation wavevector $\mathbf{q} = (\frac{1}{4}, 0, \frac{1}{2})$.

The crystal structure is described by the coordinates of the three unique atoms, $\mu = $ Fe, O, Cl, with respect to the orthorhombic basic-structure unit cell, with $a(15) = 3.675(8)$, $b(15) = 3.191(2)$ and $c(15) = 6.803(10)$ Å at 15 GPa, and $a(22.7) = 3.631(2)$, $b(22.7) = 3.170(1)$ and $c(22.7) = 6.551(15)$ Å at 22.7 GPa. Positions of the atoms in the superstructure are then obtained as the sum of the basic-structure position $\bar{\mathbf{x}}(\mu)$ and values of the modulation functions $\mathbf{u}^\mu(\bar{x}_4)$:

$$\mathbf{x}(\mu) = \bar{\mathbf{x}}(\mu) + \mathbf{u}^\mu(\bar{x}_4), \tag{5.3}$$

where $\bar{x}_4 = t + \mathbf{q} \cdot \bar{\mathbf{x}}(\mu)$, and the parameter t represents the phase of the modulation. Displacive modulations of atom μ are described by truncated Fourier series:

$$u_i^\mu(\bar{x}_4) = \sum_{n=1}^{n_{max}} A_i^n(\mu) \sin(2\pi n \bar{x}_4) + B_i^n(\mu) \cos(2\pi n \bar{x}_4), \tag{5.4}$$

for $i = x, y, z$, with $n_{max} = 1$ for 15.0 GPa, and $n_{max} = 3$ for 22.7 GPa.

The atomic coordinates of the ambient-pressure $Pmmn$ structure model of FeOCl were used as starting point for the refinements of the basic structures against main reflections at both pressures [111]. Subsequently, modulation parameters $A_i^n(\mu)$ and $B_i^n(\mu)$ were given arbitrary but small starting values. Refinement of all parameters against all reflections exhibited a smooth convergence, eventually leading to good fits to the diffraction data with $R_{all} = 0.0578$, $R_{main}=0.0443$ and $R_{sat1}=0.1053$ at 15.0 GPa, and $R_{all} = 0.0529$, $R_{main}=0.0400$, $R_{sat1}=0.0693$ and $R_{sat2} = 0.0541$ at 22.7 GPa (sat1 and sat2 refer to first- and second-order satellite reflections, respectively).

Different sections t of superspace lead to different symmetries of the $4a \times b \times 2c$ supercell. They are Bm, $B2_1/m$ (both are $\mathbf{b}$-unique) and $Bmm2$. The best fit to the
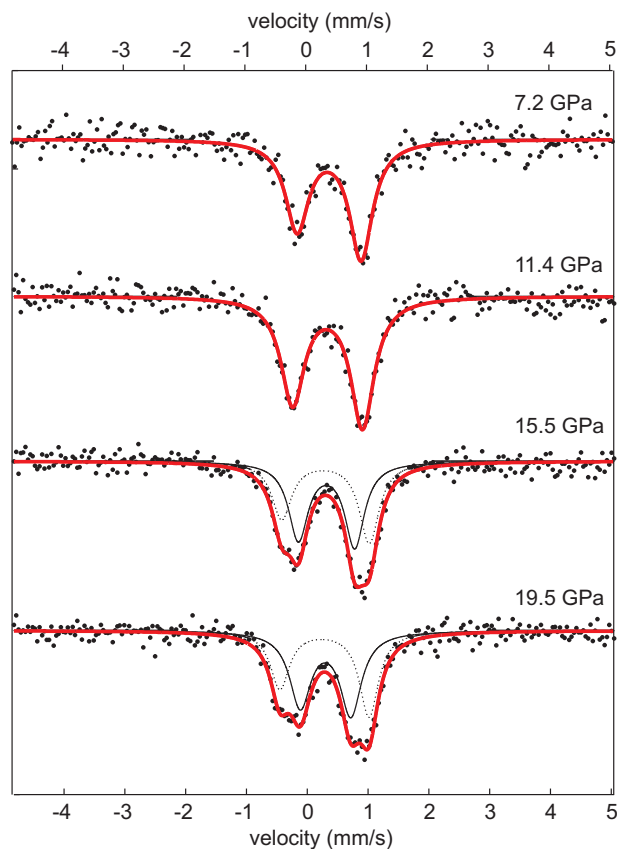
Figure 5.4: High-pressure Mössbauer spectra of ^{57}Fe measured on FeOCl powder samples in a DAC.

diffraction data was achieved for $t = \frac{1}{16}$, which corresponds to the centrosymmetric, monoclinic space group $B2_1/m$ (No. 11 with standard setting $P2_1/m$) [95].

The possible symmetries are the same as those implied by the irreducible representation A3 of space group $Pmmn$ at $\mathbf{k} = (\frac{1}{4}, 0, \frac{1}{2})$, which defines the symmetry of the primary distortion for this phase transition [112]. The necessity of high-order harmonics ($n_{max} = 3$) within the superspace approach means that in addition to the primary order parameter, secondary order parameters contribute to the structural distortion at higher pressures without further symmetry breaking.

5.3.4 Mössbauer spectroscopy

The Mössbauer spectra below 15 GPa exhibit a single doublet, which can perfectly be fitted by a pair of Lorentzian functions (Fig. 5.4). The center shift (CS) of the Fe^{3+} doublet is consistent with its octahedral coordination and with previous studies at ambient conditions [113]. The observed decrease of the CS with pressure
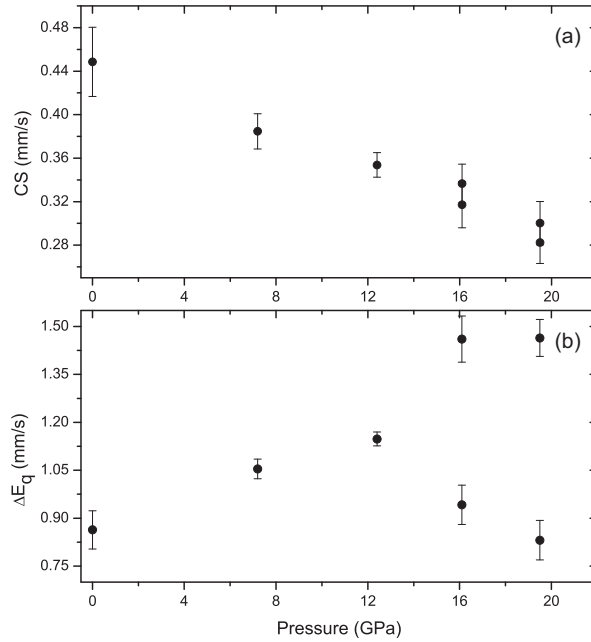
Figure 5.5:   Pressure dependence of (a) the CS, and (b) the quadrupole splitting in Mössbauer spectra.

(Fig. 5.5(a)) is in agreement with the expected increase in s-electron density at the nucleus. Spectra at pressures above 15 GPa did not show any evidence of magnetic ordering. However, they cannot be described by a single doublet. Instead, they show two, partially overlapping doublets with nearly equal CSs and different quadrupole splittings, indicating the presence of more than one independent Fe site, in agreement with the model for the superstructure.

5.4   Discussion

5.4.1   Anisotropic compressibility

The large anisotropy of the compressibility is related to the layered crystal structure of FeOCl. The structure can be described in terms of Fe-O double layers sandwiched between Cl layers thus forming slabs that are stacked along the crystallographic **c** axis [111]. The slabs are formed by sharing O–O and O–Cl edges of the distorted cis-FeO$_4$Cl$_2$ octahedra and they are connected by weak van der Waals interactions (Fig. 5.6). The latter directly explain that the compressibility along the **c**-axis is several times larger than that along the **a** and **b** axes (Fig. 5.2).

A quantitative analysis of the crystal structures shows that the interlayer Cl–Cl
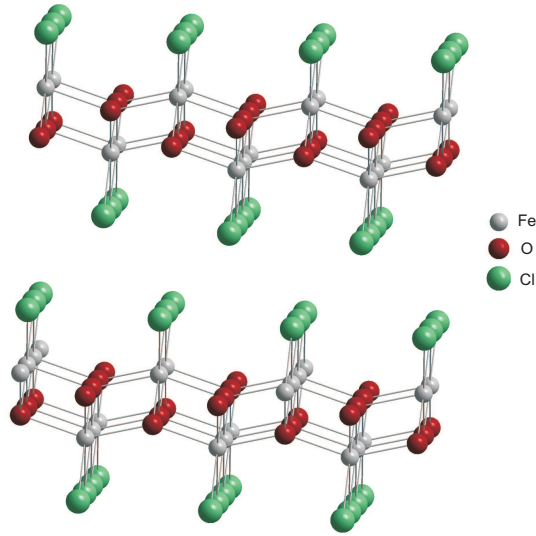
Figure 5.6: Basic structure of FeOCl. Layered crystal structure consisting of Fe-O double layers sandwiched by chlorine layers and separated by van der Waals gaps.

distance at ambient pressure, 3.680 Å, is close to twice the van der Waals radius of chlorine. The linear compressibility along **c** is in a good agreement with the compressibility of molecular Cl_2 (K_0 = 14.2 (24) GPa) reported by Dusing et al. [114], and with the linear compressibilities of layered $FeCl_2$ (K_0 = 16(3) GPa) and TiOCl (K_0=12(1) GPa) [49, 115]. These similarities show that the linear bulk moduli of FeOCl (Table 5.1), $FeCl_2$ and TiOCl and the volume bulk modulus of Cl_2 directly represent the compressional behavior of Cl–Cl van der Waals bonds. Differences between these values arise from differences in the packing of Cl atoms within the layer, from different partial charges on Cl atoms, and from the rigidity of layer backbone itself.

The compressibility along **a** reflects the reduction of Fe–O distances. Since chemical bonds are the least compressible feature of crystal structures, this explain that **a** is the most incompressible direction in FeOCl (Table 5.1). On the other hand, the compressibility along **b** is related to the contraction of the Fe_2OCl quadrangles, which is achieved through a pressure dependence of Fe–O–Fe and Fe–Cl–Fe bond angles. Bond angles are generally more soft than bond lengths are.

Table 5.2: Atomic displacements (Å) from the basic structure positions along **a** and **c** axes at 15.0 and 22.7 GPa.

Atom	x-15GPa	x-22.7GPa	z-15GPa	z-22.7GPa
Fe1	0.015	0.026	-0.11	-0.25
Fe2	-0.036	-0.074	-0.05	-0.13
Fe3	-0.015	-0.025	0.11	0.29
Fe4	0.036	0.073	0.05	0.09
O1	0.034	0.036	-0.06	-0.14
O2	-0.014	-0.015	-0.14	-0.33
O3	-0.034	-0.036	0.06	0.14
O4	0.014	0.015	0.14	0.33
Cl1	0.035	0.115	-0.17	-0.25
Cl2	-0.153	-0.407	-0.03	-0.12
Cl3	-0.132	-0.237	0.12	0.33
Cl4	0.250	0.529	0.09	0.04

5.4.2   High-pressure crystal structures

The high-pressure phase of FeOCl contains four crystallographic sites for each atom (denoted as Fe1–Fe4, Cl1–Cl4 and O1–O4), while the atomic connectivity and co-ordination numbers remain the same as those of the crystal structure at ambient conditions. Mössbauer spectra distinguishes only two Fe sites of different quadrupole splittings (Fig. 5.4). This discrepancy is explained by the details of the superstructures as defined by the atomic shifts out of the basic *Pmmn* structure. Iron and oxygen atoms pairwise have shifts of nearly equal magnitude and opposite direction (Table 5.2), thus suggesting pairwise similar quadrupole fields at the Fe sites. The four chlorine atoms all have different shifts that reflect the greater flexibility of these atoms within the van der Waals gaps.

The superstructures of FeOCl at pressures of 15.0 and 22.7 GPa are compared to the structure at ambient conditions in Fig. 5.7. The superstructures reveal an antiphase buckling of the Fe–O bilayers, with a noticeable variation of the interlayer distances that increases with pressure. Fe and O atoms do not possess large displacements along **a** due to the rigidity of the Fe–O bonds (Section 5.4.1). However, the buckling of the layers is clearly represented by in-phase displacements of Fe and O atoms along **c** (Table 5.2). It can be related to a variation of the Fe–O–Fe bond angles (Table 5.3). The compression of FeOCl is mainly determined by a decrease of the Cl–Cl distances (Table 5.3). Within the high-pressure phase this affects both interlayer and intralayer distances, as it is governed by the large displacements of the chlorine atoms (Table 5.2).
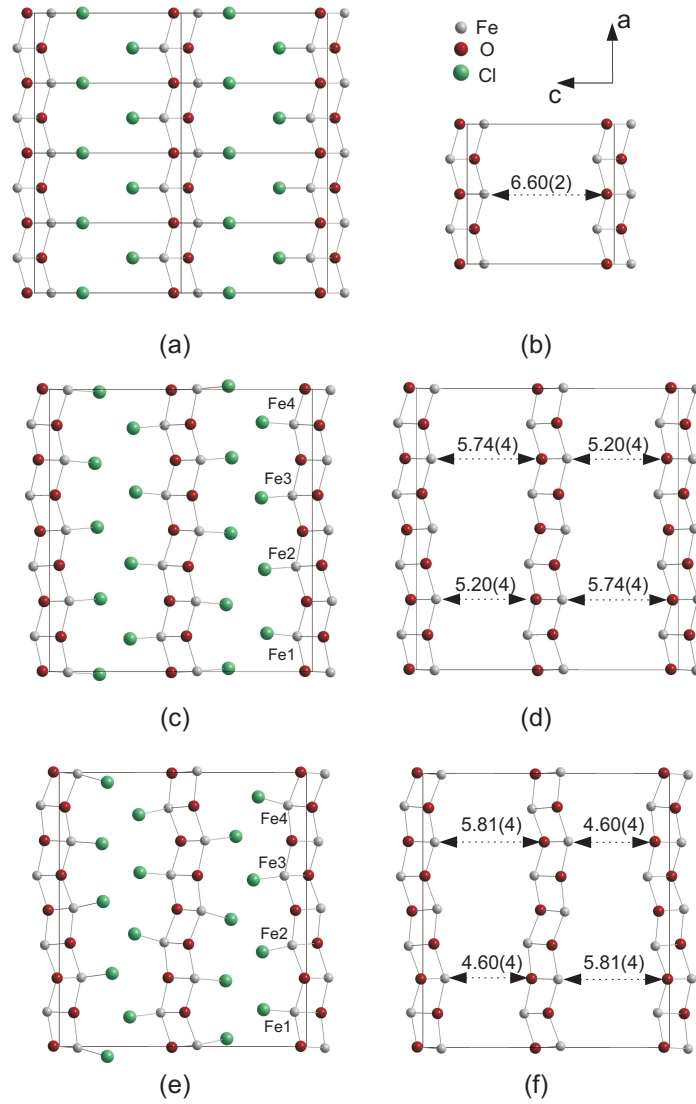
Figure 5.7: (a) Projection along **b** of the crystal structure of FeOCl at ambient conditions. (b) Distance (Å) between Fe–O double layers within the ambient phase. Chlorine atoms are not shown. (c) Projection along **b** of the high-pressure crystal structure at 15.0 GPa. (d) Minimum and maximum distances (Å) between Fe–O double layers in the high-pressure phase at 15 GPa. Chlorine atoms are not shown. (d) Projection along **b** of high-pressure crystal structure at 22.7 GPa. (e) Minimum and maximum distances (Å) between Fe–O double layers in the high-pressure phase at 22.7 GPa. Chlorine atoms are not shown.

Table 5.3:   Selected interatomic distances (Å) and angles (deg). Given are the average values (Ave), the minimum and maximum values for the high pressure phase at 15.0 and 22.7 GPa as well as distances and angles for the ambient pressure phase (AP).

	15 GPa			22.7 GPa			AP
	Min	Max	Ave	Min	Max	Ave	
Fe-Fe	3.007(14)	3.031(13)	3.018(13)	2.960(20)	3.026(18)	2.993(19)	3.104(1)
Fe-Fe[1]	3.191(2)	3.191(2)	3.191(2)	3.170(1)	3.170(1)	3.170(1)	3.3046(7)
Fe-O[2]	1.85(2)	1.92(2)	1.89(2)	1.84(3)	1.92(3)	1.88(3)	1.964(8)
Fe-O[1]	2.059(14)	2.099(15)	2.079(13)	2.036(13)	2.116(13)	2.067(12)	2.100(10)
Fe-Cl	2.231(19)	2.31(2)	2.277(19)	2.27(2)	2.31(12)	2.28(2)	2.368(7)
Cl-Cl[3]	2.97(3)	3.06(3)	3.01(3)	2.91(3)	2.89(3)	2.92(3)	3.680(3)
O-Fe-O[2]	151.5(10)	152.1(10)	151.8(10)	150.1(9)	154.4(11)	152.8(10)	148.35(4)
Fe-O-Fe[2]	147.6(13)	155.9(13)	151.8(12)	143.5(11)	161.8(11)	152.8(11)	148.35(4)

[1] Along **b**-axis

[2] Along **a**-axis

[3] Interlayer distance

Higher pressures lead to a noticeable increase of the amplitudes of atomic displacements, and the regions of layer separation and interpenetration become more pronounced (Fig. 5.7). One can expect a saturation of the modulation amplitudes at higher pressures. However, we could not continue single-crystal diffraction studies at higher pressures, because the crystal was destroyed in our experiment by pressures higher than 22.7 GPa.

5.4.3   Mechanism of the phase transition

We propose that the driving force of the phase transition is related to the Cl–Cl interactions. At ambient conditions the interlayer Cl–Cl distances are close to the sum of their van der Waals radii, while the intralayer Cl–Cl distances are larger, because they are defined by rigid Fe–O framework. So, FeOCl is to a certain extent a frustrated system, since an optimal packing of Cl atoms is not realized. Up to P_c, the packing density of chlorine is increased by a large decrease of interlayer Cl–Cl distances. The Fe–O framework is much more rigid, so that the intralayer Cl–Cl van der Waals contacts are hardly affected by pressure. The distortions defining the superstructure of the high-pressure phase allow an increase of both the interlayer and intralayer packing density in two ways. Firstly, regions exist of increased intralayer Cl–Cl distances. This allows for interpenetration of layers and each Cl atom of one layer is exclusively coordinated to Cl atoms of the neighboring layer. Within the other regions, the intralayer Cl–Cl distances are decreased, such that their distances

are optimized. The antiphase buckling of the layers within the high-pressure phase leads to both types of regions, as it is apparent from Fig 5.7(c)-(f). Thus, initially soft van der Waals Cl–Cl distances are optimized in such a way that their variation at high pressures is comparable to the variations of the lengths of the rigid Fe–O bonds (Table 5.3). This situation is similar to that observed at low temperatures for soft layered materials $(C_3H_7NH_3)_2MCl_4$ with $M =$ Cu, Mn [103].

The proposed mechanism for the high-pressure phase transition of FeOCl is essentially different from the mechanism proposed for TiOCl, where the phase transition is attributed to spin-Peierls-like interactions between Ti^{3+}, followed by the formation of superstructures, involving doubling of $\mathbf{b}$ and alternation of Ti-Ti distances [47]. The symmetry of the single filled d orbital of Ti^{3+} allows exchange interactions along the Ti chains parallel to $\mathbf{b}$ only, and thus is responsible for the formation of the spin-Peierls state [34, 35]. On the other hand, Fe^{3+} has five unpaired d-electrons. The additional electrons enter d-orbitals of different symmetries that are responsible for strong interchain exchange interactions on the ab plane [113, 116]. Accordingly, antiferromagnetic order is energetically preferred over the formation of spin-singlet pairs. The observed $4a \times 1b \times 2c$ supercell of FeOCl does not allow for a variation of Fe–Fe distances along the ribbons parallel to $\mathbf{b}$ (Table 5.3), and it thus is in agreement with the absence of spin-singlet pairs within the high-pressure phase.

The structural phase transition of FeOCl does not bear obvious relations to a supposed insulator-metal transition. Raman spectroscopy has indicated the insulating character of FeOCl at all pressures. However, the continuous reduction of Fe–Fe distances and the changes of Fe–O–Fe bond angles certainly may affect the band structure and may lead to a reduction of a band gap. They do not exclude the possibility of metallization at even higher pressure than considered in the present work.

On the other hand, the proposed model of partial interpenetration of chlorine layers may also contribute to the pressure-induced phase transitions in TiOCl. This alternative interpretation of the mechanism of the transition in TiOCl may explain the discrepancies between experimental data on high-pressure behavior of TiOCl from different sources. In this regard, high-pressure single-crystal X-ray diffraction of TiOCl would be highly desirable.

5.5 Conclusions

We have discovered a pressure-induced phase transition of FeOCl at $P_c = 15\pm1$ GPa. The phase transition is preceded by an extremely anisotropic lattice compression,

which is explained by the gradual collapse of the Van der Waals gap between the chlorine atoms at the borders of the slabs of this layered compound.

Crystal structures obtained by high-pressure single-crystal X-ray diffraction have been used to derive a microscopic mechanism of the phase transition. It is proposed that the high-pressure phase attains a denser packing of the chlorine atoms through a buckling of the layers. Consecutive layers with antiphase buckling lead to regions of increased packing density of Cl atoms within single layers and other regions with increased distances between these Cl atoms, then allowing for interpenetration of the chlorine layers of neighboring slabs (Fig. 5.7).

Spectroscopic evidence has been obtained, which shows that the high-pressure phase transition of FeOCl is not related to the development of magnetic order or to metallization of this material. The mechanism proposed here for the high-pressure phase transition of FeOCl might also play a role in the high-pressure phase transitions of TiOCl. Understanding the high-pressure behavior of TiOCl would greatly benefit from high-pressure single-crystal X-ray diffraction experiments.

Chapter 6

Pressure-induced normal-incommensurate and incommensurate-commensurate phase transitions in CrOCl[1]

The discovery of high-pressure phases of the elements with unexpectedly complex guest-host and incommensurate structures [51, 117–120] put an end to the myth, that atomic arrangements are simplified under high degrees of compression. For complex compounds systematic studies of incommensurate structures are lacking. Employing single-crystal X-ray diffraction in a diamond anvil cell we show that layered CrOCl [20] possesses an incommensurate phase for 16 – 51 GPa and lock-in phases at higher pressures. Detailed and accurate structural studies reveal that the complex behavior of CrOCl is governed by non-bonded interactions between chlorine atoms, with the incommensurability resulting from the competition between optimizing intra- and interlayer Cl–Cl distances and the general trend towards denser packings. Isostructural FeOCl exhibits the same phase sequence, but with a much narrower pressure range for its incommensurate phase. Similar high-pressure behavior can be expected for other materials containing different chemical bonds or atomic groups with individual compression behaviors.

In the past decade high-pressure diffraction experiments have uncovered a new type of behaviour of materials at extreme conditions. Contrary to the expectation

---

that on increasing pressure materials should approach high-symmetry close-packed structures, a number of elements possess extraordinary complex incommensurately modulated or self-hosting composite structures at high pressures [51, 117–119]. The occurrence of these structures has been rationalized in terms of electronic instabilities [51, 119, 121]. Generally, incommensurate structures may appear at high pressures as the result of shifts of the transition temperatures of normal-to-incommensurate phase transitions towards room temperature. This mechanism leads to similar crystal structures for the high-pressure and low-temperature phases, as it has been found in charge-density-wave systems [122, 123] and ferroelectrics [124, 125]. Incommensurability as an intrinsic high-pressure effect is described here for the first time for the compound CrOCl.

Isostructural transition metal oxychlorides MOCl (M = Ti, V, Cr, Fe) are of particular interest, because they form model systems for studies of the dependence of magnetic properties on the atomic magnetic moments of M^{3+} within a single structure type. Anisotropic magnetic interactions, magnetic frustration and strong magneto-elastic coupling have resulted in a variety of complex magnetically ordered phases at low temperatures [19–21, 34, 36]. TiOCl undergoes a phase transition at a pressure of approximately 10–15 GPa towards a twofold superstructure that is reminiscent of the superstructure of the spin-Peierls phase at low temperatures [47, 49]. A second phase transition takes place at higher pressures [45], but the powder X-ray diffraction data were of insufficient quality for a structural characterization of the high-pressure phase [49]. Recently, we have developed a methodology of accurate single-crystal X-ray diffraction studies of complex oxychlorides structures at high pressures [126], and demonstrated its efficiency particularly in an investigation of the fourfold superstructure of FeOCl up to 35 GPa [127].

We have now measured single-crystal X-ray diffraction of CrOCl up to a pressure of 56 GPa, employing synchrotron radiation at beamline ID09A of the ESRF (on compression) and at beamline P02.2 of PETRA at DESY (on decompression). Analysis of these data has provided an accurate description of the pressure dependence of the crystal structures of CrOCl (Fig. 6.1). The ambient phase with orthorhombic symmetry *Pmmn* persists up to 13 GPa. A fit of a Vinet equation of state to the volumes of the unit-cell resulted in a bulk modulus $K_0 = 29(2)$ GPa and its derivative $K_0' = 9.5(1)$. The compressibility is highly anisotropic, with a compression that is much larger in the direction perpendicular to the layers (along **c**) than in directions parallel to the layers (within the **a**, **b** plane; Fig. 6.2). This feature can be understood from the crystal structure of MOCl, which is a stacking along the **c**-axis of slabs MOCl that are connected through weak Cl$\cdots$Cl Van der Waals bonds
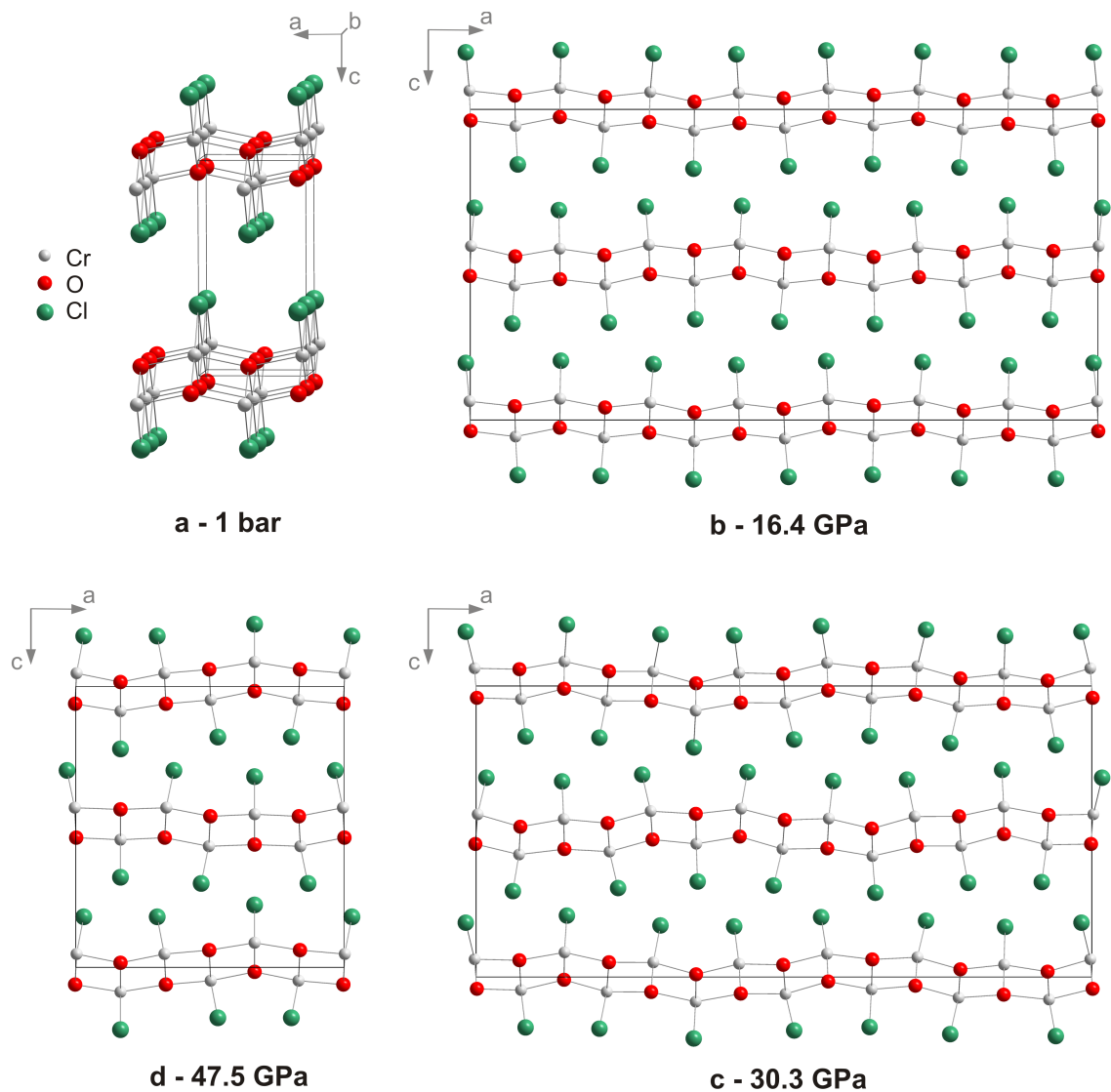
Figure 6.1: Crystal structures of CrOCl at different pressures. (a) Ambient-pressure crystal structure. Perspective view along the b-axis. (b) Approximate $7a \times b \times 2c$ superstructure at 16.4 GPa. (c) Approximate $7a \times b \times 2c$ superstructure at 30.3 GPa. (d) $3a \times b \times 2c$ superstructure at 47.5 GPa as obtained on decompression.
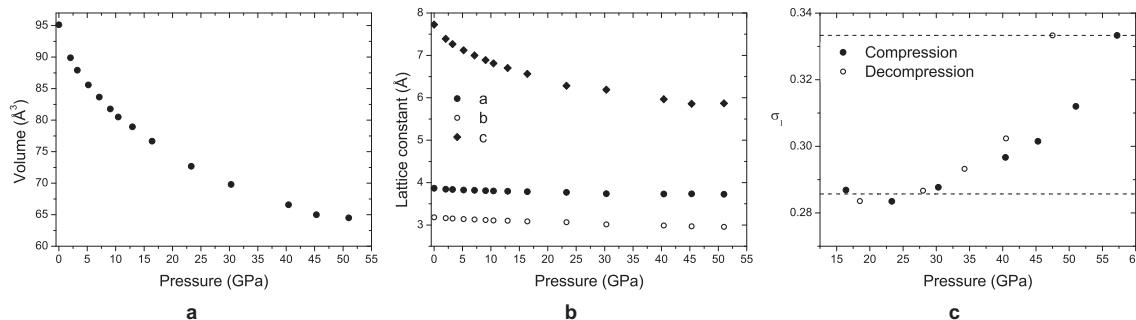
Figure 6.2:   Pressure dependencies of CrOCl unit-cell volume (a), lattice parameters (b) and of the σ_1 component of the $\mathbf{q}$-vector. Dashed lines indicate rational values $\frac{2}{7}$ and $\frac{1}{3}$.

(Fig. 6.1a). Bond energies of the latter possess a much more shallow dependence on the interatomic distance than those of chemical bonds M–O and M–Cl, and they are therefore much more compressible (Fig. 6.3). The anisotropic compression of CrOCl and FeOCl [127] is similar up to 13 GPa and thus supports a common origin for this behavior.

Evidence for a phase transition occurring between 15.3 and 16.4 GPa is provided by Raman scattering (Appendix A) and X-ray diffraction. Diffraction patterns contain superlattice reflections at 16.4 GPa and higher pressures. All Bragg reflections can be indexed on the basis of a unit cell that is closely related to the unit cell of the lattice at ambient conditions, together with a modulation wave vector $\mathbf{q} = (\sigma_1, 0, \frac{1}{2})$. At pressures below 30 GPa, σ_1 is close to the rational number $\frac{2}{7} = 0.2857$ (Fig. 6.2c). However, the pressure dependence of the σ_1 component of the $\mathbf{q}$-vector above 30 GPa unambiguously demonstrates the incommensurability of the modulation within this high-pressure phase. The crystal structures were obtained within the superspace approach through refinements against the measured diffraction data at each pressure (see Methods and Appendix A).

The occurrence of a normal-to-incommensurate phase transition can be explained by the collapse of the Van der Waals gap. It was shown for a number of organic and organometallic compounds, that increasing pressure primarily reduces the lengths of the weak intermolecular Van der Waals bonds. However, when these distances reach a lower limit, initially weak interactions approach a strongly repulsive region of the interatomic potential. A further increase of pressure then induces a phase transition, which results in a redistribution of these contacts and thus diminishes the free energy [128]. It was noticed that the lower limit can be estimated as the shortest distance in ambient-pressure structures, e.g. as they can be found in the Cambridge Structural Database (CSD)[129, 130]. For inter-molecular Cl···Cl contacts, the three shortest distances in the CSD (version November 2013) are 2.961 Å (CEBFEV [131]), 3.027
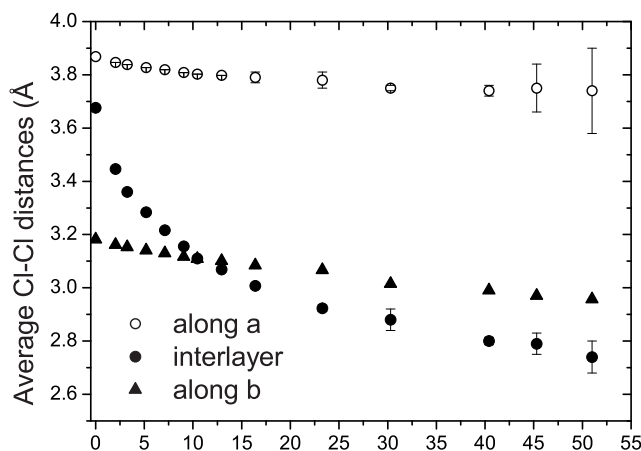
Figure 6.3: Pressure dependence of the Cl···Cl distances in CrOCl. For pressures above 15 GPa distances are the average distance over the phase t of the modulation. If error bars are not shown, they are smaller than the size of the symbol.

Å (LENDEP [132]) and 3.028 Å (YUHNIY [133]). Thus, a phase transition may be expected when interlayer Cl···Cl distances in MOCl reach a limit of about 3.0 Å. Interlayer Cl···Cl Van der Waals contacts become the shortest Cl···Cl distances above ∼11 GPa (Fig. 6.3). At 12.95 GPa (the highest pressure below the phase transition at which diffraction was measured) this distance is 3.069 Å, close to the limit of 3.0 Å. The observation of a phase transition at 15.9 ± 0.6 GPa thus is in complete agreement with the behaviour of molecular crystals. It is demonstrated below, that the incommensurate crystal structure allows for a further compression of the compound without the need to shorten the Cl···Cl contacts significantly. Average interlayer Cl···Cl distances are nearly equal at equal pressures for CrOCl and FeOCl [127] (Table A.7 in Appendix A), while both compounds exhibit phase transitions at nearly equal pressures. These observations reinforce the conclusion of a common origin for the high-pressure behavior of these compounds.

Within the MOCl structure type, the intralayer Cl···Cl distance along **a** is determined by the geometry of the poorly compressible M–O framework at the center of each slab. So, at pressures, where the interlayer Cl···Cl distance reaches the limit of 3 Å, the intralayer Cl···Cl distance along **a** is, with 3.8 Å, still larger than twice van der Waals radius of Cl (Fig. 6.3). On the local scale (taking into account only one pair of neighboring slabs), this space between Cl atoms can be used in two different ways to achieve a denser packing of Cl atoms. In the first
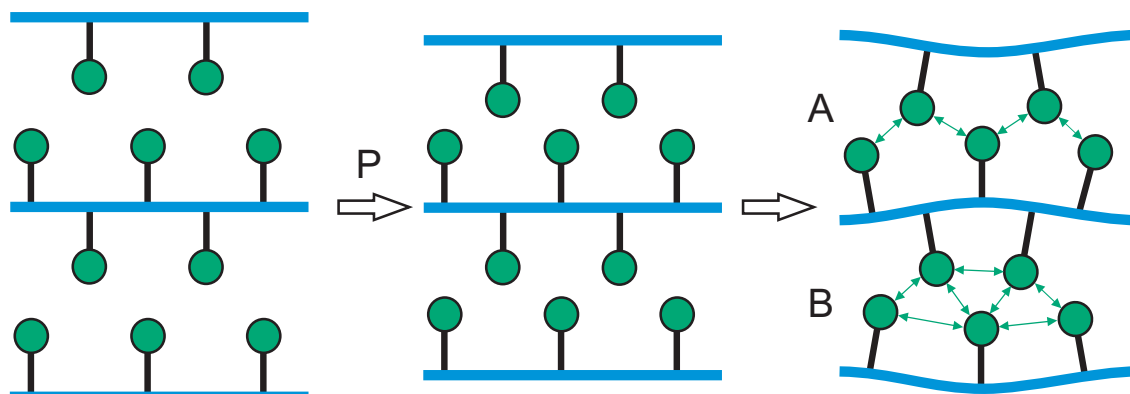
Figure 6.4:   Schematic representation of regions in the high-pressure phase of MOCl. Double arrows represent Cl$\cdots$Cl contacts that have achieved more favorable distances due to the modulation.

model, the slabs bulge towards each other (region **A** in Fig. 6.4), resulting in an increase of the gap between Cl atoms neighboring along **a**, thus allowing Cl atoms of neighboring slabs to interpenetrate (Fig. 6.1 b–d), resulting in a denser packing. In the second model, slabs bend inward (region **B** in Fig. 6.4), resulting in a reduction of the space between Cl atoms neighboring along **a**. However, interlayer Cl$\cdots$Cl distances become longer, thus allowing layers to close in, again resulting in a denser packing.

Because the M–O framework is covered by Cl atoms at both sides, the appearance of region **A** on one side will immediately lead to region **B** on the other side of the slab (Fig. 6.4). This results in doubling of the unit cell along the **c** axis which explains the rational component $\frac{1}{2}$ of the modulation wave vector. The accurate structure models reveal that the incommensurate crystal structures represent an antiphase buckling of adjacent slabs indeed (Fig. 6.1 b–d). This is represented by in-phase z-displacements of M, O and Cl atoms belonging to the same slab and possessing the same x-coordinates in the average structure (see t-plots in Fig. A.4, Appendix A). The structure models furthermore show that the major part of the modulation is given by displacements of Cl atoms in the direction of **a**. These displacements further the densification of CrOCl by allowing slabs to become closer to each other. The superspace symmetry of the incommensurate structure does not allow for atomic displacements along **b**. This is in agreement with the suggested mechanism of the phase transition, because the Cl$\cdots$Cl distances along **b** are much smaller than twice the Van der Waals radius of Cl atom, leaving no room for further decrease. Displacements of Cl atoms are severely restricted by the rigidity of the M–O and M–Cl bonds. They prevent a single most favorable Cl$\cdots$Cl distance

to be achieved for all Cl atoms, thus explaining the incommensurability and the modulations of varying wavelengths as a function of pressure.

The discovery of the incommensurate phase in CrOCl has triggered us to re-investigate the high-pressure phase diagram of FeOCl in the vicinity of 15 GPa. Indeed, incommensurate satellite reflections have now been found in the diffraction pattern of FeOCl at 15.0 GPa with $\mathbf{q} = (0.260, 0, \frac{1}{2})$, while the $\mathbf{q}$-vector is commensurate with $\sigma_1 = \frac{1}{4}$ at the next measured pressure of 22.7 GPa. The incommensurate phase of FeOCl exists in a range of pressures of at most a few GPa wide. Different radii of Fe^{3+} and Cr^{3+} lead to different M–O distances, and therefore to a different packing of Cl atoms, explaining the different periods of the modulations in FeOCl and CrOCl. Furthermore, the slightly lower transition pressure in FeOCl can be explained by the smaller cation size of Cr^{3+} than Fe^{3+}, which makes the CrOCl slabs more rigid. Therefore, more energy (higher pressure) is required to distort the Cr–O framework than to distort the Fe–O framework. Rigorous assessment of the impact of slight differences in ambient-pressure structures, different cation sizes and different electronic configurations on the observed differences between the $\mathbf{q}$-vectors and their pressure dependence would require additional experiments on isostructural compounds.

While the range of incommensurability of FeOCl is small, the intermediate structure of CrOCl persists up to 51 GPa. Compression from 16.4 to 30.3 GPa is accompanied by a gradual increase of modulation amplitudes. At 30.3 GPa the amplitudes saturate and further compression enhances the σ_1 component of the $\mathbf{q}$-vector. Apparently, the initial growth of modulation amplitudes is required to avoid shortening of interlayer $Cl \cdots Cl$ distances with diminishing of the interlayer spacing. An upper bound is reached, when unfavorably short intralayer $Cl \cdots Cl$ distances would occur. At higher pressures the evolution of the structure follows the expected behaviour of buckled slabs: increase of the σ_1 component of the $\mathbf{q}$-vector allows to reduce the $\mathbf{a}$-axis avoiding the energy-demanding large contraction of Cr–O distances.

At 57.2 GPa (highest pressure achieved) two commensurate phases are found to coexist in CrOCl. This indicates that two phase transitions take place between 51 and 57.2 GPa. One is a lock-in transition where σ_1 jumps to $\frac{1}{3}$ and a sixfold, $3a \times b \times 2c$ superstructure is formed. The second commensurate high-pressure phase is as threefold superstructure (see Appendix A). The transition is not accompanied by significant changes in molar volume. Therefore, no changes in connectivity (e.g. appearance of interlayer bonding) are expected. We could not obtain direct evidence of the exact sequence of phase transitions between 51 and 57.2 GPa. However, the smaller unit cell of the threefold superstructure may suggest that it is

developed at higher pressures than the sixfold superstructure of the lock-in phase. On decompression, the lock-in phase is preserved down to at least 47.5 GPa, with the commensurate-to-incommensurate transformation taking place between 47.5 and 40.5 GPa. These observations provide evidence for strong first-order character of the lock-in transition. Furthermore, it supports the idea the threefold superstructure is the stable phase at the highest pressures.

We have shown that high-pressure behavior of MOCl is governed by strongly non-bonded inter- and intralayer $Cl\cdots Cl$ contacts. In the vicinity of 15 GPa interlayer $Cl\cdots Cl$ contacts reach the strongly repulsive region of the interatomic potential at ~3 Å interatomic separation. This results in a phase transition towards an incommensurately modulated phase by which shorter $Cl\cdots Cl$ distances are avoided. MOCl are not molecular compounds, where generally there are more degrees of freedom regarding the variation of molecular arrangement. Nevertheless, there are voids within the structure, which allow Cl displacements along **a**. The rigid framework of M–O bonds, in turn, implies restrictions on the positions of Cl atoms. Therefore, a single most favorable configuration cannot be achieved. In CrOCl the high-pressure structure is incommensurate up to at least 51 GPa. Between 51 and 57 GPa a lock-in phase transition to a sixfold $3a \times b \times 2c$ superstructure takes place, while at still higher pressures a threefold superstructure is formed. Apparently, there is a tendency for the simplification of the structure towards higher pressures. The importance of non-bonded interactions described here for the high-pressure behavior of CrOCl will have implications for the understanding of high-pressure phase diagrams of other classes of inorganic materials, but it may also bear relevance for the stress properties of Van der Waals-bonded heterostructures [134].

Methods

Sample preparation. Single crystals of CrOCl were prepared by the gas transport technique using $CrCl_3$ (99.9 %, Alfa) and Cr_2O_3 (99.997 %, Alfa) as starting reagents, and using $HgCl_2$ as transport reagent [20]. Single crystals of FeOCl were prepared by gas transport from a stoichiometric mixture of $FeCl_3$ (99.99 %) and Fe_2O_3 (99.999 %) [10, 19]. The high-quality single crystals of CrOCl and FeOCl along with small ruby spheres were placed inside BX90 diamond anvil cells [60] equipped with Boehler-Almax diamonds (culet size 250 μm). Ne was used as a pressure-transmitting medium.

X-ray diffraction. Single-crystal X-ray diffraction experiments were performed at the beamlines ID09A (ESRF, Grenoble, France) and P02.2 (PetraIII, Hamburg, Gemany) using monochromatic X-ray radiation of wavelengths 0.414 and 0.290 Å

respectively. The diffraction data were collected in a sequence of 1° oscillations over a total scan range of 80° around the vertical (ω) axis. Diffracted intensities were collected with Mar555 flat panel and PerkinElmer XRD 1621 detectors.

Data analysis. Lattice parameters, components of the **q**-vector and integrated intensities were obtained from the measured images using the computer program $CrysAlis^{Pro}$. Bragg reflections overlapping with reflections from the diamonds or the pressure-transmitting medium were excluded from the data integration procedure. Outliers were removed (usually 1–2 per data set) according to procedures recently implemented in Jana2006 [75].

Crystal structures. Crystal structures were obtained within the superspace approach using the superspace group $Pmmn(\sigma_1, 0, \frac{1}{2})00s$. Structure refinements of the atomic coordinates and modulation amplitudes were performed with the software Jana2006[135]. They resulted in a good fit to the diffraction data at each pressure. Further details on structure models are given in the Appendix A.

Chapter 7

Pressure-induced phase transitions in MOCl (M = Ti, V, Sc)[1]

7.1   Introduction

The layered compound TiOCl has become one of the most intensively studied low-dimensional S $= \frac{1}{2}$ systems since the discovery of its unconventional spin-Peierls transition by Seidel et al. in 2003 [34]. On cooling, TiOCl undergoes a phase transition at $T_{c2} = 90$ K towards an incommensurately modulated phase, and a second transition at $T_{c1} = 67$ K towards a $a \times 2b \times c$ superstructure [36]. The transitions lead to the formation of Ti^{3+}–Ti^{3+} singlet dimers along the direction of quasi-one-dimensional spin chains (along the **b**-axis). For highly anisotropic systems, like TiOCl, the application of hydrostatic pressure provides a way of modifying magnetic intrachain and interchain exchange parameters, and allows to get a broader understanding of the interplay between different degrees of freedom in these systems.

The high-pressure behavior, and especially high-pressure crystal structures remain the biggest mysteries in TiOCl physics. TiOCl is a Mott insulator with weak electron localization attributed to high nearest-neighbor exchange coupling. Therefore, it was suggested that TiOCl is close to an insulator-metal transition and an application of pressure would be an ideal tool to trigger this transition [43]. First high-pressure transmittance and reflectance measurements suggested that TiOCl undergoes an insulator-to-metal transition at $\sim$12 GPa [43]. Later Forthaus et al. have performed electrical transport measurements [44] and found that TiOCl does not transform to a metallic state, although there is a substantial change in the pres-

---

sure dependence of the band gap width around 13 GPa. This indicated a change in the electronic structure of TiOCl. At the same time, no structural changes were observed by means of energy-dispersive powder X-ray diffraction. Later Zhang et al. [45] have performed *ab initio* calculations and claimed two pressure-induced phase transitions to occur. The first transition leads to the two-dimensional metallic state with strong Ti–Ti dimerization. The dimerization is suppressed at the second transition, and TiOCl becomes a uniform metal.

The structural evidence for the first transition has been obtained by Kuntscher et al. [46]. Employing powder X-ray diffraction they have found additional reflections on the diffraction pattern above 15.5 GPa. However, no structural model has been proposed for the high-pressure phase. Later Blanco-Canosa et al. [47, 48] proposed that the high-pressure structure is a monoclinic $a \times 2b \times c$ superstructure with symmetry $P2_1/m$. A Rietveld refinement revealed the formation of Ti–Ti dimers along the **b**-axis. Although the refinement results are supported by the theoretical calculations, the accuracy of Rietveld refinement of TiOCl powders is rather questionable. Indeed, later Ebad-Allah et al. [49] interpreted powder X-ray diffraction patterns of TiOCl in a different way. They suggested that above 15 GPa a mixture of ambient-pressure $Pmmn$ phase and a monoclinic $2a \times 2b \times c$ superstructure exists. Moreover, Ebad-Allah et al. have found a pronounced anomaly in all lattice parameters of the $2a \times 2b \times c$ superstructure and suggested that a second transition takes place at 22 GPa. However, no models were proposed for these high-pressure superstructures.

So, up to now no full agreement has been obtained about the possible metallization of TiOCl at high pressure. Furthermore, no accurate structure models are reported for high-pressure structures. A major reason is that it is not possible to produce good TiOCl powders for measurements in diamond anvil cells (DACs). Plate-like crystallites of TiOCl orient themselves to lie flat on the diamond culet, and, therefore, the crystallographic **c**-axis becomes parallel to the primary X-ray beam. Due to this extreme preferred orientation, Rietveld refinements can not provide reliable structure models. A straightforward solution is, therefore, a single-crystal X-ray diffraction experiment.

Novel developments in the instrumentation for high-pressure crystallography now make single-crystal X-ray diffraction measurements feasible even above 100 GPa [136]. Recently, several high-pressure single-crystal X-ray diffraction studies were performed on isostructural FeOCl and CrOCl compounds [126, 127]. It was shown that in the vicinity of 15 GPa these compounds undergo a pressure-induced phase transition related to the optimization of crystal packing rather than to any mag-

netic or electronic phenomena. Furthermore, it was claimed that similar distortions may contribute to the high-pressure behavior of TiOCl and other isostructural compounds (e.g. VOCl, ScOCl, InOCl). Here we report the results of single-crystal X-ray diffraction studies of TiOCl, VOCl and ScOCl. The results resolve a long-standing mystery of TiOCl and point out similarities and differences in MOCl (M = Sc, Ti, V, Cr, Fe) phase diagrams.

7.2   Experiment

High-pressure phase diagrams of ScOCl, TiOCl and VOCl were studied by means of single-crystal X-ray diffraction in diamond anvil cells using synchrotron radiation. Experimental details are summarized in the Table 7.1.

Table 7.1: Experimental details of high-pressure single-crystal X-ray diffraction studies of MOCl.

	ScOCl	TiOCl	VOCl
Beamline	P02.2 (DESY)	ID09A (ESRF)	ID09A (ESRF)
Wavelength, Å	0.28995	0.4127	0.4145
Detector	Pilatus 300K	MAR555	MAR555
Gasket material	Re	Re	Re
Pressure medium	Ne	Ne	Ne
Pressure sensor	Ruby	Sm:YAG	Ruby
Data collection type	ω-scans	ω-scans	ω-scans
$\Delta\omega,°$	0.5	1.0	0.5
ω range, °	$-40 \to 40$	$-40 \to 40$	$-40 \to 40$

Pressure was determined using a shift of $R1$ and $Y1$ fluorescence peaks of ruby and Sm:YAG respectively [63, 137]. Fluorescence of the pressure standard was measured before and after each data collection, and an average value was considered to be the pressure for the actual data set. Diffraction data were collected by narrow ω-scanning with $\Delta\omega = 0.5 - 1.0°$ and an exposure time of 1 s. At some pressure points the DAC was rotated by $90°$ degrees around the primary beam direction and a second run was performed, in order to increase data completeness. Data processing (peak intensities integration, background evaluation, lattice parameters, space group determination, frame scaling and absorption correction) was done with the $CrysAlis^{Pro}$ software (see Chapter 3). All structure refinements were performed with Jana2006 crystallographic computing system [135].

7.3 High-pressure crystal structures

TiOCl

Single-crystal X-ray diffraction data were collected for TiOCl at 7 pressure points. The ambient-pressure structure with orthorhombic symmetry $Pmmn$ was detected at $P = 0.2$ GPa and at $P = 3.7$ GPa. The structure was refined based on the model reported by Schäfer et al. [11]. Due to the limitations on data completeness imposed by the DAC technique, only the atomic displacement parameters of Cl were refined anisotropically.

At the next pressure point (9 GPa) additional weak reflections appeared on the diffraction pattern. They could be indexed with an incommensurate $\mathbf{q}$-vector $(\sigma_1, \sigma_2, 0)$, where $\sigma_1 = 0.1016$ and $\sigma_2 = 0.5109$. Based on the diffraction symmetry and on the analysis of systematic absences the superspace group was found to be $P2/n(\sigma_1, \sigma_2, 0)0s$ (with standard setting $P2/b(\sigma_1, \sigma_2, 0)00$, No. 13.1.2.1) [93]. We denote this phase of TiOCl as TiOCl–II.

The crystal structure in superspace is defined by the coordinates of the atoms in the basic structure and their displacements. So, the position ($\mathbf{x}$) of the atom μ can be obtained as a sum of its position in the basic structure ($\bar{\mathbf{x}}(\mu)$) and the value of the modulation function $\mathbf{u}^\mu$. Since only first-order satellite reflections were observed, the modulation was described by first-order harmonic functions:

$$u_i^\mu(\bar{x}_4) = A_i(\mu)\sin(2\pi\bar{x}_4) + B_i(\mu)\cos(2\pi\bar{x}_4), \qquad (7.1)$$

where $i = x, y, z$, $\bar{x}_4 = t + \mathbf{q} \cdot \bar{\mathbf{x}}(\mu)$, t is the phase of the modulation, and A_i and B_i are the amplitudes of the modulation functions. Due to the symmetry restrictions on the atomic modulation functions coefficients A_x, A_y and B_z are equal to 0 for each atom.

The average structure was derived using group-subgroup relations between $Pmmn$ and $P2/n$ space groups [138]. Modulation amplitudes were refined starting from small arbitrary values (< 0.01 Å). The same structure was observed for the next pressure point (11.2 GPa), however, the σ_2 component of the $\mathbf{q}$-vector appeared to be pressure-dependent (see Table B.3 in Appendix B). All refinements smoothly converged to excellent fits to the diffraction data.

Two kinds of satellite reflections were found on the diffraction pattern above 15 GPa. Some satellites were indexed with $\mathbf{q}^1 = (\sigma_{11}, \frac{1}{2}, 0)$ as valid for TiOCl-II, but with a rational component along $\mathbf{b}^*$. Additional satellites were indexed with $\mathbf{q}^2 = (\sigma_{21}, 0, \frac{1}{2})$. These $\mathbf{q}^2$ satellites are extremely weak at 15 GPa, however their intensities rapidly increase with pressure: $<\frac{I}{\sigma(I)}>_{main}/<\frac{I}{\sigma(I)}>_{q^1}/<\frac{I}{\sigma(I)}>_{q^2} =$

10.88/2.81/1.86 at 15.0 GPa and 11.35/2.83/4.06 at 18.1 GPa. No mixed satellites were observed at positions $\pm\mathbf{q}^1 \pm \mathbf{q}^2$ at 15 GPa, and only 5 such reflections were observed at 18.1 GPa.

At 18.1 GPa $\sigma_{11} = 0.1179$ and $\sigma_{21} = 0.2364$. These values are far from any rational number with fairly low denominator (more or less acceptable rational approximations are $\frac{2}{17} = 0.1176$ and $\frac{4}{17} = 0.2353$). Therefore, the structure of TiOCl has been considered as incommensurately modulated at this pressure point.

In case of two $\mathbf{q}$-vectors, the general formula for the modulation functions has the following form:

$$u_i^{\mu}(\bar{x}_4, \bar{x}_5) = \sum_{n_1=0}^{\infty} \sum_{n_2=0}^{\infty} A_i^{n_1 n_2}(\mu) \sin[2\pi(n_1\bar{x}_4 + n_2\bar{x}_5)] + B_i^{n_1 n_2}(\mu) \cos[2\pi(n_1\bar{x}_4 + n_2\bar{x}_5)],$$

(7.2)

where $\bar{x}_4 = t_1 + \mathbf{q}^1 \cdot \bar{\mathbf{x}}$, $\bar{x}_5 = t_2 + \mathbf{q}^2 \cdot \bar{\mathbf{x}}$, $i = x, y, z$, and the term with $n_1 = n_2 = 0$ is excluded from the summation [52]. The maximum values of n_1 and n_2 for the refinement were defined by the maximal order of corresponding satellite reflections, which were observed in the diffraction pattern. At 18.1 GPa $n_{1max} = 1$ and $n_{2max} = 3$. Due to the absence of mixed satellites, all terms in which both n_1 and n_2 are non-zero are excluded from the summation 7.2. The best fit to the diffraction data was achieved using the superspace group $P2/n(\sigma_{11}, \sigma_{12}, 0)0s(\sigma_{21}, \sigma_{22}, \frac{1}{2})0s$ with $\sigma_{12} = \frac{1}{2}$ and $\sigma_{22} = 0$ (Table B.3 in Appendix B).

At 15 GPa $\sigma_{11} = 0.1242 \approx \frac{1}{8}$ and $\sigma_{21} = 0.2494 \approx \frac{1}{4}$, indicating the structure at this pressure point may be a commensurate $8a \times 2b \times 2c$ superstructure. However, due to the weakness of $\mathbf{q}^2$ satellites and the absence of satellite reflections of higher order, an unambiguous distinction between commensurate and incommensurate models was not possible. At the same time, in case of large superstructures, treatment of the superstructure as incommensurate may serve as a good approximation to the real structure, and a crystal-chemical analysis does not suffer much from this ambiguity (see Chapter 4). Therefore, the 15 GPa crystal structure has been treated as incommensurately modulated. For the structure refinement, the structure model of TiOCl at 18 GPa (Table B.4 in Appendix B) has been taken with modulated functions truncated to the first order harmonics. TiOCl phase observed at 15 and 18.1 GPa is denoted as TiOCl-III.

Above 20 GPa, the crystal quality started to decrease rapidly, therefore at higher pressures only indexing of the diffraction pattern was possible. At 25 GPa the reciprocal lattice of the basic structure still could be identified. Reconstructed (hkl) planes with integer k index contain strong satellite reflections which could be indexed with $\mathbf{q} = (\frac{1}{5}, 0, \frac{1}{2})$. In addition, weaker reflections could be found within $(h\ k+0.5\ l)$
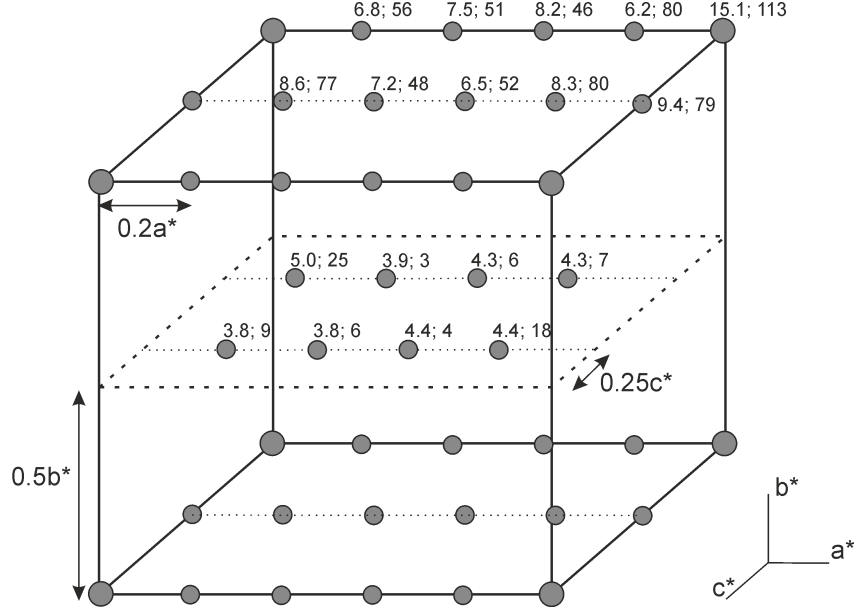
Figure 7.1: A scheme of the reciprocal lattice of TiOCl-IV. Main reflections are represented by large grey circles, and superlattice reflections are represented by small circles. Lengths relations between reciprocal lattice parameters are not maintained for picture simplicity. Average $I/\sigma(I)$ values for reflections with $I > 3\sigma(I)$ and the total number of such reflections are given in a form $< I/\sigma(I) >; N$.

planes at positions $h \pm \frac{1}{5}n, k + \frac{1}{2}, l \pm \frac{1}{4}$, where $n = 1, 2$ (Fig. 7.1). In fact, all reflections can be indexed with a single $\mathbf{q}$-vector. However, the choice is not unique. Each $\mathbf{q}$-vector $(\frac{i}{5}, \frac{j}{2}, \frac{k}{4})$, where $i \neq 5n, j = 2n + 1, k = 2n + 1$, can describe the diffraction pattern. A convenient choice would be to choose the $\mathbf{q}$-vector in a way that lower-order satellites are more intense, than the higher-order ones. According to the data presented in the Fig. 7.1, the best option is $\mathbf{q} = (\frac{1}{5}, \frac{1}{2}, \frac{1}{4})$. This phase is denoted further as TiOCl-IV. Above 25 GPa the crystal was completely destroyed.

VOCl

Single-crystal X-ray diffraction of VOCl was performed at 12 pressure points on compression from ambient pressure up to 50.5 GPa, and at 7 pressure points on decompression. The ambient-pressure crystal structure of VOCl is stable up to 14.1 GPa. The structure was refined based on the model reported by Haase et al. [139].

Between 14.1 and 16.3 GPa VOCl undergoes a normal-to-incommensurate phase transition similar to that found in FeOCl and in CrOCl (Chapters 4, 5, 6). Satellite reflections can be indexed with $\mathbf{q} = (\sigma_1, 0, \frac{1}{2})$, where σ_1 amounts to 0.26. The structure model from incommensurate structure of FeOCl with superspace group

symmetry $Pmmn(\sigma_1, 0, \frac{1}{2})00s$ was taken as a starting model for the refinement of the high-pressure structure of VOCl. Atomic modulation functions of each atom were described as Fourier series truncated to third order:

$$u_i^\mu(\bar{x}_4) = \sum_{n=1}^{3} A_i^n(\mu) \sin(2\pi n \bar{x}_4) + B_i^n(\mu) \cos(2\pi n \bar{x}_4). \qquad (7.3)$$

This incommensurate phase is denoted as VOCl-II.

Further compression leads to the formation of a $3a \times 3b \times 2c$ superstructure above 20 GPa. In order to describe all superlattice reflections of a $3a \times 3b \times 2c$ superstructure, at least two **q**-vectors are needed. This makes the superspace analysis rather complex. Furthermore, all possible types of superlattice reflections have been observed, and some of them appeared to be of comparable intensities with the main reflections. Hence, the gain in the number of refined parameters for the superspace description of the superstructure will not be substantial. Therefore, in the current case a conventional refinement may be a better choice for the structure description.

The superstructure has a monoclinic symmetry $P2_1/c$ (**a** - axis unique), and the crystal is twinned by pseudomerohedry. All structure refinements at pressures below 38 GPa (including points on decompression) lead to good fits to the data (Table B.5 in Appendix B). However, attempts to refine crystal structure using the same $P2_1/c$ model at pressures above 38 GPa lead to R-factors higher than 0.1, to non-positive definite atomic displacement tensors and to many correlations between refined parameters. Analysis of the diffraction pattern revealed that additional systematic absences appear and correspond to an n-glide perpendicular to the **c**-axis (Fig. 7.2). A successful structure solution and refinement has been performed using the orthorhombic space group $Pcmn$ (Table B.5 in Appendix B). Therefore there is one more transition in VOCl between 35.4 and 38.0 GPa. The monoclinic $P2_1/c$ and orthorhombic $Pcmn$ structures are denoted as VOCl-III and VOCl-IV respectively.

All phase transitions in VOCl appeared to be reversible. Decompression leads to the transformation towards ambient-pressure $Pmmn$ structure. Reduction of the crystal quality is responsible for slightly higher R-values for structure refinements on decompression (Table B.5 in Appendix B).

ScOCl

Weak scattering power of a thin ScOCl crystal ($d \sim 1\mu$m) together with the low sensitivity of a Pilatus300K detector to the high-energy radiation did not allow to obtain a sufficient number of reflections for the structure refinements. Nevertheless,
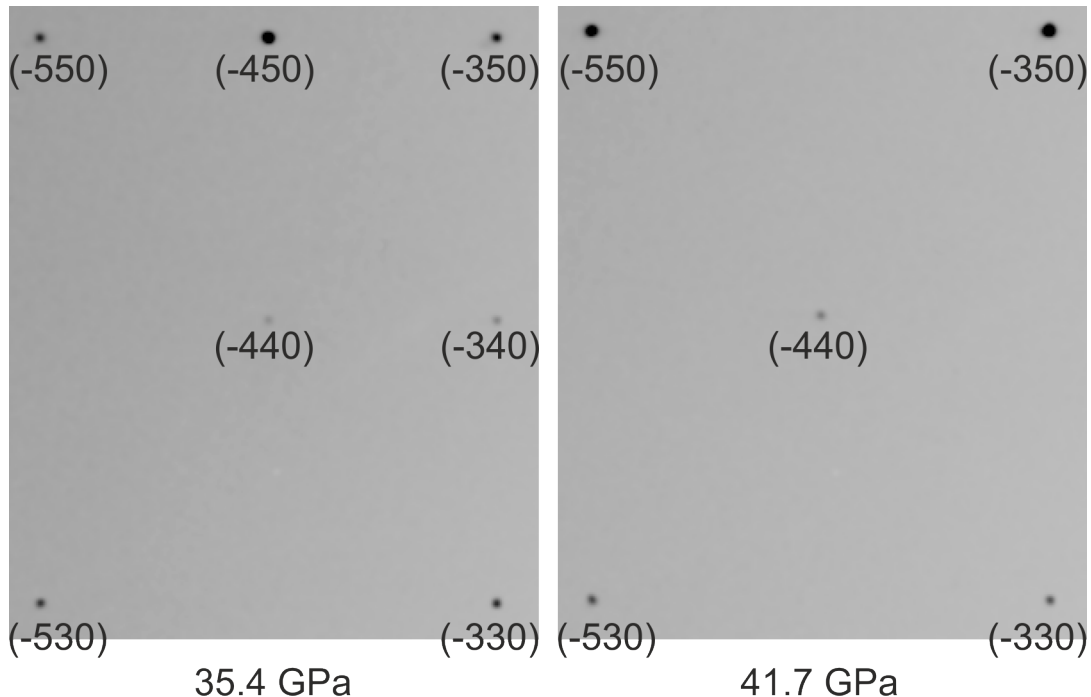
Figure 7.2: Reconstructed ($hk0$) planes of VOCl at 35.4 and 41.7 GPa.

the appearance of satellite reflections and a monoclinic lattice distortion revealed a structural phase transition between 4.8 and 8.4 GPa. The lattice parameters at 8.4 GPa were obtained as: $a = 3.821(5), b = 3.481(3), c = 6.92(3)$ Å, $\beta = 104.5°, \mathbf{q} = (\frac{1}{6}, 0, \frac{1}{2})$. Due to the pronounced monoclinic angle β, the superspace group $Pmmn(\sigma_1, 0, \frac{1}{2})00s$ does not apply to this structure.

7.4 Results and discussion

TiOCl

The first high-pressure phase of TiOCl (TiOCl-II) appears to be incommensurately modulated. Its structure is similar to the low-temperature incommensurate phase between $T_{c1} = 67$ K and $T_{c2} = 90$ K [37] (see Appendix B). Fausti et al. [109] have pointed out that the transition temperatures are correlated with the ratio between intrachain and interchain exchange interactions J_1 and J_2. The intrachain interaction arises from the direct exchange between Ti^{3+} ions, while the interchain interaction is of superexchange nature through oxygen atoms [109, 140]. General compressional trends in MOCl compounds, and in particular in TiOCl show that intrachain Ti–Ti distances are much more affected by applied pressure than Ti–O

distances and Ti–O–Ti angles along $\mathbf{a} + \mathbf{b}$. Therefore, J_1 strongly increases with pressure, while J_2 is much less pressure-dependent. Such anisotropic behavior leads to a strong enhancement of the transition temperatures.

None of the previous high-pressure diffraction studies of TiOCl has reported an incommensurate phase [44, 47–49]. However, Ebad-Allah et al. have reported the appearance of additional reflections in the powder diffraction diagrams above ∼7 GPa [49]. The diffraction has been interpreted assuming the coexistence of several high-pressure phases. Nevertheless, taking in account our single-crystal studies, we can conclude that Ebad-Allah et al. have indeed observed TiOCl-II, but unambiguous indexing of their powder diffraction patterns was not achieved. Using the results of Ebad-Allah et al. we can, therefore, establish a precise transition pressure of 7 GPa for the TiOCl-I $\rightarrow$ TiOCl-II transition. This transition pressure is in a good agreement with the pressure dependence of T_{c2} reported by Blanco-Canosa et al. [48]. According to magnetic susceptibility measurements up to ∼1 GPa, $\frac{dT_{c2}}{dP} = 33.2 \ \frac{K}{GPa}$. Therefore, the incommensurate phase can be expected to appear at ambient temperature at ∼ 6 GPa. The major structural distortion in TiOCl-II is expressed in a variation of Ti–Ti distances along the $\mathbf{b}$-axis. The modulation amplitude $B_y[\text{Ti}]$ is ∼3 times larger than at low temperatures and increases with pressure (Table B.2 in Appendix B).

Further increase of pressure may lead to two phenomena. First of all, reported $\frac{dT_{c1}}{dP}$ amounts to 19.1 $\frac{K}{GPa}$ [48]. Therefore, a lock-in transition to a $a \times 2b \times c$ superstructure may be expected around 12 GPa. Secondly, a structural transition, related to the optimization of packing of Cl atoms, typical for MOCl compounds can be expected close to ∼ 15 GPa [126, 127].

Our single-crystal X-ray diffraction experiments show that both distortions contribute to the high-pressure crystal structure of TiOCl. Two modulation wave vectors are needed to describe the diffraction pattern of TiOCl above 15 GPa. The first one ($\mathbf{q}^1 = (\sigma_{11}, \frac{1}{2}, 0)$) arises from spin-Peierls-like distortions (pairing of Ti atoms in dimers along the $\mathbf{b}$ - axis). The second ($\mathbf{q}^2 = (\sigma_{21}, 0, \frac{1}{2})$) arises from the buckling of Ti–O layers and optimization of packing of Cl atoms.

So far, in literature, there is one single-crystal X-ray diffraction study of TiOCl at high pressure [98]. The experiment has been performed at $T = 6$ K. Remarkably, the authors found incommensurate satellite reflections at positions (1.52, 0, 0) and (2.48,0,0) at $P = 13.2$ GPa and $T = 6$ K [98]. The positions of these satellites are in good agreement with positions of second-order $\mathbf{q}^2$-type satellites in TiOCl-III. In view of an absence of electronic and magnetic contributions to the $\mathbf{q}_2$-type distortion, it is not expected to be much temperature-dependent. Therefore, it is

likely that Prodi et al. [98] have observed at 6 K similar $\mathbf{q}^2$-type distortions as in TiOCl-III at ambient temperature.

The structure of TiOCl-III is presented in Fig. 7.3. Each Ti chain is dimerized, so there are two Ti–Ti distances along each chain, but these distances vary from chain to chain along the direction $\mathbf{a}$. This way of chain distortion is essentially different from that in TiOCl-II or in the incommensurate low-temperature phase, where all Ti chains possess equivalent modulations. It is reminiscent of that in $TiPO_4$ [141] (Chapter 8). This distortion type (however without incommensurate component along $\mathbf{a}$) was predicted and studied before [45, 47]. However, one can notice a buckling of Ti–O double layers like in CrOCl and in FeOCl [126, 127]. Therefore, two inherently different distortions contribute to the high-pressure crystal structure of TiOCl-III. The $\mathbf{q}^2$ distortion has never been taken into account in previous studies of TiOCl. The $\mathbf{q}^2$ distortion is unlikely a reason for substantial changes in electronic or magnetic structure of TiOCl [126, 127]. It has no effect on Ti–Ti distances along the direct exchange path (along $\mathbf{b}$) and only slightly affects Ti–O, Ti–Cl and interchain Ti–Ti distances. It should be noted that despite the fact that $\mathbf{q}^1$- and $\mathbf{q}^2$-type distortions are related to entirely different phenomena, the incommensurate components of the $\mathbf{q}$-vectors seem to be coupled. So, at both pressure points, at which TiOCl-III phase has been observed, $\sigma_{21} \approx 2\sigma_{11}$.

Blanco-Canosa et al. [47] suggested that the spin-Peierls distortion is expected to be supported by a conventional Peierls distortion since the short Ti–Ti distance approaches the limit for electron itinerancy. Piñeiro et al. [142] suggest that on increasing pressure two dimerized high-pressure phases develop: so-called short-dimerized and long-dimerized structures. The short-dimerized phase corresponds to a conventional spin-Peierls scenario with small alternation of Ti–Ti distances along the chains. The long-dimerized phase with strong variations in Ti–Ti distances occurs due to a spin-Peierls $\rightarrow$ Peierls crossover. Table 7.2 contains intrachain Ti–Ti distances in TiOCl at different conditions. Our results show no significant enhancement of modulation amplitudes of Ti atoms from 10 GPa up to 18 GPa, but they are significantly larger than at low temperatures. Therefore, spin-Peierls-Peierls crossover is unlikely to occur at ambient temperature. Of particular interest would be to study high-pressure behavior of TiOCl at low temperatures.

Intensities of $\mathbf{q}^1$ satellites are comparable with those of $\mathbf{q}^2$ satellites in TiOCl-III, while in TiOCl-IV, satellites having half-integer component along $\mathbf{b}^*$ have negligible intensities (Fig. 7.1). This points that spin-Peierls-like dimerization is almost suppressed in TiOCl-IV, and the contribution of $\mathbf{q}^2$-type distortion increases. The suppression of dimerization is in agreement with the prediction of Zhang et al. [45].
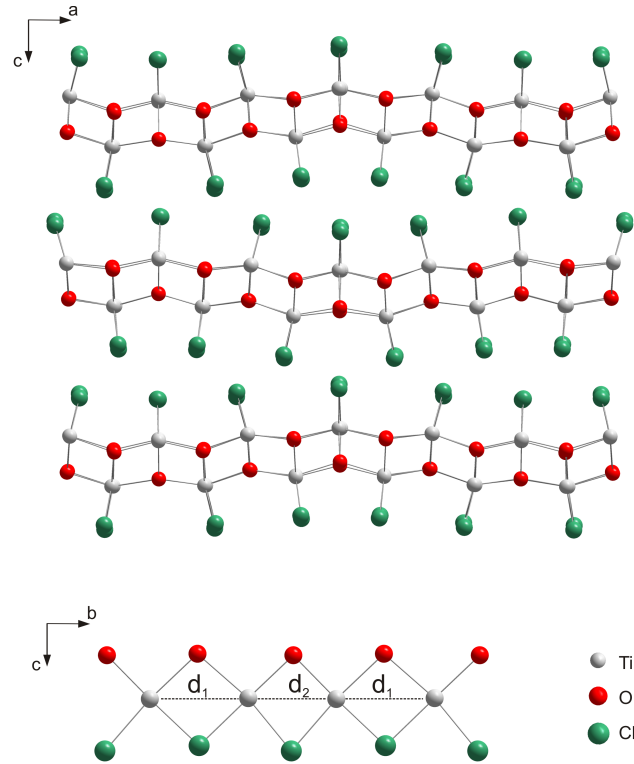
Figure 7.3: Incommensurate crystal structure of TiOCl at 18.1 GPa represented as a fragment of $17a \times 2b \times 2c$ basic-structure unit cells (upper figure). A projection of a single TiOCl chain along the **a**-axis with alternating Ti–Ti distances d_1 and d_2.

However, at the highest pressure point achieved in this study (25 GPa) the dimerization is not fully suppressed. This is revealed by a rational component of the **q**-vector along the **b**-axis $\sigma_2 = \frac{1}{2}$. A complete transformation to a non-dimerized metallic state can be, therefore, expected at higher pressures.

VOCl

High-pressure behavior of VOCl below 17 GPa didn't reveal any peculiarities in comparison with other MOCl compounds. Between 14.1 and 16.3 it undergoes normal-incommensurate phase transition typical for MOCl in this pressure range. However, further compression leads to a unique kind of structure. First, at 23.7 GPa a $3a \times 3b \times 2c$ superstructure was detected. This is not a typical lock-in phase, as observed in FeOCl and CrOCl, since it has a tripled **b**-axis. Another peculiarity is that the transition is accompanied by a volume drop of $\sim 7\%$, that was not observed in other MOCl compounds. Above the transition pressure, the compressibility of VOCl drastically decreases, which is represented by a change of the

Table 7.2: Intrachain Ti–Ti distances (Å) in TiOCl at different pressures and temperatures. Given are the average (d_{ave}), minimal (d_{min}), maximal (d_{max}) values and difference (Δ) between d_{max} and d_{min}.

Conditions	d_{ave}	d_{min}	d_{max}	Δ
0.0001 GPa, 10 K[1]	3.3145	3.254(1)	3.429(1)	0.175
0.0001 GPa, 72 K[2]	3.3417(10)	3.243(2)	3.438(2)	0.195
10.2 GPa, 293 K	3.1848(1)	2.9579(19)	3.4090(19)	0.451
11.8 GPa, 293 K	3.1604(10)	2.8965(19)	3.4187(19)	0.522
15.2 GPa, 293 K[3]	3.2	2.85(5)	3.55(5)	0.70
15.0 GPa, 293 K	3.134(6)	2.852(10)	3.395(8)	0.543
18.2 GPa, 293 K	3.117(12)	2.829(17)	3.385(17)	0.556

[1] Data from Shaz et al. [36].
[2] Data from Schönleber et al. [37].
[3] Data from Blanco-Canosa et al. [47].

slope of volume-pressure behavior (Fig. 7.4). An analysis of pressure behaviors of the lattice parameters shows that the volume drop is mostly related to the substantial reduction of the **b**-axis, and the change in compressibility defined by the identical change in the linear compressibility along the **c**-axis (Fig. 7.5).

The change in compressibility of the **c**-axis is explained by the appearance of interlayer V–Cl bonds (Fig. 7.6). So, V atoms located at positions of minimal interlayer distances change coordination from distorted octahedral to distorted face capped octahedral. For instance, at 23.7 GPa for three V atoms in such coordination, the V–Cl distances are: (2.372, 2.385, 2.402 Å); (2.310, 2.322, 2.573 Å) and (2.329, 2.386, 2.453 Å). Such behavior towards increasing of coordination numbers is in agreement with general expectations about high-pressure trends in crystal structures. The locking-in of the structure along **a** and doubling of the **c**-axis is similar to the behavior of CrOCl, which forms a lock-in $3a \times b \times 2c$ superstructure above 51 GPa. Substantial reduction of b is definitely not favorable for the packing of Cl atoms, therefore another mechanism is responsible for this transition. The triplication of the **b**-axis leads to three alternating V–V distances along this direction (Fig. 7.6 c). Some V–V distances along **b** approach the contact distance in V metal, suggesting the formation of V–V bonds. Taking into account the neighboring chains we found that each of the V atoms forming dimers along **b** is also connected to V atoms belonging to the neighboring chain (along **a** + **b**). Therefore triangular V clusters are formed in VOCl-III (Fig. 7.6 b). Formation of molecular clusters in
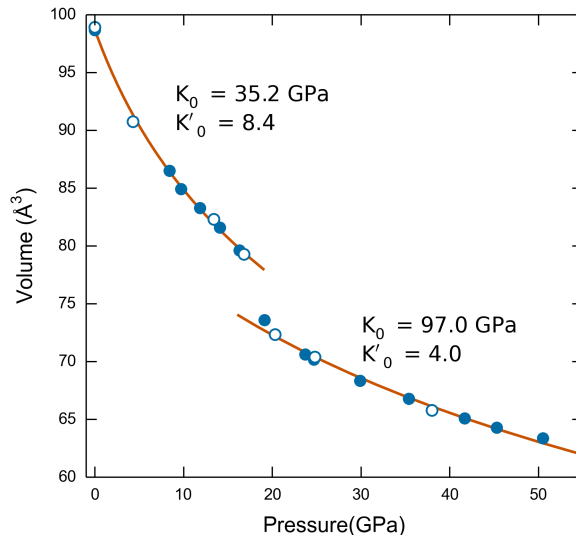
Figure 7.4:   Pressure dependence of the unit-cell volume of VOCl. Open symbols correspond to decompression experiment. For pressures above 20 GPa symbols represent unit-cell volume divided by 18.

Mott insulators usually is referred to as partial Mott transition: so in some parts of the systems, the interatomic distances are smaller than the critical distance for electron delocalization, but the distance between the clusters remains large, so there is no net metallic conductivity [143]. Other examples include trimer clusters in $LiVO_2$ [144], helical dimers in $MgTi_2O_4$ [145] and octamers in $CuIr_2S_4$ [146].

VOCl-III contains not only clusters of V atoms. One third of the V chains along the **b**-axis are only slightly distorted, and these chains do not contain V–V bonds (Fig. 7.6 b). Pressure-dependence of the intrachain V–V distances is shown in the Fig. 7.7. Above 20 GPa there are two distinct sets of V–V distances: shorter ones correspond to the V triangular clusters and longer ones - to the intertrimer distances, and to the V–V distances along the slightly distorted chains. Interestingly, the non-clustered V atoms are involved in the interlayer bonding through Cl atoms.

There are no distinct changes in the unit-cell volume and interatomic distances between orthorhombic VOCl-IV and monoclinic VOCl-III. The transition doesn't lead to formation of new clusters or V–V bonds. Overall, the structure becomes more symmetric: triangular V clusters become isosceles and overall number of distinct V–V distances decreases.
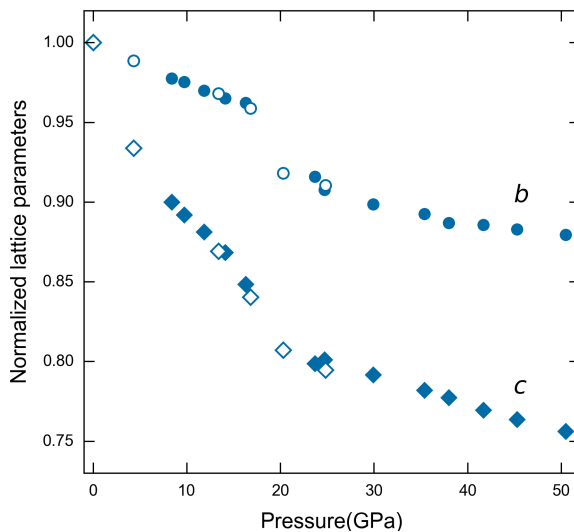
Figure 7.5: Pressure dependence of the normalized lattice parameters b and c of VOCl. Open symbols correspond to decompression experiment. For pressures above 20 GPa given are values of $b/3$ and $c/2$.

Relations between high-pressure behaviors of MOCl

MOCl exhibit both similarities and differences in their high-pressure behaviors. All MOCl undergo similar structural phase transitions which are revealed by the appearance of satellite reflections. The satellites could be indexed by a modulation wave vector $(\sigma_1, 0, \frac{1}{2})$. For TiOCl, VOCl, CrOCl and FeOCl the structural transition leads to the formation of incommensurately modulated structures (expressed by irrational values of σ_1). At higher pressures lock-in transitions take place (Table 7.3, Fig. 7.8).

The mechanism of the normal-incommensurate phase transitions in MOCl in the vicinity of 15 GPa was discussed in detail in the Chapter 6. Based on the analysis of crystal structures of CrOCl and FeOCl it was proposed that the transition takes place when interlayer $Cl \cdots Cl$ distances reach a limit of about 3 Å. Further decrease of interlayer distance does cost too much energy, and the gain in energy arising from the redistribution of Cl atoms compensate the elastic energy costs for the distortion of M–O layers. Apparently, this 3 Å rule is valid for VOCl and TiOCl as well. Interlayer $Cl \cdots Cl$ distances in VOCl at 14.1 GPa and in TiOCl at 12 GPa are 3.059Å and 3.131 Å respectively.

Nevertheless, the structural phase transition in ScOCl has been observed at
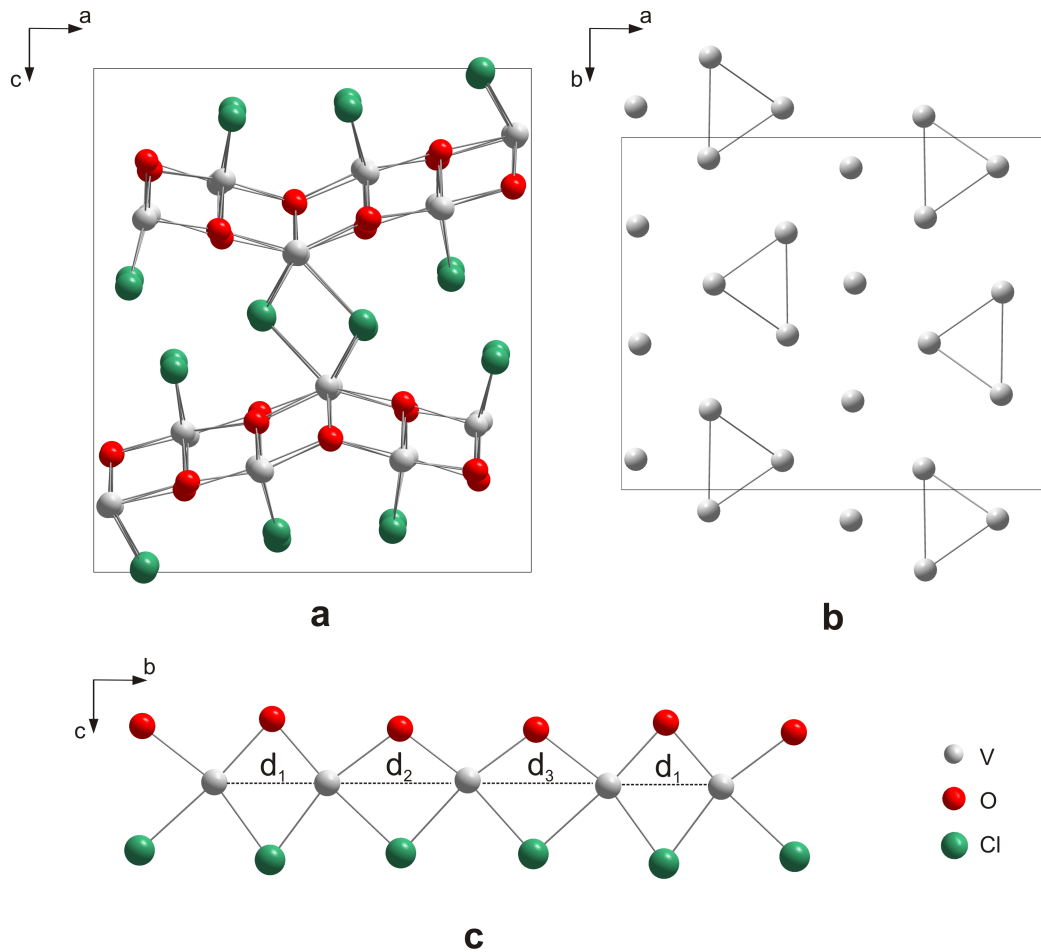
Figure 7.6: Projections of crystal structure of VOCl-III at 24.8 GPa (a) along the **b**-axis, (b) along the **c**-axis (only V atoms are shown) and (c) along the **a**-axis.

much lower pressures. Although, an incommensurately modulated phase of ScOCl has not been detected and structure solution of the $6a \times b \times 2c$ superstructure was not successful, a similar form of the modulation wave vector suggests that the distortion mechanism will be the same as in other MOCl. The interlayer Cl$\cdots$Cl distances do not depend much on the transition metal atom, but are defined only by the applied pressure. Therefore, the critical Cl$\cdots$Cl distance for ScOCl is larger than the value of 3 Å, common for other MOCl. This means that the critical Cl$\cdots$Cl distance may depend on the rigidity of the M–O slab. As a consequence the critical distance, and, therefore, the transition pressure will depend on the radius of M^{3+} (Fig. 7.9). Radii of Ti^{3+}, V^{3+}, Cr^{3+} and Fe^{3+} are more or less close to each other, and, consequently, M–O slabs stiffnesses, are close to each other. Sc^{3+}, however, has a much larger radius, much longer Sc–O distances, and much lower transition pressure.

It has been discussed in Chapters 5 and 6 that the normal-incommensurate
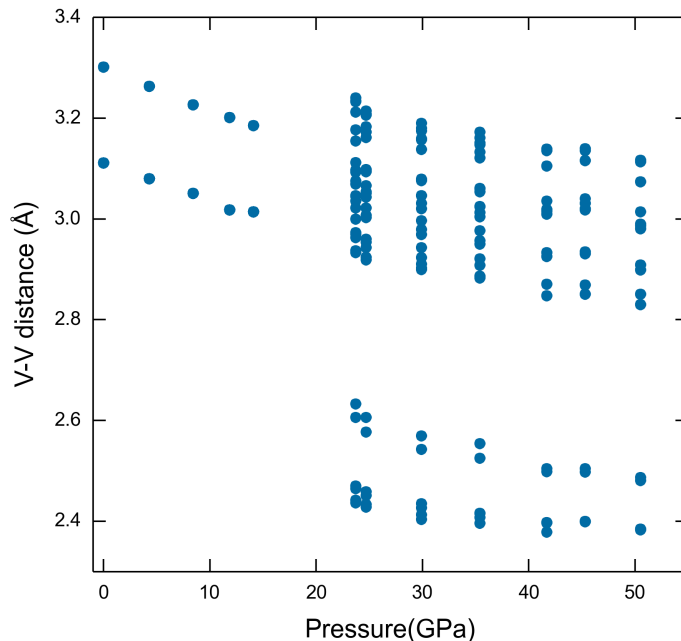
Figure 7.7: Pressure dependence of V–V distances.

transition is not related to changes in electronic or magnetic structures of MOCl. Therefore, it occurs in each MOCl compound independent of the number of its d-electrons, dimensionality of magnetic interactions or the width of the band gap. However these differences are responsible for different behaviors of MOCl apart from the structural transition. The most prominent example is TiOCl with only one d-electron on Ti^{3+}. This makes TiOCl a 1D magnetic system, unlike other compounds VOCl, CrOCl and FeOCl. So, a spin-Peierls distortion, driven by low-dimensional magnetism of TiOCl, occurs independently of the structural transition.

According to Goodenough [40], a critical internuclear separation R_c exists, for which the electrons may be considered as localized if the interatomic separation $R > R_c$. If $R < R_c$ it may lead to a metallic state. Among considered transition metals Cr^{3+} has the smallest R_c, and therefore, CrOCl is further from itinerant electron limit, and no metallization (CrOCl remains optically transparent) or distortions along the $\mathbf{b}$-axis were observed. VOCl is much closer to the formation of V–V homopolar bonds, and it happens above 20 GPa. Till now FeOCl has been studied up to $\sim$ 24 GPa by single-crystal X-ray diffraction and up to $\sim$34 GPa by powder X-ray diffraction, and no further transitions have been observed (Chapter 5). Nevertheless, a Mott transition may be expected not far from 34 GPa, since Fe^{3+}–Fe^{3+} distance is approaching its critical value. Complete understanding of the
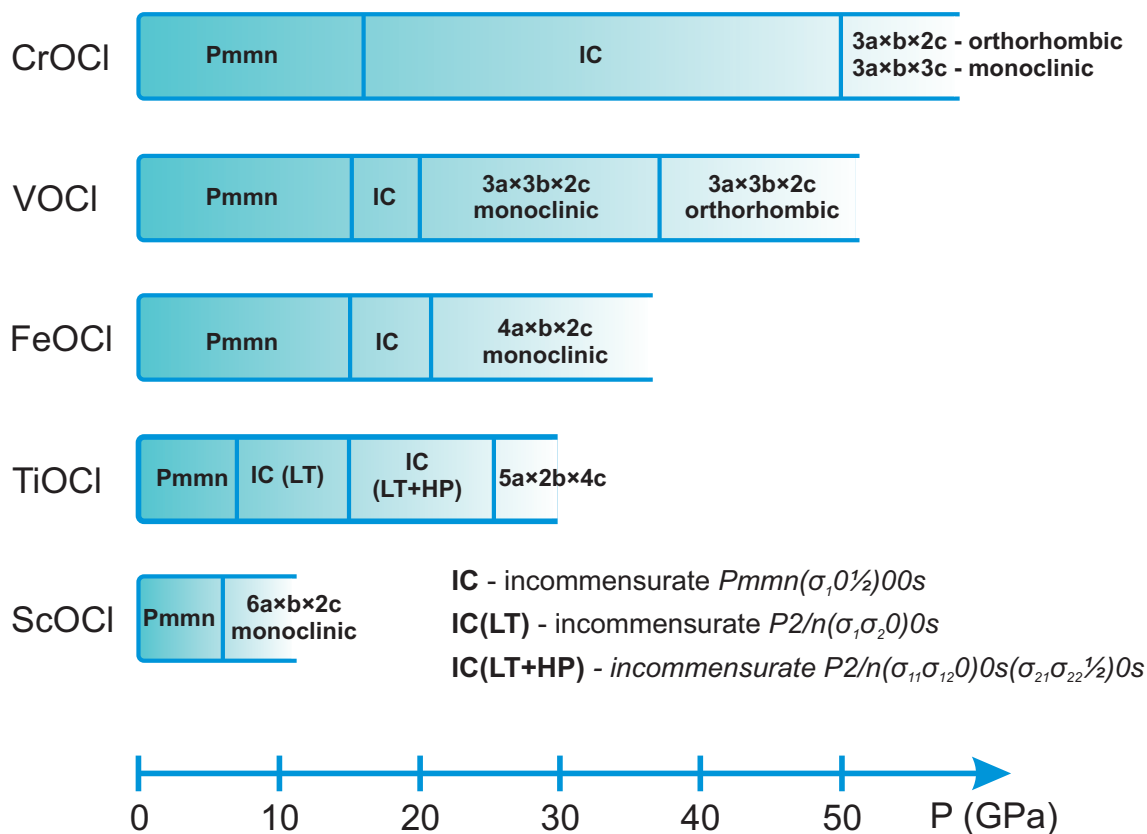
Figure 7.8: Scheme of pressure-induced phase transitions in MOCl.
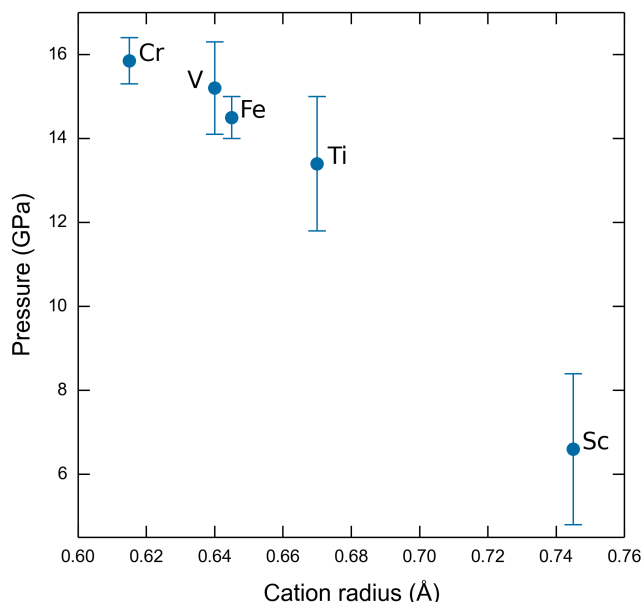
Figure 7.9: Phase transition pressures plotted against transition metal cation radius. Error bars show the pressure range within which, the transition takes place. The errors come from discrete set of pressure points.

94

Table 7.3: Pressures of normal-to-incommensurate (P_{c1}) and incommensurate-commensurate (P_{c2}) phase transitions in MOCl, values of σ components of the modulation wave vectors $\mathbf{q} = (\sigma, 0, \frac{1}{2})$.

	ScOCl	TiOCl	VOCl	CrOCl	FeOCl
P_{c1} (GPa)	unknown	13.4 ± 1.6	15.2 ± 1.1	15.85 ± 0.85	14.5 ± 0.5
σ at P_{c1}	unknown	0.2494	0.2618	0.2869	0.261
P_{c2} (GPa)	6.6 ± 1.8[1]	21.05 ± 2.95	18.3 ± 2.0	53.5 ± 2.5	18.85 ± 3.85
σ at P_{c2}	$\frac{1}{6}$	$\frac{1}{5}$	$\frac{1}{3}$	$\frac{1}{3}$	$\frac{1}{4}$

[1] P_{c2} for ScOCl is a pressure of incommensurate-commensurate phase transition under an assumption that the incommensurate phase was missed in our experiment.

high-pressure behaviors of MOCl requires theoretical calculations. Of particular interest would be to find a role of orbital order/degeneracy of M^{3+} d-orbitals in the stabilization of particular high-pressure structures. Furthermore, new experiments on ScOCl and on InOCl will give detailed information on normal-incommensurate-commensurate phase transitions and on the evolution of the lock-in phase without possible contribution from any electronic or magnetic phenomena.

7.5 Conclusions

We have investigated the high-pressure behaviors of TiOCl, VOCl and ScOCl by means of single-crystal X-ray diffraction. A common distortion related to the optimization of packing of Cl atoms is found in each MOCl (M = Sc, Ti, V) compound. The transition pressures depend on the radius of the transition metal atom, which in turn defines the stiffness of the M–O slab. Apart from that, the high-pressure behavior of MOCl is correlated with the electronic configuration of the transition metal atom. Spin-Peierls-like distortions have been found in quasi-one-dimensional system TiOCl. VOCl undergoes a partial Mott transition with the formation of triangular V clusters.

Chapter 8

Spin-Peierls distortions in TiPO$_4$[1]

8.1 Introduction

The complex interplay between spin, charge, orbital, and lattice degrees of freedom has made low-dimensional quantum spin magnets with strong antiferromagnetic (AF) spin-exchange coupling prime candidates for studying unusual magnetic ground states [147, 148]. For instance, a progressive spin-lattice dimerization in one-dimensional AF Heisenberg chains, which occurs below a critical temperature and induces a singlet ground state with a magnetic gap, is commonly referred to as spin-Peierls (SP) transition [149]. Such a transition, first observed in organic materials [150–152] attracted renewed attention when the first inorganic SP system, CuGeO$_3$ with Cu^{2+} spin $S =1/2$ entities ($T_{SP} \sim 15$ K), was discovered about two decades ago [153]. The critical temperature of SP systems is essentially proportional to the intrachain spin-exchange interaction, J [154]. The search for systems with even higher SP transition temperatures focused on systems with one electron occupying the $3d$ shell, *e.g.*, systems containing Ti^{3+} cations because the large extension of their magnetic orbitals provides enhanced orbital overlap between adjacent sites. In addition, the weak spin-orbit coupling of these cations makes their spin exchange interactions well described by a Heisenberg Hamiltonian hence enabling comparisons with standard theory [150, 151, 154].

Recently, the compounds TiOX (X = Cl, Br) have been intensively investigated due to their unconventional magnetic and structural properties [34–37, 155–158]. Unlike standard SP systems, TiOCl and TiOBr showed two successive phase tran-

---

[1]This chapter has been published as M. Bykov, J. Zhang, A. Schonleber, A. Wölfel, S.I. Ali, S. van Smaalen, R. Glaum, H.-J. Koo, M.-H. Whangbo, P.G. Reuvekamp, J.M. Law, C. Hoch, and R.K. Kremer. Spin-Peierls distortions in TiPO$_4$. Phys. Rev. B 88, 184420 (2013).

sitions at remarkably high temperatures. Upon cooling a continuous transition is observed at 90 K in TiOCl from the room-temperature phase to an incommensurate (IC) phase, which is followed by a first-order lock-in transition at 67 K into a commensurate SP phase [36, 37, 157–159]. X-ray diffraction studies found a Ti–Ti dimerization along the ribbon chains, which indicates direct exchange interactions between spins of neighboring Ti ions [36]. However, due to the two-dimensional character of the TiOX crystal structure, questions about the strength of the interchain spin-exchange interactions and their involvement in causing two successive transitions remained unanswered [159].

Based on magnetic susceptibility, heat capacity and nuclear magnetic resonance (NMR) measurements, Law *et al.* [53] lately reported an apparently similar SP scenario with two transitions at $T_{c1} = 74$ K and $T_{c2} = 111$ K for titanium orthophosphate, TiPO$_4$, containing Ti^{3+} cations with a $3d^1$ electronic configuration. TiPO$_4$ belongs to the rich family of CrVO$_4$-type oxides, which exhibit a wide range of different magnetic properties [160–166]. Compared to the TiOX compounds, TiPO$_4$ exhibits a significantly less complex crystal structure characterized by edge-sharing TiO$_6$ octahedra forming slightly corrugated TiO$_2$ ribbon chains which are interconnected by sharing corners with PO$_4$ tetrahedra (Fig. 8.1) [167, 168]. The high-temperature magnetic susceptibility of TiPO$_4$ follows very well that of a $S = 1/2$ Heisenberg chain with a remarkably large nearest-neighbor AF spin-exchange constant of 965 K, about 50% larger than those of the TiOX compounds. DFT calculations indicated the interchain spin-exchange to be less than 2% of the intrachain interaction and ESR measurements revealed the anisotropy of the g-factor to be of the order of 1% [169]. Low temperature susceptibility data showed a non-magnetic singlet ground state [53].

Based on ^{31}P NMR measurements, the low-temperature phase ($T < T_{c1}$) was ascribed to a commensurate phase with a Ti–Ti bond alternation along the Ti chains, generating two different P positions. In the intermediate phase, the NMR experiments found a broad asymmetric continuum characteristic for an IC phase [53].

Here we report the discovery of the low-temperature superstructures of TiPO$_4$ by means of temperature-dependent X-ray diffraction experiments. Our measurements provide structural proof for a SP distortion, *i.e.*, a Ti–Ti dimerization along TiO$_2$ ribbon chains parallel to **c**. In the intermediate phase the crystal structure is IC and is characterized by a temperature-dependent modulation of the atom positions with a propagation **q**-vector along **a***. The complete accurate structural analysis supported by density functional calculations, allowed to select the most favorable
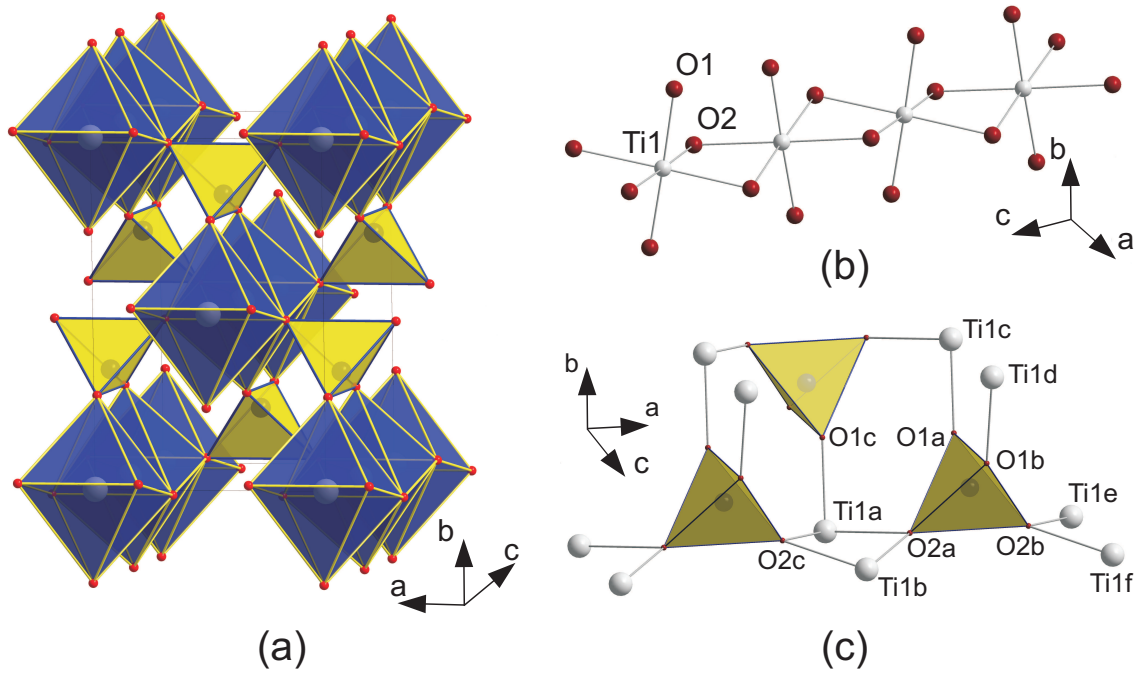
Figure 8.1: (a) Room-temperature crystal structure of TiPO$_4$ with $Cmcm$ space group. (b) Chain of edge-sharing TiO$_6$ octahedra along **c**. (c) Fragment of the crystal structure showing interchain connections through PO$_4$ tetrahedral groups.

structural model for the low-temperature phase, and to uncover the origin of the IC phase.

8.2 Experimental

Temperature-dependent single-crystal X-ray diffraction experiments on a high-quality single crystal of TiPO$_4$ were carried out using synchrotron and laboratory-based radiation sources (for more details see Appendix C.2). Systematic **q**-scans along all principal reciprocal lattice axes and diagonals at 10 K revealed superstructure reflections at positions $(h + \frac{1}{2}, k, l)$, which can be indexed by a propagation vector $\mathbf{q} = (\sigma_1, 0, 0)$, where σ_1 amounts to $\frac{1}{2}$. Several strong superlattice satellite reflections were selected and their positions and integrated intensities were measured as a function of temperature. Their indices are independent of temperature up to 74 K, *i.e.* $\sigma_1 = \frac{1}{2}$. At $T_{c1} = 75$ K σ_1 exhibits a discontinuous jump to 0.527 and increases smoothly to 0.565 up to 110 K. Concomitantly, the satellites decrease their intensity and finally disappear at 112 K (Fig. 8.2). These results show that below T_{c1} TiPO$_4$ forms a superstructure with a doubling of the room-
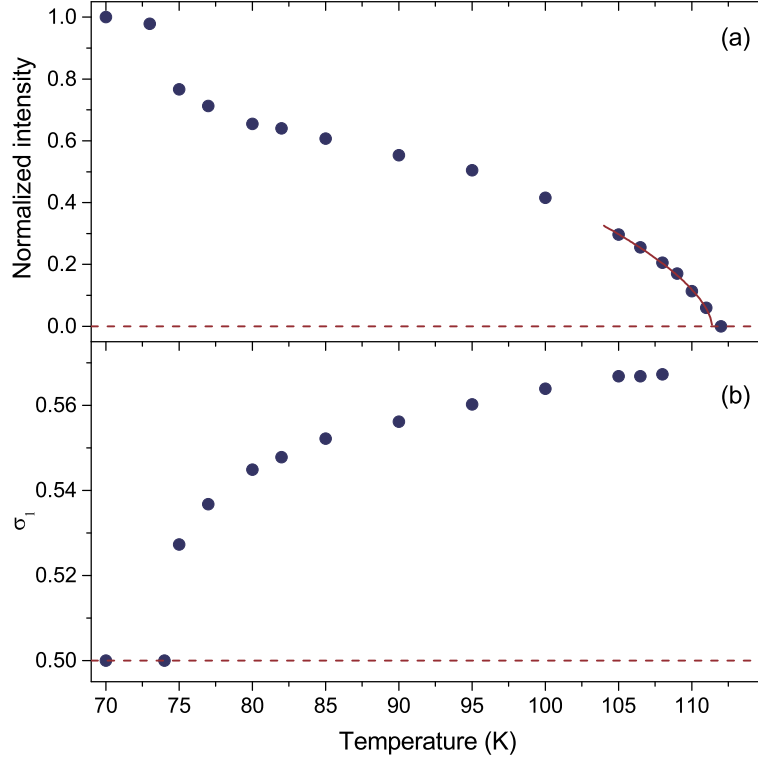
Figure 8.2: (a) Temperature dependence of the normalized intensities of the (2 4 3 -1) satellite Bragg reflection. The solid curve represents the fit with a critical power law with a critical temperature of $T_{c2} = 111.6(3)$ K and a critical exponent of 0.32(2), consistent with standard universality classes. (b) Temperature dependence of the σ_1 component of $\mathbf{q} = (\sigma_1, 0, 0)$. Errors are smaller than the symbol sizes.

temperature unit cell along $\mathbf{a}$, whereas the crystal structure of the intermediate phase is incommensurately modulated. The discontinuity in σ_1 at T_{c1} (Fig. 8.2(b)) indicates a weak first-order character of the phase transition, as is also supported by thermal hysteresis in the susceptibility and heat capacity measurements [53]. The smooth decrease of the satellite intensities on heating indicates a second-order phase transition at T_{c2}. The change of length in dependence on temperature of an oriented single crystal (length~1 mm) was followed by cooling and heating the sample with a miniature capacitance dilatometer (Appendix C.3). Two phase transitions are also found in the thermal expansion data displayed in Fig. 8.3, then providing consistent transition temperatures of 74.9 K and 112.5 K, respectively. The thermal hysteresis of c at T_{c1} (see lower inset on Fig. 8.3) without a sharp discontinuity again manifests the weak first-order nature of this transition. As also seen in temperature dependent X-ray diffraction data down to 100 K [169], the length change with decreasing temperature of the lattice is distinctly anisotropic
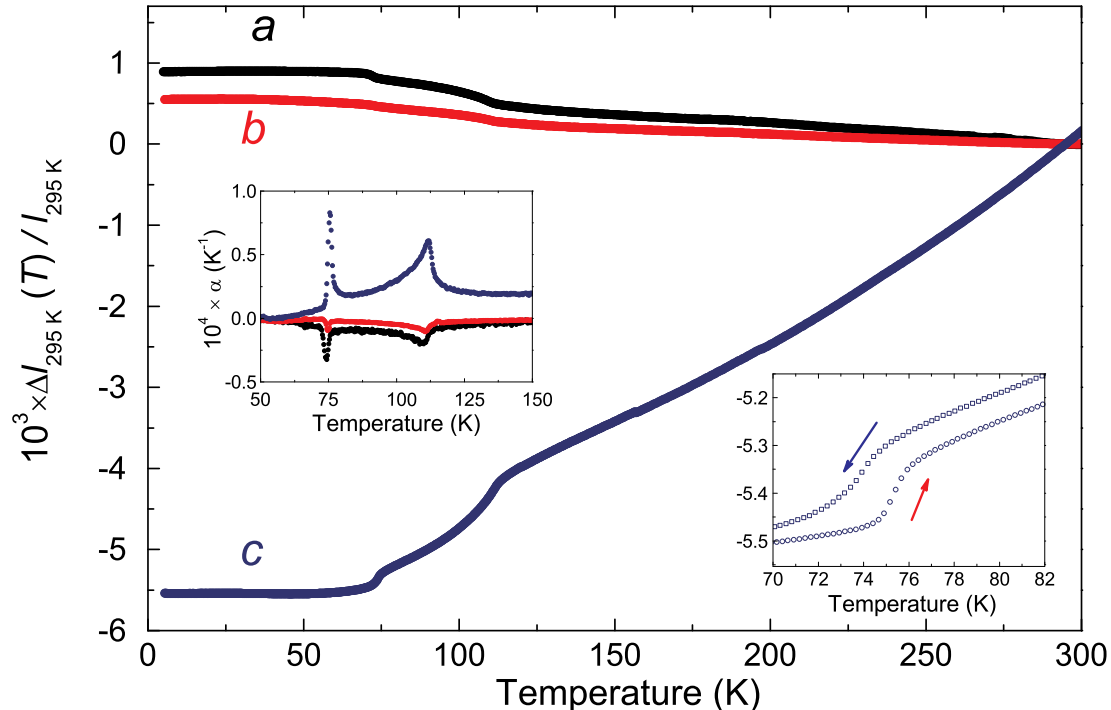
Figure 8.3: Relative length change (w. r. t. 295 K) of a single crystal of TiPO$_4$ along the three crystallographic directions as indicated. The upper inset displays the thermal expansion coefficients using the same color code. The lower inset magnifies the thermal hysteresis around the transition to the commensurate low-temperature phase.

and characterized by an expansion upon cooling along **a** and **b** perpendicular to the Ti chains, whereas a contraction of the crystal along the Ti chains (along **c**) is observed. Two complete data sets of integrated intensities of Bragg reflections were collected at 10 K and 82 K, corresponding to the commensurate and the IC phases, respectively. All observed Bragg reflections could be indexed with respect to the unit cell of the average structure and a modulation wavevector **q**, using four integers $(hklm)$.

This allows the use of the superspace approach for structural analysis, where the structural parameters are separated into the parameters of the average structure defined by main reflections ($m = 0$) and the modulation parameters defined by satellite reflections ($m \neq 0$) [52]. The latter characterize relatively small displacements of the atoms, which can be described by a first-order Fourier series for the modulation functions:

$$u_i^\mu(\bar{x}_4) = A_i(\mu)\sin(2\pi\bar{x}_4) + B_i(\mu)\cos(2\pi\bar{x}_4), \qquad (8.1)$$

100

for $i = x$, y and z. μ indicates the atom Ti, P, O1 or O2 in the average-structure unit cell, and $\bar{x}_4 = t + \mathbf{q} \cdot \bar{\mathbf{x}}$, where $\bar{\mathbf{x}}$ is the atomic position in the average structure. The parameter t represents the phase of the modulation.

It should be noted that no high-order satellites ($|m| > 1$) were observed at 10 K. The commensurate value of σ_1 at 10 K implies that the satellites with $|m| = 2$ would appear at the positions of the main reflections forbidden by the C-centering of the lattice. No such reflections were detected during the data collection in the low-angle region ($\sin\theta/\lambda < 0.31$), and they were excluded for the further full data collection. No explicit search was performed for the second-order satellites at 82 K mainly due to the beam time limitations. Furthermore, in the IC phase at 82 K, reflections with $|m| = 1$ have $< I/\sigma(I) >$ equal to 10.9 (compared to 200.8 for main reflections). Therefore, higher order satellites, if any, are expected to be too weak to have been observed in our experiment. The intensities of satellite reflections of order m are approximately proportional to the square of the amplitude of the mth-order harmonic [52]. The absence of satellites with $|m| > 1$ implies that the modulation functions can be successfully described by exclusively first-order harmonics (Eq. 8.1). All structure refinements were performed with standard software (Appendix C.2).

Both low-temperature structures can be described by the same orthorhombic superspace group $Cmcm(\sigma_1 00)0s0$ (No. 63.1.13.8 with standard setting $Amam(00\sigma_3)0s0$) [93, 94]. In the description of the lock-in phase as commensurately modulated structure, different sections $t = t_0$ of superspace lead to different symmetries of the fourfold, $2a \times b \times c$ superstructure.[1] The best fit to the diffraction data was obtained for $t_0 = \frac{1}{8}$, which corresponds to space group $Pbnm$ for the superstructure (Fig. 8.4(d)). However, good agreement was also found for $t_0 = 0$, corresponding to space group $Pmnm$ (Fig. 8.4(b)), and for $t_0 = \frac{1}{16}$, corresponding to the non-centrosymmetric space group $P2_1 nm$ (Fig. 8.4(c)).

8.3 Discussion

The most prominent feature of the $Pbnm$ low-temperature superstructure is a dimerization of the Ti chains with a Ti–Ti bond alternation along $\mathbf{c}$ of about 3% ($d_1 = 3.134(5)$ and $d_2 = 3.230(5)$ Å (see Table C.8)), almost four times larger than that in $CuGeO_3$ [170].

---

[1]Note that the primitive unit cell volume of the low-temperature superstructures is four times larger than that of the high-temperature $Cmcm$ phase. Therefore we refer these superstructures to as fourfold.
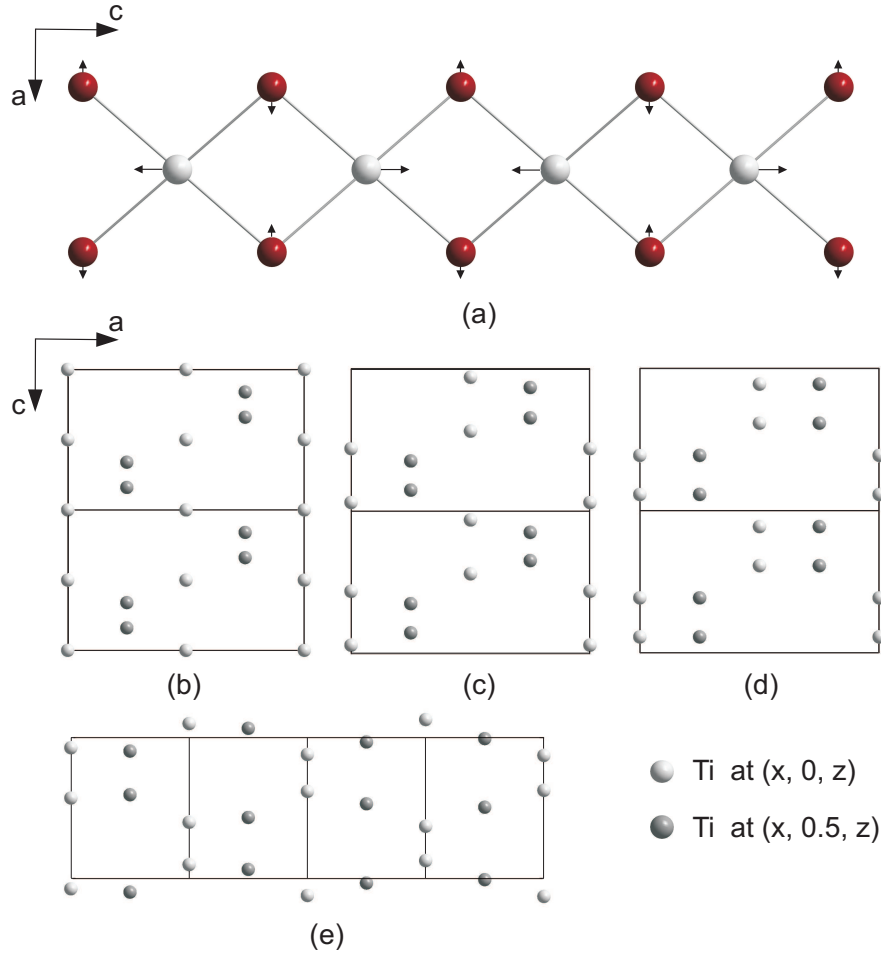
Figure 8.4:   (a) Single TiO$_2$ chain from the crystal structure of TiPO$_4$. Arrows indicate the atomic displacements corresponding to the *Pbnm* structure model for the spin-Peierls phase at 10 K. (b – d) Projection of the crystal structures at 10 K along [010]. (b) $2a \times b \times c$ supercells with *Pmnm* symmetry, (c) with *P2$_1$nm* symmetry, (d) with *Pbnm* symmetry. (e) Incommensurate phase at 82 K represented by $4a \times b \times c$ basic-structure unit cells. Only Ti atoms are shown. Basic-structure coordinates are $x = 0$ or $1/2$ and $z = 0$ or $1/2$. For clarity all atomic displacements have been multiplied by 30.

Table 8.1: Relative energies of the three possible low-temperature structures ($T < 75$ K) obtained from DFT $+ U$ calculations.

U (eV)	$Pbnm$ (meV)	$P2_1nm$ (meV)	$Pmnm$ (meV)
2	0	0.43	0.56
3	0	0.43	0.57

Compared to the room-temperature structure, the TiO$_6$ octahedra at 10 K are slightly more distorted, but they remain compressed with Ti–O distances to apical oxygen atoms (O1) clearly shorter than distances to equatorial oxygen atoms (O2). The Ti $3d$ orbitals are split into e_g and t_{2g} orbitals. With a coordinate system chosen as $z \parallel b$, $x \parallel a$, and $y \parallel c$, the t_{2g} orbitals are further split into $d_{x^2-y^2}$ and almost degenerate d_{yz} and d_{xz}, the latter being higher in energy due to the compression of the TiO$_6$ octahedra [171]. The structure model thus is in agreement with direct magnetic exchange between unpaired electrons occupying the $d_{x^2-y^2}$ orbitals on Ti^{3+} atoms neighboring along **c**. While the displacements of Ti atoms are driven by SP coupling, the modulations of other atoms follow those of Ti to retain favorable bonding configurations. The latter is also implied by the negative thermal expansion along **a** and **b**. In the structure model described by the space group $Pmnm$ only Ti chains in every second layer undergo a dimerization (Fig. 8.4(b)), in disagreement with the magnetic susceptibility data showing a non-magnetic singlet ground state below T_{c1} [53]. The structure model $P2_1nm$ (Fig. 8.4(c)) exhibits varying Ti–Ti dimerizations generating a total of four different P atoms. However, since the positional parameters of two pairs of P atoms are only marginally different (Section C.4), this finding is at first hand not inconsistent with the NMR data detecting only two ^{31}P lines [53].

In order to find the relative energies of these three putative low-temperature structures, density functional theory (DFT) electronic band structure calculations were carried out by employing the Vienna *ab initio* simulation package [172–174] with the projected augmented wave method and the generalized gradient approximation (GGA) for the exchange and the correlation functional [175]. To account for the electron correlation associated with the Ti $3d$ state, we performed DFT plus on-site repulsion (DFT+U) calculations [176] with an effective $U_{\text{eff}} = U - J = 2$ and 3 eV on Ti. Details of the calculations can be found in Appendix C.1. The DFT calculations clearly identify the $Pbnm$ model as the structure with minimum energy (Table 8.1), supporting the results of the structure refinements. The two other structure models, however, are surprisingly close in energy, with consequences

for the IC phase (see below).

A peculiarity of TiPO$_4$ is that a dimerization of the Ti chains along **c** is brought about by a doubling of the unit cell along **a**. This feature is explained by the loss of point symmetry accompanying the loss of translational symmetry, and the fact that the basic structure already contains two Ti atoms within one period along **c**. The IC phase at intermediate temperatures is characterized by an IC modulation along **a** as defined by **q** $= (\sigma_1, 0, 0)$ (Fig. 8.2). In the absence of a non-zero component along **c***, the Ti chains along **c** remain dimerized, but chains centered at different x possess different degrees of dimerization (Fig. 8.4(e)). Some chains appear similarly dimerized as those in the low-temperature *Pbnm* structure, while other chains are more like those in the *P*2$_1$*nm* or *Pmnm* low-temperature structures (compare Figs. 8.4(b)–(e)). In this respect the IC structure of TiPO$_4$ is essentially different from the IC structure of TiOCl. An incommensurate component of the **q** vector along the chain direction in TiOCl determines that all chains are identically modulated in TiOCl, whereas the zero component of the **q** vector along the chain direction makes all chains differently dimerized in the IC structure of TiPO$_4$.

Since DFT calculations have revealed that the different models for the low-temperature crystal structure exhibit only small differences in energy (Table 8.1), we propose that the IC phase should be considered as a combination of all possible low-temperature structures. Fluctuations between energetically almost degenerate structures with different P environments, allow one to understand the very broad ^{31}P NMR continuum in the IC phase spreading out over more than 200 ppm. In the commensurate phase below T_{c1} the NMR spectrum contracts to two very sharp resonance lines separated by only ~ 5 ppm [53]. The dilatometry experiments revealed a negative thermal expansion perpendicular to the Ti chains, whereas a contraction of the lattice of significantly larger magnitude is seen along **c** (Fig. 8.3). These findings indicate that elastic interactions mediated by the PO$_4$ units have to be considered between neighboring chains, in addition to the displacements of the Ti atoms driven by the SP dimerization.

The variation of a structural parameter (*e.g.* interatomic distances or bond angles) within the IC structure is given by a t-plot. The latter gives the value of this parameter as a function of the phase t of the periodic modulation wave [52]. An extended discussion of the t-plots is given in Appendix C.4. Selected t-plots are presented in Fig. 8.5. Expectedly, the largest variation holds for Ti-Ti intrachain distances (Fig. 8.5(a)), while the small variation of P–O distances and O–P–O bond angles in the IC structure (Fig. 8.5(b),(c)) demonstrate that the PO$_4$ tetrahedra behave to a large extent as rigid units. On the other hand, the apical oxygen atoms of
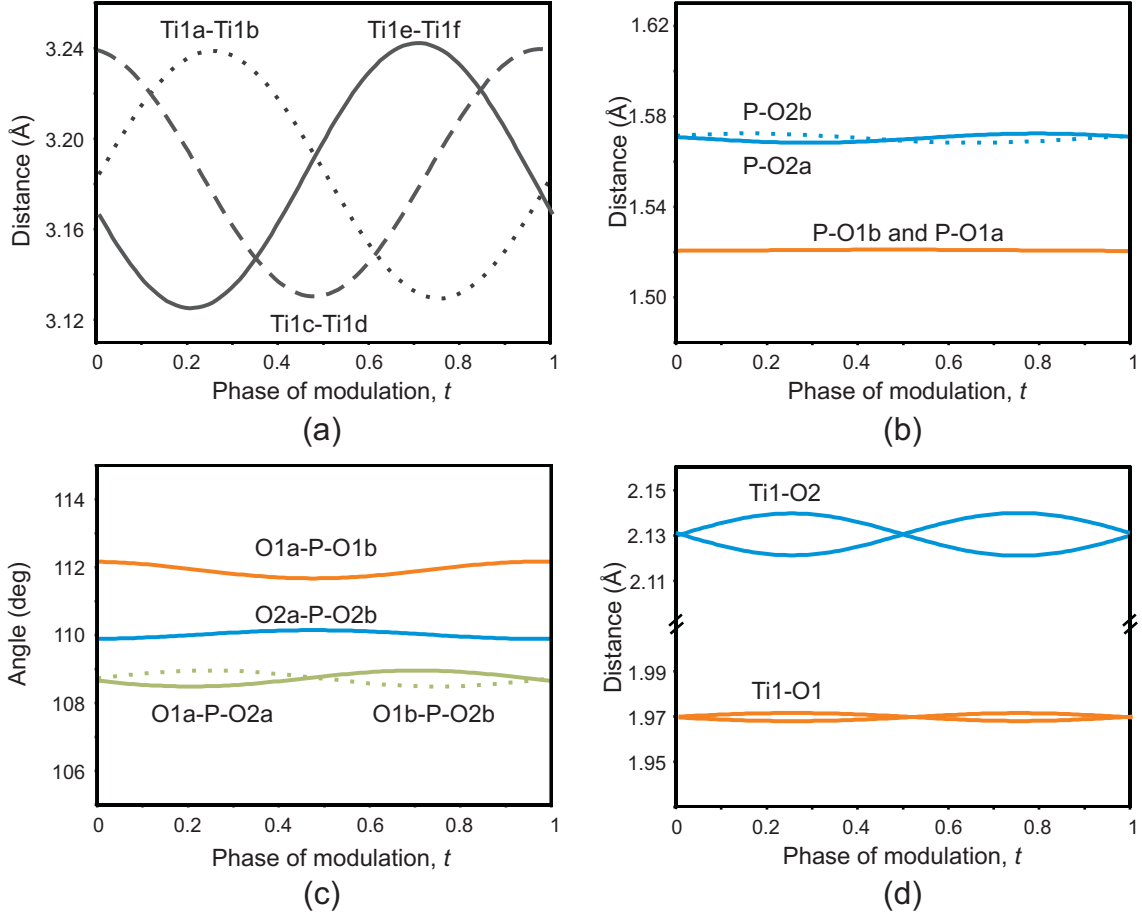
Figure 8.5: Selected t-plots for the IC phase at 82 K. Atom labels refer to the Fig. 8.1.

the TiO$_6$ octahedra (O1 in Fig. 8.1) follow and adjust to the SP dimerization of the Ti atoms, so that Ti–O1 distance variation is very small (Fig. 8.5(d)). Consequently, the shifts of the apical oxygen atoms will also affect the adjustment of the equatorial oxygen atoms (O2 atoms in Fig. 8.1) of TiO$_6$ octahedra in neighboring chains. The competition and frustration of the SP distortion in neighboring Ti chains, mediated by the elastic coupling by rigid PO$_4$ units, can explain the structural fluctuations in the IC phase indicated by the NMR experiment.

The proposed IC model also explains the behavior of the magnetic susceptibility reported in Ref. [53]. The formation of spin-singlets starts below T_{c2}, and expectedly results in the drop of the magnetic susceptibility. Between T_{c2} and T_{c1} χ is defined by the non-dimerized and slightly dimerized spin chains. As evidenced by the gradual rise of satellite intensities on further cooling (Fig. 8.2(a)), the modulation amplitudes increase, and, therefore, the number of weakly dimerized chains decreases. Such chains disappear below T_{c1}, resulting in almost zero magnetic susceptibility in

the lock-in phase.

8.4   Conclusions

In conclusion, TiPO$_4$ shows a SP phase below $T_{c1} = 74$ K, that is characterized by a dimerization of the Ti chains along **c**. The occurrence of an IC phase extending up to temperatures significantly above the T_{c1} is unexpected within a standard SP scenario. The IC phase is ascribed to energetically almost degenerate phases resulting from a competition and frustration of the SP transition due to elastic coupling between neighboring Ti chains. The transitions between the different phase involve sizeable lattice anomalies with a contraction of the lattice along the spin chains whereas perpendicular to the Ti chains an expansion of the lattice is found.

Chapter 9

Summary

This thesis reports on structural studies of low-dimensional systems MOCl (M = Sc, Ti, V, Cr, Fe) and TiPO$_4$ subjected to non-ambient conditions. Transition metal oxychlorides MOCl have been investigated at high pressures in diamond anvil cells by means of single-crystal synchrotron X-ray diffraction and by complementary techniques including Raman and Mössbauer spectroscopies and powder X-ray diffraction. The results reveal a plethora of high-pressure phase transitions in MOCl. A structural analysis allowed to associate the driving forces of the transitions either with the optimization of crystal packing, with the enhancement of low-dimensional magnetic properties, or with changes in electronic structures. TiPO$_4$ has been studied by means of single-crystal X-ray diffraction at low temperatures. A structural proof of the spin-Peierls transition in this compound has been obtained. Furthermore, a novel incommensurately modulated phase of TiPO$_4$ has been discovered and characterized.

At ambient conditions the compounds MOCl are isostructural and possess layered structures, which consist of double layers M–O, separated by Cl bilayers. In this work, these crystal structures were followed as function of pressure. The common structure type of MOCl is responsible for the similarities in their high-pressure behaviors, while the differences are defined by the different electronic configurations of M^{3+}. So, common structural transitions have been observed in each MOCl compound studied. The transitions are related to the fact that an optimal packing of Cl atoms is not realized within the ambient-pressure structure type due to the restrictions implied by M–O bonds. At elevated pressures the situation is reached where some Cl$\cdots$Cl contacts are very short, but others are much longer than the optimal value (twice van der Waals radius of Cl atom). It is not possible to balance the Cl packing without the distortion of the M–O slabs. The transition occurs when the gain in energy arising from the redistribution of Cl atoms compensates the cost

of elastic energy for distortion of the M–O slabs. A competition between optimal packing of Cl atoms and restrictions by M–O and M–Cl bonds leads to the incommensurability of the high-pressure structures. The superspace approach has been employed to describe the high-pressure incommensurate structures of MOCl. The modulation wave vectors have the form $\mathbf{q} = \sigma_1\mathbf{a}^* + \frac{1}{2}\mathbf{c}^*$, where σ_1 is an irrational number, which is specific for each transition metal and may vary with pressure. At higher pressures incommensurate structures transform to commensurate superstructures.

As has been mentioned above, the electronic configuration of M^{3+} is crucial for the understanding of high-pressure behaviors of MOCl. A single d-electron and orbital order are responsible for the quasi-one-dimensional nature of magnetic interactions in TiOCl. Application of high pressure to TiOCl enhances the temperature of spin-Peierls transition in TiOCl and leads to an incommensurately modulated high-pressure phase, that is similar to the incommensurate low-temperature phase, stable between 67 and 90 K. Further increase of pressure results in a very complex incommensurate structure with two modulation wave vectors related to inherently different distortion mechanisms: spin-Peierls-like (defined by low-dimensional magnetism) and optimisation of crystal packing (pure structural transition). At higher pressures this incommensurate phases transforms to a commensurate $5a \times 2b \times 4c$ superstructure.

V^{3+}, Cr^{3+} and Fe^{3+} have more than one d-electron and, therefore, have additional strong magnetic interchain couplings. This doesn't allow spin-Peierls state to develop in VOCl, CrOCl and FeOCl. However, VOCl, CrOCl and FeOCl are Mott insulators with different critical metal–metal distances R_c for electron delocalization. Among the considered transition metal cations, Cr^{3+} has the shortest R_c which has not been reached in CrOCl up to 57 GPa. Consequently, no Mott transition and related distortions have been observed. This allowed to investigate the evolution of the incommensurate and the lock-in phases in a much wider range of pressures than it was possible in other MOCl compounds. For CrOCl the σ_1 component of the $\mathbf{q}$-vector is pressure-dependent. Between 16.4 and 30.3 GPa it varies slightly, while above 30.3 GPa it rapidly grows with pressure and jumps to a rational value of $\frac{1}{3}$ at 57 GPa. The atomic modulation amplitudes grow significantly up to 30.3 GPa and stay almost constant at higher pressures.

High-pressure behavior of VOCl has been studied up to 50.5 GPa. Apart from a structural normal-to-incommensurate phase transition at ~ 15 GPa VOCl undergoes a partial Mott transition at ~ 20 GPa with formation of a monoclinic $3a \times 3b \times 2c$ superstructure. The superstructure contains triangular V clusters with homopolar

V–V bonds within the clusters. This is a rare case of the electronic transition, where the electron delocalization occurs within some metallic clusters with $R_{\text{metal–metal}} <$ R_c, while the distances between the clusters are larger than R_c, so that there is no net metallic conductivity. At higher pressures the symmetry of the $3a \times 3b \times 2c$ superstructure changes from monoclinic to orthorhombic without substantial atomic rearrangements.

Single-crystal X-ray diffraction data on FeOCl have been collected at 15.0 and at 22.7 GPa, where FeOCl adopts an incommensurately modulated structure and a $4a \times b \times 2c$ superstructure respectively. FeOCl has been additionally studied by means of Mössbauer spectroscopy. It was shown that the structural transition at $\sim$ 15 GPa is not related to changes in magnetic structure of FeOCl.

The spin-Peierls compound $TiPO_4$ has been studied by means of single-crystal X-ray diffraction in a temperature range from 292 K down to 10 K. On cooling $TiPO_4$ undergoes two consecutive phase transitions at $T_{c2} = 111.6(3)$ K and at $T_{c1} = 74.5(5)$ K. It has been found that the low-temperature phase, stable below T_{c1}, is characterized by dimerization of the Ti chains. Between T_{c1} and T_{c2} the structure of $TiPO_4$ is incommensurately modulated. The incommensurate phase is ascribed to energetically almost degenerate phases resulting from a competition and frustration of the spin-Peierls transition due to elastic coupling between neighboring Ti chains.

Chapter 10

Zusammenfassung

Inhalt der vorliegenden Arbeit sind Strukturuntersuchungen an den niedrig-dimensionalen Systemen MOCl (M = Sc, Ti, V, Cr, Fe) und $TiPO_4$ als Funktion von Druck und Temperatur. Die Übergangsmetalloxichloride MOCl wurden bei hohen Drücken in Diamantstempelzellen mittels Einkristall-Synchrotron-Röntgenstrahlbeugung und den komplementären Methoden Raman- und Mössbauer-Spektroskopie und Pulver-Röntgenstrahlbeugung gemessen. Als Ergebnis konnte eine Vielzahl an Phasenumwandlungen von MOCl bei hohen Drücken gefunden werden. Die Analyse der Kristallstrukturen erlaubte es, als treibende Kraft der Phasenumwandlungen entweder die Optimierung der Kristallpackung, einhergehend mit einer Verstärkung der niedrig-dimensionalen magnetischen Eigenschaften, oder die Änderung in der elektronischen Struktur zu definieren. $TiPO_4$ wurde mittels Einkristall-Röntgenstrahlbeugung bei tiefen Temperaturen gemessen und der strukturelle Beweis der Spin-Peierls-Umwandlung für diese Verbindung erbracht. Desweiteren wurde eine neue inkommensurabel modulierte Phase von $TiPO_4$ gefunden und charakterisiert.

Unter Normalbedingungen sind die Verbindungen MOCl isostrukturell und besitzen Schichtstrukturen aus Doppelschichten M–O, die durch Cl-Doppelschichten voneinander getrennt sind. In dieser Arbeit wurden nun die Strukturen als Funktion des Drucks untersucht. Der gemeinsame Strukturtyp der MOCl-Verbindungen ist für ihr ähnliches Verhalten bei hohen Drücken verantwortlich, während die Unterschiede durch die unterschiedlichen Elektronenkonfigurationen der M^{3+} erklärt werden können. Gemeinsame strukturelle Phasenumwandlungen wurden in allen untersuchten MOCl-Verbindungen gefunden. Die Umwandlungen begründen sich in der nicht-optimalen Packung der Cl-Atome in der Struktur bei Normaldruck, die durch die M–O-Bindungen verhindert wird. Bei höheren Drücken kommt es schließlich dazu, dass die einen Cl$\cdots$Cl-Kontakte sehr kurz werden, während an-

dere deutlich länger als der optimale Wert von "zweimal der van der Waals Radius" der Cl-Atome sind. Da es aber nicht möglich ist, die Cl-Packung auszugleichen, ohne dabei die M–O-Schichten zu verzerren, tritt die Phasenumwandlung erst auf, wenn der Energiegewinn, der durch die Umverteilung der Cl-Atome entsteht, die Kosten der elastischen Energie für die Verzerrung der M–O-Schichten kompensiert. Die Konkurrenz zwischen optimaler Packung der Cl-Atome und der Beschränkung durch die M–O- und M–Cl-Bindungen führt zur Inkommensurabilität in den Hochdruckstrukturen. Die inkommensurablen Hochdruckstrukturen der MOCl-Verbindungen wurden unter Anwendung der Superraum-Methode beschrieben. Die Modulationswellenvektoren können als $\mathbf{q} = \sigma_1\mathbf{a}^* + \frac{1}{2}\mathbf{c}^*$ geschrieben werden, wobei σ_1 die irrationale Zahl ist, welche für jedes Übergangsmetall charakteristisch ist und sich als Funktion des Drucks ändern kann. Bei höheren Drücken wandeln sich die inkommensurablen Strukturen in kommensurable Überstrukturen um.

Wie bereits erwähnt, ist die Elektronenkonfiguration der M^{3+} entscheidend für das Verständnis des Hochdruckverhaltens der MOCl-Verbindungen. Das einzelne d-Elektron und Orbital-Ausordnung sind für die quasi-eindimensionale Natur der magnetischen Wechselwirkungen in TiOCl verantwortlich. Die Einwirkung hoher Drücke auf TiOCl führt zu einer Erhöhung der Temperatur der Spin-Peierls-Umwandlung und zu einer inkommensurabel modulierten Hochdruckphase, die der zwischen 67 und 90 K stabilen inkommensurablen Tieftemperaturphase ähnlich ist. Eine weitere Druckerhöhung resultiert in einer sehr komplexen inkommensurablen Struktur mit zwei Modulationswellenvektoren, die zwei inhärenten, unterschiedlichen Verzerrungsmechanismen zuzuordnen sind: der eine Mechanismus ist Spin-Peierls-ähnlich (definiert durch den niedrig-dimensionalen Magnetismus), der andere ist die Optimierung der Kristallpackung (eine rein strukturelle Umwandlung). Diese inkommensurable Phase geht dann bei noch höheren Drücken in eine kommensurable $5a \times 2b \times 4c$ Überstruktur über.

Da V^{3+}, Cr^{3+} und Fe^{3+} mehr als ein d-Elektron besitzen, zeigen sie auch eine zusätzliche starke Kopplung zwischen den Ketten. Dadurch ist eine Ausformung des Spin-Peierls-Zustands in VOCl, CrOCl und FeOCl nicht möglich. Jedoch sind VOCl, CrOCl und FeOCl Mott-Isolatoren mit unterschiedlichen kritischen Metall–Metall-Abständen R_c für die Elektronen-Delokalisierung. Für die untersuchten Übergangsmetallkationen hat Cr^{3+} den kürzesten Abstand R_c, der durch Druckerhöhung selbst bei 57 GPa noch nicht erreicht wurde. Als Folge wurden hier keine Mott-Umwandlung und die damit zusammenhängenden Verzerrungen beobachtet. Dies erlaubte aber, das Verhalten der inkommensurablen Struktur und der sogenannten "Lock-in"-Phase in einem größerem Druckbereich zu studieren,

was bei den anderen MOCl-Verbindungen nicht möglich war. Für CrOCl ist die σ_1-Komponente des **q**-Vektors druckabhängig. Zwischen 16.4 und 30.3 GPa verändert sie sich nur leicht, während sie oberhalb von 30.3 GPa mit zunehmenden Druck stark und dann bei 57 GPa sprunghaft zum rationalen Wert $\frac{1}{3}$ ansteigt. Die atomaren Modulationsamplituden werden bis 30.3 GPa signifikant größer, bleiben aber dann bei höheren Drücken nahezu konstant.

Das Hochdruckverhalten von VOCl wurde bis zu einem Druck von 50.5 GPa untersucht. Abgesehen von der "Normal-zu-inkommensurabel"-Phasenumwandlung bei $\sim$ 15 GPa durchläuft VOCl eine partielle Mott-Umwandlung bei $\sim$ 20 GPa unter Ausbildung einer monoklinen $3a \times 3b \times 2c$ Überstruktur. Diese Überstruktur enthält dreieckige V-Cluster mit homopolaren V–V-Bindungen in den Clustern. Dies stellt einen der wenigen Fälle einer elektronischen Umwandlung dar, bei der die Elektronendelokalisierung innerhalb einiger metallischer Cluster mit $R_{\text{Metall–Metall}} < R_c$ auftritt, während die Abstände zwischen den Clustern größer als R_c sind, wodurch dann keine resultierende metallische Leitfähigkeit entsteht. Bei höheren Drücken ändert sich die Symmetrie der $3a \times 3b \times 2c$ Überstruktur von monoklin nach orthorhombisch, jedoch ohne eine nennenswerte atomare Umgruppierung.

Einkristall-Röntgenstrahlbeugungsdaten wurden für FeOCl bei 15.0 und bei 22.7 GPa gemessen. FeOCl besitzt bei diesen Drücken eine inkommensurabel modulierte Struktur bzw. eine $4a \times b \times 2c$ Überstruktur. Zusätzlich wurde an FeOCl druckabhängige Mössbauer-Spektroskopie durchgeführt. Es konnte gezeigt werden, dass die strukturelle Umwandlung bei $\sim$ 15 GPa nicht mit Änderungen in der magnetischen Struktur von FeOCl zusammenhängt.

Die Spin-Peierls-Verbindung TiPO$_4$ wurde im Temperaturbereich von 292 K bis 10 K mittels Einkristall-Röntgenstrahlbeugung untersucht. Bei Abkühlung durchläuft TiPO$_4$ zwei aufeinanderfolgende Phasenumwandlungen bei $T_{c2} = $ 111.6(3) K und bei $T_{c1} = $ 74.5(5) K. Die Tieftemperaturphase unterhalb T_{c1} ist durch eine Dimerisierung der Ti-Ketten charakterisiert. Zwischen T_{c1} und T_{c2} ist die Struktur von TiPO$_4$ inkommensurabel moduliert. Diese inkommensurable Phase ist energetisch nahezu degenerierten Phasen zugerechnet, die aus der Konkurrenz und der Frustration der Spin-Peierls-Umwandlung aufgrund der elastischen Kopplung zwischen benachbarten Ti-Ketten entsteht.

Appendix A

Pressure-induced normal-incommensurate and incommensurate-commensurate phase transitions in CrOCl

A.1 Details of the experiment and of the data processing

Single-crystal X-ray diffraction experiments have been performed on crystals loaded in BX90 diamond anvil cells [60] equipped with Boehler-Almax diamonds [59]. Pressures were obtained from the shifts of the R_1 fluorescence line of ruby [63]. The fluorescence was measured directly before and immediately after the data collections, in order to establish the magnitudes of pressure variation during each experiment. Neon crystallizes at approximately 4.8 GPa [106], but its diffraction peaks become clearly visible only at 13 GPa. Therefore, the lattice parameter of Ne could be obtained and was used as an additional pressure indicator [64]. The maximal differences between the pressures measured before and after the data collections, and determined by different methods did not exceed 0.7 GPa.

For Raman spectroscopy experiments a BX90 DAC with standard design diamond anvils (250 μm culet size) was used. Raman spectra were measured in backscattering geometry, employing a Dilor XY Raman spectrometer using an Ar^+ ion laser (Coherent Innova 300) with a wavelength of 514.5 nm, and possessing a spectral resolution of 1 cm^{-1}. The laser power was kept below 2 mW, in order to avoid laser-heating of the sample. Phonon frequencies were obtained by fitting

Pearson VII functions to the experimental peaks.

Integrated intensities of Bragg reflections were obtained from the measured diffraction images by the software $CrysAlis^{Pro}$. It appeared necessary to convert the format of the Mar555 images to Mar345 format. Custom-made software available at beamline ID09A was used for this purpose. Perkin Elmer images in .tif format were converted to the esperanto image type that is supported by the latest version of $CrysAlis^{Pro}$ [50]. Components of the modulation wave vector were refined simultaneously with the orientation matrix against the observed positions of the reflections, using the computer program NADA as implemented in $CrysAlis^{Pro}$ [92]. All equation of state fits were performed with EosFit7c [177].

A.2 Details of structure solution and refinement

Structure refinements for the low-pressure phases of CrOCl

CrOCl keeps its ambient-pressure structure up to 14.5 GPa. Crystal structures at these pressures were successfully refined against each of the eight data sets of X-ray diffraction data measured at pressures between 0.0001 and 12.95 GPa (Table A.1). The structure published by Forsberg [178] was used as starting model. Due to the limited coverage of reciprocal space in the high-pressure diffraction experiments at the ESRF, it appeared necessary to use a smaller number of independent parameters in the refinements than the three coordinates and nine atomic displacement parameters (ADPs) allowed by symmetry. It was chosen to use isotropic ADPs for Cr and O, thus reducing the number of ADP parameters from 9 to 5. The Cl atoms can be expected to possess large and anisotropic displacement amplitudes, because they form the boundary of the Van der Waals gap. Therefore, Cl was given anisotropic ADPs. This model leads to a pronounced drop in R-factors and is supported by a Hamilton test (0.005 significance level), while anisotropic refinement of Cr and O atoms does not lead to a significant lowering of the agreement factors. Data obtained upon decompression contained more reflections, which allowed refinement anisotropic ADPs for all atoms (Table A.2). Larger mosaic spreads at higher pressures reduced the importance of extinction. Therefore, an extinction correction was not applied at pressures above 7.1 GPa. All refinements smoothly converged to excellent fits to the diffraction data (Tables A.1 and A.2).

Structure refinement of the incommensurate high-pressure phase of CrOCl

CrOCl is found to undergo a phase transition at a pressure between 15.3 and 16.4 GPa. The phase transition is evidenced by the presence of weak superlattice reflections in the diffraction patterns at 16.4 GPa and higher pressures. All observed Bragg reflections could be indexed on the basis of a unit cell that is closely related to the unit cell below 14.5 GPa, together with a modulation wave vector $\mathbf{q} = (\sigma_1, 0, \frac{1}{2})$. Analysis of the diffraction symmetry and the reflection conditions revealed two possible superspace groups: $Pmmn(\sigma_1, 0, \frac{1}{2})00s$ and $Pmmn(\sigma_1, 0, \frac{1}{2})000$. These groups are different settings of the superspace group $Pmnm(\sigma_1, 0, \frac{1}{2})000$ (No. 59.1.10.6) [93] and can be obtained from each other by a translation of the origin by $(00\frac{1}{2}0)$ in superspace. The superspace group $Pmmn(\sigma_1, 0, \frac{1}{2})00s$ has been chosen in order to keep the atomic coordinates in the basic structure close to those in low-pressure phase structure model. Atomic modulation functions were described by truncated Fourier series for all the atoms. Up to second-order harmonics were used at all pressures except 16.4 GPa, where second-order satellites were not observed, and therefore only first-order harmonics could be used. The ambient-pressure structure model was used as a starting model for the refinements of the basic structure against the main reflections. Subsequently, small but arbitrary values were given to the modulation amplitudes. Refinement of all parameters against all reflections resulted in a smooth convergence and a good fit to the diffraction data at each pressure (Tables A.1 and A.2).

At pressures below 30 GPa, σ_1 is close to the rational number $\frac{2}{7} = 0.2857$. This value would imply a commensurate modulation that can alternatively be described as a superstructure with a 14-fold, $7a \times b \times 2c$ supercell. The superspace group of the modulated-structure description implies different symmetries of the supercell in dependence on the section t_0 of superspace. Possible 3-dimensional (3D) space groups are $Pcmn$ for $t_0 = 0 + \frac{n}{14}$, $Pmmn$ for $t_0 = \frac{1}{28} + \frac{n}{14}(n = 0, 1, \cdots, 13)$, and $P2_1mn$ for other values of t_0. In addition to the refinement of the incommensurate structure model, superstructure models were tested by commensurate superspace refinements with t_0 equal to 0, $\frac{1}{28}$ and 0.050508, respectively. Differences between the R-factors of these four refinements did not exceed 0.01 % (Table A.3). As a consequence, it is impossible to distinguish between different superstructures and between incommensurate and commensurate modulations, solely on the basis of the refinements. This ambiguity may be the result of having available only highly incomplete data sets. Furthermore, the 14-fold superstructure would allow satellites up to the seventh order, but only first- and second-order satellites were observed, which again

diminishes the sensitivity of the diffraction to a possible commensurability of the modulation.

On the other hand, the pressure dependence of the σ_1 reveals an incommensurate modulation for pressures between 30 and 51 GPa, while phase transitions between 16.4 and 51 GPa were not observed. This strongly suggests the incommensurability of this high-pressure phase of CrOCl. However, a commensurate-to-incommensurate transition at approximately 30 GPa cannot be entirely excluded on the basis of the present data.

Structure refinement of the incommensurate high-pressure phase of FeOCl at 15 GPa

In FeOCl at 15 GPa satellite reflections can be indexed with the $\mathbf{q}$-vector $(0.26, 0, \frac{1}{2})$. The superspace symmetry and the starting structure model for the refinement are the same as for CrOCl. Atomic modulation functions were described as first-order harmonics. Refinement of all parameters against all reflections resulted in a smooth convergence and a good fit to the diffraction data (Table A.4).

Structure refinement of the commensurate high-pressure phases of CrOCl

At $P = 57.2$ GPa the diffraction pattern contains two sets of satellite reflections. One set can be indexed as a lock-in phase of the incommensurately modulated phase at lower pressures, employing $\sigma_1 = \frac{1}{3}$. The second set can be indexed with the different modulation wave vector $\mathbf{q}^2 = (\frac{1}{3}, 0, \frac{1}{3})$. On decompression, at $P = 47.5$ GPa only the lock-in phase survived. Therefore, the two sets of satellite reflections were treated as originating in different parts of the crystal. Unfortunately, we were not able to obtain acceptable fits to the diffraction data at 57.2 GPa. We ascribe this problem to the limited scattering information contained in the data sets, together with the fact that main reflections of the two phases overlap with each other. Consequently, we discuss only main structural features of the second phase, while bond distances, angles and displacement parameters are not reliable. For the structure solution and refinement, the second phase was treated as having monoclinic symmetry (space group $P2_1/m$) with $a = 6.910$, $b = 2.8999$, $c = 9.325$ Å, $\beta = 95.86°$ (Table A.5). The cell transformation $\mathbf{a} + \mathbf{c}, \mathbf{b}, 2\mathbf{a} - \mathbf{c}$ leads to a $3a \times b \times 3c$ X-centered monoclinic supercell with centering vectors $(\frac{1}{3}, 0, \frac{1}{3})$ and $(\frac{2}{3}, 0, \frac{2}{3})$. On decompression, at $P = 47.5$ GPa only the lock-in phase survived. It was described by the same superspace group and the same basic structure as the incommensurately modulated structure at

116

lower pressures. Refinements of the commensurately modulated structure converged smoothly to a good fit to the diffraction data (Table A.2). The best fit to the diffraction data was obtained for the section $t_0 = \frac{1}{12}$ of superspace (Table A.6). This structure model corresponds to a superstructure with a sixfold, $3a \times b \times 2c$ supercell with space group $Pmmn$.

Table A.1: Experimental details on compression of CrOCl at ID09A (ESRF).

	0.0001 GPa	2.05 GPa	3.25 GPa
Crystal data			
$a(\text{Å})$	3.8683(1)	3.8461(1)	3.8382(1)
$b(\text{Å})$	3.1823(4)	3.1618(1)	3.1530(1)
$c(\text{Å})$	7.726(8)	7.3924(17)	7.2652(19)
$V(\text{Å}^3)$	95.14(7)	89.90(2)	87.92(2)
Data collection			
No. of reflections:			
measured,	164	196	190
independent,	51	62	63
observed ($I > 3\sigma(I)$)	51	59	61
R_{int} (obs/all)	0.0441/0.0441	0.0288/0.0288	0.0310/0.0310
Redundancy	3.216	3.161	3.016
$(\sin\theta/\lambda)_{max}(\text{Å}^{-1})$	0.764	0.783	0.785
Refinement			
No. of parameters	10	10	10
$R_F(\text{obs})/wR_F(\text{all})$	0.0423/0.0569	0.0272/0.0438	0.0242/0.0390
$\Delta\rho_{min}/\Delta\rho_{max}(\text{eÅ}^{-3})$	-0.57/0.59	-0.36/0.27	-0.36/0.39

Table A.1 – continued from previous page

	5.20 GPa	7.10 GPa	9.05 GPa
Crystal data			
$a(\text{Å})$	3.8272(1)	3.8190(1)	3.8083(1)
$b(\text{Å})$	3.1403(1)	3.1299(1)	3.1170(1)
$c(\text{Å})$	7.1203(19)	6.9996(17)	6.889(2)
$V(\text{Å}^3)$	85.58(2)	83.67(2)	81.78(2)
Data collection			
No. of reflections:			
measured,	182	166	192
independent,	60	58	61
observed $(I > 3\sigma(I))$	52	56	46
R_{int} (obs/all)	0.0322/0.0323	0.0361/0.0361	0.0523/0.0525
Redundancy	3.033	2.862	3.148
$(\sin\theta/\lambda)_{max}(\text{Å}^{-1})$	0.787	0.789	0.787
Refinement			
No. of parameters	10	10	9
$R_F(\text{obs})/wR_F(\text{all})$	0.0286/0.0374	0.0344/0.0552	0.0327/0.0418
$\Delta\rho_{min}/\Delta\rho_{max}(\text{eÅ}^{-3})$	-0.42/0.50	-0.33/0.46	-0.74/0.74

Table A.1 – continued from previous page

	10.45 GPa	12.95 GPa
Crystal data		
$a(\text{Å})$	3.8024(1)	3.7978(2)
$b(\text{Å})$	3.1088(1)	3.1009(2)
$c(\text{Å})$	6.811(2)	6.703(6)
$V(\text{Å}^3)$	80.51(2)	78.94(7)
Data collection		
No. of reflections:		
measured,	188	158
independent,	61	56
observed $(I > 3\sigma(I))$	50	47
R_{int} (obs/all)	0.0437/0.0438	0.0250/0.0250
Redundancy	3.082	2.821
$(\sin\theta/\lambda)_{max}(\text{Å}^{-1})$	0.729	0.732
Refinement		
No. of parameters	9	9
$R_F(\text{obs})/wR_F(\text{all})$	0.0395/0.0459	0.0425/0.0619
$\Delta\rho_{min}/\Delta\rho_{max}(\text{e}\text{Å}^{-3})$	-0.5/1.0	-0.55/1.04

Table A.1 – continued from previous page

	16.4 GPa	23.3 GPa	30.3 GPa
Crystal data			
a (Å)	3.7866(3)	3.7698(5)	3.7406(12)
b (Å)	3.0848(3)	3.0669(5)	3.0156(18)
c (Å)	6.564(6)	6.286(8)	6.19(3)
V (Å^3)	76.67(7)	72.68(11)	69.8(3)
q-vector	$(0.2869(5),0,\frac{1}{2})$	$(0.2835(3),0,\frac{1}{2})$	$(0.2877(6),0,\frac{1}{2})$
Data collection			
No. of reflections:			
measured (main/sat1/sat2)[1]	165/393/0	140/331/253	145/358/305
independent (main/sat1/sat2)	55/106/0	44/96/91	48/101/94
observed (main/sat1/sat2)	46/63/0	39/65/50	43/61/49
R_{int} (obs/all)	0.0519/0.0523	0.0665/0.0674	0.0560/0.0577
Redundancy	3.466	3.134	3.325
$(\sin\theta/\lambda)_{max}(Å^{-1})$	0.778	0.784	0.790
Refinement			
No. of parameters	17	23	23
R_F(obs) (all/main)	0.0420/0.0400	0.0408/0.0369	0.0604/0.0529
R_F(obs) (sat1/sat2)	0.0486/–	0.0445/0.0431	0.0638/0.0754
wR_F(all) (all/main)	0.0541/0.0524	0.0552/0.0455	0.0734/0.0637
wR_F(all) (sat1/sat2)	0.0612/–	0.0617/0.0771	0.0785/0.1119
$\Delta\rho_{min}/\Delta\rho_{max}(eÅ^{-3})$	-0.71/0.75	-0.57/0.51	-0.99/0.79

---

[1]Here and in the following tables notation sat$n$ corresponds to nth-order satellites.

Table A.1 – continued from previous page

	40.4 GPa	45.3 GPa	51.0 GPa
Crystal data			
a (Å)	3.7323(6)	3.7348(11)	3.726(3)
b (Å)	2.9902(6)	2.9702(18)	2.9574(20)
c (Å)	5.967(7)	5.86(3)	5.87(5)
$V(\text{Å}^3)$	66.59(8)	65.0(3)	64.5
q-vector	$(0.2967(4),0,\frac{1}{2})$	$(0.3015(5),0,\frac{1}{2})$	$(0.3120(4),0,\frac{1}{2})$
Data collection			
No. of reflections:			
measured (main/sat1/sat2)	136/304/238	136/338/287	134/276/256
independent (main/sat1/sat2)	43/90/86	49/92/89	38/81/81
observed (main/sat1/sat2)	36/54/44	39/46/39	34/50/44
R_{int} (obs/all)	0.0558/0.0573	0.0573/0.0593	0.0458/0.0467
Redundancy	3.178	3.309	3.330
$(\sin\theta/\lambda)_{max}(\text{Å}^{-1})$	0.762	0.774	0.792
Refinement			
No. of parameters	23	23	23
R_F(obs) (all/main)	0.0582/0.0436	0.0575/0.0534	0.0504/0.0373
R_F(obs) (sat1/sat2)	0.0670/0.0855	0.0528/0.0845	0.0496/0.1022
wR_F(all) (all/main)	0.0686/0.0493	0.0723/0.0637	0.0563/0.0402
wR_F(all) (sat1/sat2)	0.0855/0.1267	0.0766/0.1334	0.0606/0.1467
$\Delta\rho_{min}/\Delta\rho_{max}(\text{e\AA}^{-3})$	-0.86/0.87	-0.85/1.07	-1.01/0.81

Table A.2: Experimental details on decompression of CrOCl at P02.2 (DESY).

	47.5 GPa	40.5 GPa	28.0 GPa
Crystal data			
a (Å)	3.707(3)	3.7404(8)	3.772(2)
b (Å)	2.943(3)	3.0133(8)	3.050(2)
c (Å)	5.91(4)	5.93(1)	6.17(3)
$V(Å^3)$	64.5(4)	66.88(12)	71.0(4)
q-vector	$(\frac{1}{3},0,\frac{1}{2})$	$(0.3022(3),0,\frac{1}{2})$	$(0.2867(2),0,\frac{1}{2})$
Data collection			
No. of reflections:			
measured (main/sat1/sat2)	296/640/603	291/653/613	277/655/639
independent (main/sat1/sat2)	74/145/144	78/153/149	77/159/161
observed (main/sat1/sat2)	70/85/86	72/94/87	67/97/81
R_{int} (obs/all)	0.0463/0.0514	0.0417/0.0467	0.0340/0.0423
Redundancy	4.240	4.097	3.957
$(\sin\theta/\lambda)_{max}(Å^{-1})$	0.986	0.977	0.950
Refinement			
No. of parameters	23	23	23
R_F(obs) (all/main)	0.0280/0.0213	0.0263/0.0242	0.0306/0.0245
R_F(obs) (sat1/sat2)	0.0296/0.0414	0.0234/0.0365	0.0356/0.0384
wR_F(all) (all/main)	0.0403/0.0235	0.0360/0.0268	0.0410/0.0260
wR_F(all) (sat1/sat2)	0.0503/0.0735	0.0349/0.0717	0.0553/0.0701
$\Delta\rho_{min}/\Delta\rho_{max}(eÅ^{-3})$	-0.71/0.73	-0.63/0.49	-0.63/0.58

Table A.2 – continued from previous page

	18.5 GPa	14.5 GPa	5.5 GPa
Crystal data			
a (Å)	3.8127(8)	3.8123(13)	3.8268(2)
b (Å)	3.1086(9)	3.1109(11)	3.1429(2)
c (Å)	6.379(11)	6.65(2)	7.212(3)
$V(\text{Å}^3)$	75.61(14)	78.9(3)	86.74(4)
q-vector	$(0.2836(2),0,\frac{1}{2})$	—	—
Data collection			
No. of reflections:			
measured (main/sat1/sat2)	312/743/704	359/–/–	436/–/–
independent (main/sat1/sat2)	90/171/170	94/–/–	85/–/–
observed (main/sat1/sat2)	76/92/52	64/–/–	74/–/–
R_{int}(obs/all)	0.0386/0.0522	0.0266/0.0308	0.0260/0.0272
Redundancy	4.081	3.819	5.129
$(\sin\theta/\lambda)_{max}(\text{Å}^{-1})$	0.963	0.971	0.953
Refinement			
No. of parameters	23	14	14
R_F(obs) (all/main)	0.0224/0.0179	0.0263/0.0263	0.0165/0.0165
R_F(obs) (sat1/sat2)	0.0237/0.0424	–/–	–/–
wR_F(all) (all/main)	0.0406/0.0215	0.0287/0.0287	0.0209/0.0209
wR_F(all) (sat1/sat2)	0.0521/0.1208	–/–	–/–
$\Delta\rho_{min}/\Delta\rho_{max}(\text{eÅ}^{-3})$	-0.54/0.51	-0.47/0.50	-0.37/0.39

Table A.2 – continued from previous page

	0.0001 GPa
Crystal data	
a (Å)	3.8601(3)
b (Å)	3.1771(3)
c (Å)	7.708(5)
$V(\text{Å}^3)$	94.53(6)
Data collection	
No. of reflections:	
measured	456
independent	91
observed	78
R_{int}(obs/all)	0.0675/0.0691
Redundancy	5.011
$(\sin\theta/\lambda)_{max}(\text{Å}^{-1})$	0.940
Refinement	
No. of parameters	14
R_F(obs)/wR_F(all)	0.0302/0.0370
$\Delta\rho_{min}/\Delta\rho_{max}(\text{eÅ}^{-3}$	-0.62/0.73

Table A.3: R factors of refinements of the high-pressure phase of CrOCl between 16.4 and 30.3 GPa using different models.[1]

	16.4 GPa	23.3 GPa	30.3 GPa	28.0 GPa	18.5 GPa
Incommensurate:					
R_F (all)	0.0420	0.0481	0.0605	0.0306	0.0224
R_F (main)	0.0400	0.0411	0.0529	0.0245	0.0179
R_F (sat1)	0.0485	0.0532	0.0641	0.0356	0.0237
R_F (sat2)	—	0.0649	0.0751	0.0384	0.0424
Commensurate:					
$\mathbf{t_0 = 0}$					
R_F (all)	0.0420	0.0481	0.0606	0.0306	0.0223
R_F (main)	0.0400	0.0411	0.0527	0.0245	0.0172
R_F (sat1)	0.0487	0.0532	0.0643	0.0357	0.0237
R_F (sat2)	—	0.0648	0.0762	0.0384	0.0422
Commensurate:					
$\mathbf{t_0 = \frac{1}{28}}$					
R_F (all)	0.0420	0.0481	0.0606	0.0305	0.0223
R_F (main)	0.0400	0.0411	0.0527	0.0245	0.0172
R_F (sat1)	0.0487	0.0531	0.0642	0.0357	0.0237
R_F (sat2)	—	0.0649	0.0762	0.0383	0.0422
Commensurate:					
$\mathbf{t_0 = 0.050508}$					
R_F (all)	0.0420	0.0481	0.0606	0.0305	0.0223
R_F (main)	0.0400	0.0411	0.0527	0.0245	0.0172
R_F (sat1)	0.0487	0.0531	0.0643	0.0357	0.0237
R_F (sat2)	—	0.0649	0.0762	0.0383	0.0422

[1] Reflections were averaged according to point symmetry $2mm$ for all refinements.

Table A.4: Experimental details on structure refinement of FeOCl at 15 GPa.

Crystal data	
a (Å)	3.6615(11)
b (Å)	3.1937(11)
c (Å)	6.780(13)
$V(\text{Å}^3)$	79.29(16)
q-vector	$(0.261, 0, \frac{1}{2})$
Space group	$Pmmn(\sigma_1 0\frac{1}{2})00s$
Data collection	
No. of reflections:	
measured (main/sat)	252/503
independent (main/sat)	61/121
observed (main/sat)	50/52
Redundancy	4.148
$(\sin\theta/\lambda)_{max}(\text{Å}^{-1})$	0.719
R_{int}(obs/all)	0.0571/0.0615
Refinement	
No. of parameters	21
R_F(obs) (all/main/sat)	0.0550/0.0549/0.0555
wR_F(all) (all/main/sat)	0.0677/0.0626/0.0906
$\Delta\rho_{min}/\Delta\rho_{max}(\text{e\AA}^{-3})$	-1.16/0.85

Table A.5: Crystal data on CrOCl high-pressure phases observed at 57.2 GPa.

	$3a \times b \times 2c$	$3a \times b \times 3c$
Crystal data		
a (Å)	3.6788(13)	6.910(16)
b (Å)	2.8999(9)	2.8950(9)
c (Å)	5.812(18)	9.325(9)
β (°)	90	95.86(18)
V(Å^3)	62.0(2)	185.6(5)
q-vector	$(\frac{1}{3},0,\frac{1}{2})$	–
Space group	$Pmmn(\sigma_1 0\frac{1}{2})00s$	$P2_1/m$
Data collection		
No. of reflections:		
measured (main/sat1/sat2/sat3)	288/807/744/412	1131/–/–/–
independent (main/sat1/sat2/sat3)	94/199/194/104	538/–/–/–
observed (main/sat1/sat2/sat3)	65/68/65/9	247/–/–
Redundancy	3.814	2.102
$(\sin\theta/\lambda)_{max}$(Å^{-1})	1.086	1.093
R$_{int}$(obs/all)	22.17/26.98	17.96/19.85
Refinement		
No. of parameters	23	28
R$_F$(obs) (all/main)	0.0882/0.0905	0.0807/0.0807
R$_F$(obs) (sat1/sat2/sat3)	0.0955/0.0711/0.0891	–/–/–
wR$_F$(all) (all/main)	0.1333/0.0.1114	0.1153/0.1153
wR$_F$(all) (sat1/sat2/sat3)	0.1397/0.1463/0.3552	–/–/–
$\Delta\rho_{min}/\Delta\rho_{max}$(eÅ^{-3})	-2.79/3.21	-1.95/1.83

Table A.6: R factors of refinements of the high-pressure lock-in phase of CrOCl at 47.5 GPa on decompession using different models.[1]

	$t_0 = 0$,	$t_0 = \frac{1}{12}$	$t_0 = $ general	Incommensurate
Supercell space group	$Pcmn$	$Pmmn$	$P2_1mn$	—
R_{all} $(I > 3\sigma(I))$	0.0981	0.0279	0.0344	0.0491
R_{main} $(I > 3\sigma(I))$	0.0316	0.0212	0.0216	0.0260
R_{sat1} $(I > 3\sigma(I))$	0.0889	0.0297	0.0322	0.0461
R_{sat2} $(I > 3\sigma(I))$	0.2658	0.0414	0.0674	0.1071
wR_{all}	0.1191	0.0402	0.0467	0.0610
wR_{main}	0.0337	0.0233	0.0234	0.0278
wR_{sat1}	0.1117	0.0503	0.0532	0.0645
wR_{sat2}	0.2984	0.0734	0.0979	0.1370

[1] Reflections were averaged according to point symmetry $2mm$ for all refinements.

A.3 Pressure dependence of the Raman scattering of CrOCl

Raman spectra of CrOCl were recorded at 13 pressure points within the range 5–31 GPa (Fig. A.1). The full representation of the vibrational modes of CrOCl in space group $Pmmn$ is:

$$\Gamma_{tot} = 3A_g + 2B_{1u} + 3B_{2g} + 2B_{2u} + 3B_{3g} + 2B_{3u}, \tag{A.1}$$

where A_g, B_{2g} and B_{3g} are Raman active. At low pressures three strong Raman
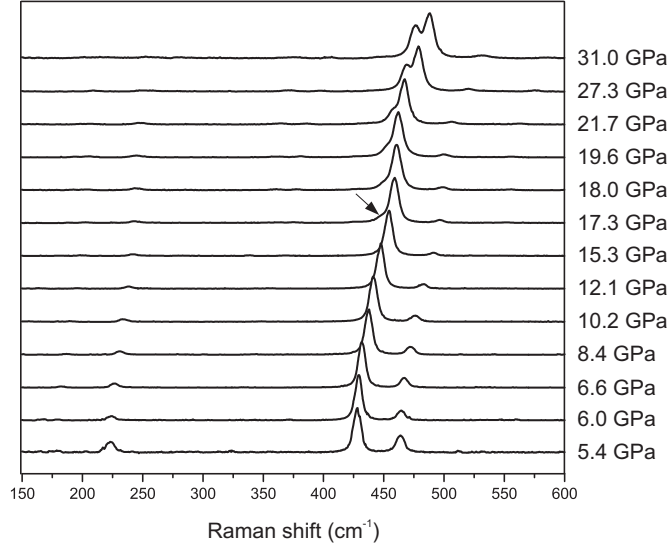
Figure A.1: Raman spectra of CrOCl at different pressures. The arrow points at the strongest additional peak appearing in the course of the phase transition.

active modes are clearly observed (Fig A.1). They can be identified with A_g modes according to Fausti et al. [109]. The three additional weakly active modes may have either B_{2g} or B_{3g} symmetry. All Raman peaks gradually shift to higher energies with pressure (Fig. A.2). Dramatic changes in Raman spectrum are observed in the pressure region between 15.3 and 17.3 GPa, thus manifesting a phase transition.
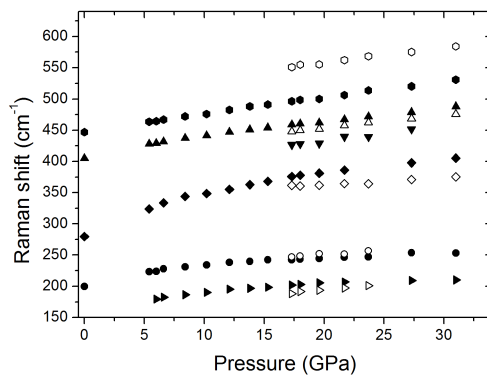
Figure A.2: Variation of the Raman shift frequencies with applied pressure.
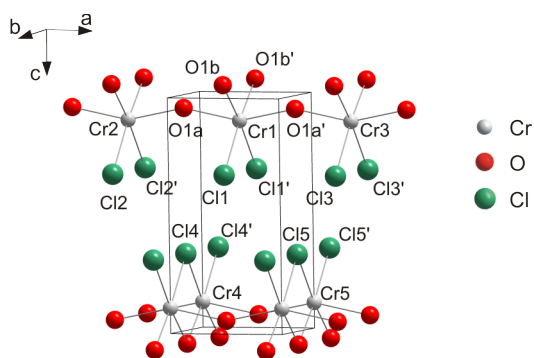
Figure A.3: Average structure of CrOCl. Atomic labeling as used in the Fig. A.4 and in the Table A.8 is shown.

A.4   *t*-plots of the incommensurately modulated structure of CrOCl at 23 GPa
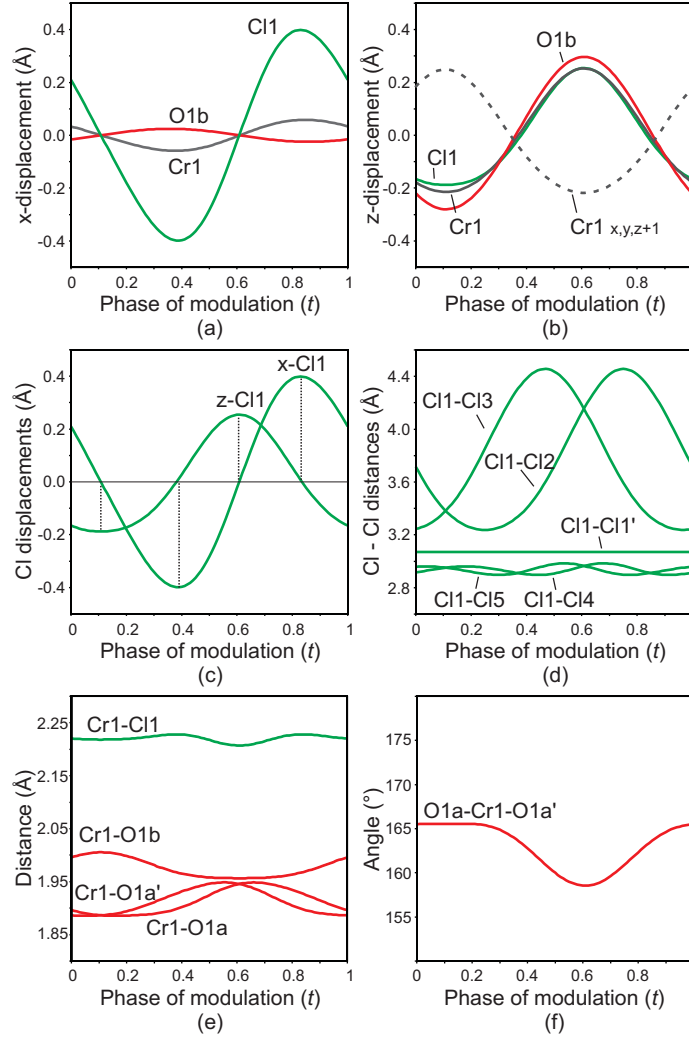
Figure A.4:   Selected *t*-plots of the incommensurately modulated structure of CrOCl at $P = 23.3$ GPa. (a) *x*-displacements of Cr, O and Cl atoms. (b) *z*-displacements of Cr, O, Cl atoms. (c) *x*- and *z*-displacements of Cl atom; vertical dashed lines are drawn at *t* values corresponding to maximal and minimal displacements. (d) Cl···Cl distances. (e) Cr-O and Cr-Cl distances. (f) O-Cr-O angle.

A.5 Tables of interatomic distances and angles

Table A.7: Average interlayer Cl$\cdots$Cl distances (Å) in CrOCl and in FeOCl.

Pressure, GPa	FeOCl	CrOCl
0.0001	3.680(6)[1]	3.678(8)
15.0	3.06(3)	
16.4		3.007(9)
22.7	2.92(3)[2]	
23.3		2.924(8)

[1] Data from [111].
[2] Data from [127].

Table A.8: Selected interatomic distances for CrOCl. For pressures above 15 GPa distances have been averaged over the phase t of the modulation.

Pressure (GPa)	Cr1-O1a (Å)	Cr1-O1b (Å)	Cr1-Cl1 (Å)
0.0001	1.976(4)	2.036(12)	2.316(7)
2.05	1.969(3)	2.012(8)	2.301(5)
3.25	1.956(2)	2.023(8)	2.302(4)
5.20	1.955(3)	2.009(10)	2.281(5)
7.10	1.946(3)	2.013(9)	2.274(4)
9.05	1.941(3)	2.009(11)	2.258(5)
10.45	1.934(3)	2.002(12)	2.262(6)
12.95	1.933(5)	1.988(15)	2.246(7)
16.4	1.921(12)	1.993(11)	2.241(6)
23.3	1.912(5)	1.976(15)	2.220(8)
30.3	1.90(5)	1.95(2)	2.194(12)
40.4	1.886(15)	1.95(2)	2.173(13)
45.3	1.89(5)	1.94(3)	2.140(15)
51.0	1.88(8)	1.95(2)	2.164(11)
	Cl1$\cdots$Cl2 (Å)	Cl1$\cdots$Cl1′ (Å)	Cl1$\cdots$Cl4 (Å)
0.0001	3.8683(1)	3.1823(4)	3.676(8)
2.05	3.8461(1)	3.1618(1)	3.446(6)
3.25	3.8382(1)	3.1530(1)	3.360(5)
5.20	3.8272(1)	3.1403(1)	3.284(6)
7.10	3.8190(1)	3.1299(1)	3.216(5)
9.05	3.8083(1)	3.1170(1)	3.156(6)
10.45	3.8024(1)	3.1088(1)	3.110(6)
12.95	3.7978(2)	3.1009(2)	3.069(7)
16.4	3.79(2)	3.0848(3)	3.007(9)
23.3	3.78(3)	3.0669(5)	2.923(12)
30.3	3.75(1)	3.0156(18)	2.88(4)
40.4	3.74(2)	2.9902(6)	2.800(14)
45.3	3.75(9)	2.9702(18)	2.79(4)
51.0	3.74(16)	2.9574(20)	2.74(6)

Appendix B

High-pressure behavior of MOCl (M = Sc, Ti, V)

Relations between TiOCl-II and the low-temperature incommensurate phase

Schönleber et al. have reported the structure model for the incommensurate phase of TiOCl, stable between 66 and 90 K [37]. It was found that the structure has $P2/n(\sigma_1, \sigma_2, 0)00$ symmetry with $\sigma_1 = 0.0589$ and $\sigma_2 = 0.5066$ at 72 K. Furthermore, the structure appeared to be twinned. Therefore, the first order satellite reflections belonging to different domains appear very close to each other. Consequently, it is not possible to distinguish, to which domain the observed satellite belongs to. This brings an ambiguity to the assessment of the correct superspace group. In particular, the reflection (0001) should be extinct in $P2/n(\sigma_1, \sigma_2, 0)0s$. Nevertheless, it overlaps with the reflection $(010\bar{1})$ of the second domain. The latter reflection is not extinct in $P2/n(\sigma_1, \sigma_2, 0)0s$. The situation is opposite if we consider the superspace group $P2/n(\sigma_1, \sigma_2, 0)00$. So, in this case, both superspace groups do not contradict the observed diffraction patterns. In case of TiOCl-II at high pressure, the structure is not twinned and it was possible to unambiguously determine the correct superspace group as $P2/n(\sigma_1, \sigma_2, 0)0s$ which differs from that reported by Schönleber et al. [37]. We have reproduced the refinement of the incommensurate low-temperature structure of TiOCl using the data, kindly provided by the authors of [37]. It has been found that the refinement in the superspace group $P2/n(\sigma_1, \sigma_2, 0)0s$ leads to lower R-values than the refinement in $P2/n(\sigma_1, \sigma_2, 0)00$ (Table B.1). Therefore, we suggest that the symmetries of TiOCl-II and the low-temperature incommensurate structure of TiOCl are the same. The structure models of TiOCl-II at 10.2, 11.8 GPa and at 72 K are compared in the Table B.2.

Table B.1: Results of the refinements of the low-temperature incommensurate structure of TiOCl, using the data provided by the authors of [37].

	$P2/n(\sigma_1, \sigma_2, 0)00$	$P2/n(\sigma_1, \sigma_2, 0)0s$
R_F (obs)(main + satellite)	0.0441	0.0438
R_F (obs)(main)	0.0394	0.0395
R_F (obs)(satellite)	0.0991	0.0947

Table B.2: Comparison of the structure of TiOCl-II at different conditions. Given are the fractional atomic coordinates and non-zero atomic modulation amplitudes (see Eq. 7.1).

	10.2 GPa, 293 K	11.8 GPa, 293 K	1 bar, 72 K
$x[\text{Ti}]/a$	0	0	0
$y[\text{Ti}]/b$	0.5	0.5	0.5
$z[\text{Ti}]/c$	0.1323(5)	0.1334(3)	0.11976(8)
$B_x[\text{Ti}]$, Å	0.0264(12)	0.0299(10)	0.0097(19)
$B_y[\text{Ti}]$, Å	0.1129(13)	0.1307(14)	0.0479(14)
$A_z[\text{Ti}]$, Å	-0.036(5)	-0.042(4)	-0.017(3)
$x[\text{O}]/a$	0	0	0
$y[\text{O}]/b$	0	0	0
$z[\text{O}]/c$	-0.0698(16)	-0.0718(15)	-0.0563(3)
$B_x[\text{O}]$, Å	-0.009(5)	-0.015(4)	-0.015(8)
$B_y[\text{O}]$, Å	-0.069(5)	-0.075(5)	-0.032(7)
$A_z[\text{O}]$, Å	-0.076(17)	-0.084(14)	-0.027(7)
$x[\text{Cl}]/a$	0	0	0
$y[\text{Cl}]/b$	0	0	0
$z[\text{Cl}]/c$	0.3618(7)	0.3667(5)	0.33369(12)
$B_x[\text{Cl}]$, Å	0.0035(19)	0.0046(15)	-0.001(4)
$B_y[\text{Cl}]$, Å	0.0320(16)	0.0387(16)	0.0151(2)
$A_z[\text{Cl}]$, Å	0.062(7)	0.082(6)	0.056(3)

Appendix B. Appendix high-pressure behavior of MOCl (M = Sc, Ti, V)

Table B.3: Experimental details on compression of TiOCl.

	0.2 GPa	3.7 GPa
Crystal data		
a(Å)	3.7952(3)	3.7653(1)
b(Å)	3.3717(3)	3.2880(1)
c(Å)	8.054(6)	7.621(3)
V(Å^3)	103.06(8)	94.35(4)
Space group	$Pmmn$	$Pmmn$
Data collection		
No. of reflections:		
measured,	205	198
independent,	88	76
observed $(I > 3\sigma(I))$	55	55
R$_{int}$ (obs/all)	0.0679/0.0705	0.0600/0.0602
Redundancy	2.33	2.605
$(\sin\theta/\lambda)_{max}$(Å^{-1})	0.793	0.781
Refinement		
No. of parameters	11	11
R$_F$(obs),wR$_F$(all)	0.0639/0.0685	0.0310/0.0409
$\Delta\rho_{min}/\Delta\rho_{max}$(eÅ^{-3})	-0.75/0.84	-0.36/0.49

Table B.3: continued from previous page

	10.2 GPa	11.8 GPa
Crystal data		
a (Å)	3.7447(3)	3.740(6)
b (Å)	3.183(4)	3.157(6)
c (Å)	7.326(8)	7.298(14)
$\gamma(°)$	90.0	90.0
V (Å³)	87.30(17)	86.17(30)
Superspace group	$P2/n(\sigma_1,\sigma_2,0)0s$	$P2/n(\sigma_1,\sigma_2,0)0s$
q-vector	(0.1016(15),0.5109(16),0)	(0.1016(16),0.5052(16),0)
Data collection		
No. of reflections:		
measured (main/sat1)[1]	183/361	190/361
independent (main/sat1)	87/168	89/166
observed (main/sat1)	67/84	76/135
R_{int} (obs/all)	0.0324/0.0333	0.0177/0.0178
Redundancy	2.133	2.161
$(\sin\theta/\lambda)_{max}$(Å⁻¹)	0.799	0.817
Refinement		
No. of parameters	25	25
R_F(obs) (all/main/sat)	0.0417/0.0322/0.0670	0.0539/0.0385/0.0856
wR_F(all) (all/main/sat)	0.0538/0.0364/0.1196	0.0646/0.0451/0.1060
$\Delta\rho_{min}/\Delta\rho_{max}$(eÅ⁻³)	-0.43/0.45	-0.54/0.66

---

[1]Here and in the following tables notation sat$n$ corresponds to n^{th}-order satellites.

Table B.3: continued from previous page

	15.0 GPa	18.1 GPa
Crystal data		
a (Å)	3.7316(4)	3.729(3)
b (Å)	3.1230(4)	3.106(2)
c (Å)	7.191(9)	6.989(12)
$\gamma(°)$	90.0	90.0
$V(\text{Å}^3)$	83.81(10)	80.95(10)
$\mathbf{q}^1$	$(0.1242(12), \frac{1}{2}, 0)$	$(0.1179(6), \frac{1}{2}, 0)$
$\mathbf{q}^2$	$(0.2494(12), 0, \frac{1}{2})$	$(0.2364(4), 0, \frac{1}{2})$
Superspace group	$P2/n(\sigma_{11}, \sigma_{12}, 0)0s(\sigma_{21}, \sigma_{22}, \frac{1}{2})0s$	$P2/n(\sigma_{11}, \sigma_{12}, 0)0s(\sigma_{21}, \sigma_{22}, \frac{1}{2})0s$
Data collection		
No. of reflections:		
Main reflections:		
measured	199	168
independent	93	81
observed	59	64
$\mathbf{q}^1$ satellites:		
measured (1st order)	399	373
independent (1st order)	212	186
observed (1st order)	66	102
$\mathbf{q}^2$ satellites:		
measured (1st order)	432	365
measured (2nd order)	–	323
measured (3rd order)	–	278
independent (1st order)	185	169
independent (2nd order)	–	152
independent (3rd order)	–	150
observed (1st order)	19	101
observed (2nd order)	–	75
observed (3rd order)	–	31
R_{int} (obs/all)	0.0835/0.0921	0.0786/0.0844
Redundancy	2.196	1.917
$(\sin\theta/\lambda)_{max}(\text{Å}^{-1})$	0.833	0.821

Table B.3: continued from previous page

	15.0 GPa	18.1 GPa
Refinement		
No. of parameters	26	50
$R_F(\text{obs})/wR_F(\text{all})$	0.0932/0.1234	0.0627/0.0793
R-values for main reflections:		
$R_F(\text{obs})/wR_F(\text{all})$	0.0835/0.1006	0.0518/0.0599
R-values for $\mathbf{q}^1$ satellites:		
$R_F(\text{obs})/wR_F(\text{all})$	0.1065/0.1969	0.0952/0.1294
R-values for $\mathbf{q}^2$ satellites:		
$R_F(\text{obs})/wR_F(\text{all})$ (1st order)	0.1628/0.3014	0.0544/0.0785
$R_F(\text{obs})/wR_F(\text{all})$ (2nd order)	–/–	0.0593/0.0884
$R_F(\text{obs})/wR_F(\text{all})$ (3rd order)	–/–	0.0755/0.1438
$\Delta\rho_{min}/\Delta\rho_{max}(\text{e\AA}^{-3})$	-1.36/1.13	-0.93/0.96

Table B.4: Structural parameters for the TiOCl-III phase at 18.1 GPa. coordinates are given with respect to the average unit cell. Modulation amplitudes are recalculated in Å.

	Ti	O	Cl
x/a	0	0	0
y/b	0.5	0	0
z/c	0.1371(5)	-0.0763(16)	0.3767(6)
U^{eq} (Å^2)	0.011(2)	0.0078(9)	0.012(2)
A_x^{10}	0	0	0
B_x^{10}	0.0273(18)	-0.018(7)	0.0002(6)
A_y^{10}	0	0	0
B_y^{10}	0.1362(15)	-0.063(5)	0.042(2)
A_z^{10}	-0.031(7)	-0.075(29)	0.069(17)
B_z^{10}	0	0	0
A_x^{01}	0.0276(5)	0.0081(11)	0.4549(19)
B_x^{01}	0.0600(5)	-0.033(3)	0.1856(9)
A_y^{01}	0.0006(11)	0.0004(20)	0.002(3)
B_y^{01}	0.0013(11)	-0.0016(20)	0.0006(10)
A_z^{01}	-0.247(4)	-0.329(16)	-0.106(3)
B_z^{01}	0.113(4)	-0.081(4)	0.260(6)
A_x^{02}	0.0005(8)	0.001(4)	0.0587(15)
B_x^{02}	-0.0006(8)	0.0007(20)	0.0574(14)
A_y^{02}	-0.0035(19)	-0.011(11)	0.0002(20)
B_y^{02}	0.0041(19)	-0.005(5)	0.0002(20)
A_z^{02}	-0.008(4)	-0.008(8)	-0.026(5)
B_z^{02}	-0.007(4)	0.016(16)	0.026(5)
A_x^{03}	0.0016(8)	-0.005(3)	-0.0037(9)
B_x^{03}	0.0004(2)	0.006(3)	-0.0085(9)
A_y^{03}	-0.002(4)	-0.010(8)	0.0036(19)
B_y^{03}	-0.0004(4)	0.012(8)	0.008(4)
A_z^{03}	-0.0043(15)	-0.005(15)	0
B_z^{03}	0.015(5)	-0.004(13)	0

Table B.5: Experimental details on VOCl. Pressure points on decompression are indicated with asterisk.

	0.0001 GPa*	4.3 GPa*	8.4 GPa
Crystal data			
$a(\text{Å})$	3.7741(2)	3.7502(2)	3.7287(2)
$b(\text{Å})$	3.3012(2)	3.2635(2)	3.2268(2)
$c(\text{Å})$	7.937(6)	7.412(6)	7.1435(37)
$V(\text{Å}^3)$	98.90(7)	90.71(7)	85.94(4)
Space group	$Pmmn$	$Pmmn$	$Pmmn$
Data collection			
No. of reflections:			
measured,	203	210	206
independent,	64	60	65
observed $(I > 3\sigma(I))$	56	53	56
R_{int} (obs/all)	0.0248/0.0249	0.0581/0.0582	0.0579/0.0579
Redundancy	3.172	3.5	3.169
$(\sin\theta/\lambda)_{max}(\text{Å}^{-1})$	0.749	0.759	0.768
Refinement			
No. of parameters	7	7	9
$R_F(\text{obs}),wR_F(\text{all})$	0.1018/0.1404	0.0952/0.1501	0.0590/0.0859
$\Delta\rho_{min}/\Delta\rho_{max}(\text{e\AA}^{-3})$	-1.32/1.43		-0.97/1.07

Table B.5: continued from previous page

	9.72 GPa	11.85 GPa	13.4 GPa*
Crystal data			
$a(\text{Å})$	3.7269(3)	3.7184(4)	3.7329(5)
$b(\text{Å})$	3.2196(3)	3.2017(3)	3.1958(4)
$c(\text{Å})$	7.080(7)	6.994(8)	6.899(13)
$V(\text{Å}^3)$	84.95(9)	83.27(10)	82.30(16)
Space group	$Pmmn$	$Pmmn$	$Pmmn$
Data collection			
No. of reflections:			
measured,	207	189	169
independent,	64	63	61
observed $(I > 3\sigma(I))$	59	58	52
R_{int} (obs/all)	0.0244/0.0244	0.0299/0.0300	0.0496/0.0497
Redundancy	3.234	3.0	2.77
$(\sin\theta/\lambda)_{max}(\text{Å}^{-1})$	0.770	0.774	0.745
Refinement			
No. of parameters	7	7	7
R_F(obs),wR_F(all)	0.0837/0.1211	0.0804/0.1244	0.0773/0.1041
$\Delta\rho_{min}/\Delta\rho_{max}(\text{e}\text{Å}^{-3})$	-1.3/1.58	1.19/-1.43	-1.3/1.43

	14.1 GPa	16.3 GPa	16.8 GPa*
a (Å)	3.7154(3)	3.7218(5)	3.7394(2)
b (Å)	3.1855(3)	3.1764(5)	3.1654(2)
c (Å)	6.893(6)	6.735(8)	6.671(7)
V (Å^3)	81.58(7)	79.62(11)	79.0(1)
(super)space group	$Pmmn$	$Pmmn(\sigma_1,0,\frac{1}{2})00s$	$Pmmn(\sigma_1,0,\frac{1}{2})00s$
q-vector	—	$(0.2618(1),0,\frac{1}{2})$	$(0.2617(3),0,\frac{1}{2})$
Data collection			
No. of reflections:			
measured (main/sat1)	200/–	639/1476	174/401
measured (sat2/sat3)	–/–	1308/741	357/420
independent (main/sat1)	61/–	70/125	58/113
independent (sat2/sat3)	–/–	122/124	111/113
observed (main/sat1)	58/–	67/99	55/85
observed (sat2/sat3)	–/–	84/42	75/30
R_{int} (obs/all)	0.0519/0.0523	0.1160/0.1164	0.0864/0.0871
Redundancy	3.279	9.522	3.428
$(\sin\theta/\lambda)_{max}$(Å^{-1})	0.778	0.782	0.764
Refinement			
No. of parameters	7	44	41
R_F(obs) (all/main)	0.0646/0.0646	0.0433/0.0412	0.0900/0.0818
R_F(obs) (sat1/sat2/sat3)	–/–/–	0.0365/0.0556/0.0805	0.0912/0.1114/0.1020
wR_F(all) (all/main)	0.1138/0.1138	0.0480/0.0484	0.1056/0.0964
wR_F(all) (sat1/sat2/sat3)	–/–/–	0.0415/0.0549/0.0991	0.1016/0.1449/0.1617
$\Delta\rho_{min}/\Delta\rho_{max}$(eÅ^{-3})	-1.281/1.03	-0.72/0.83	-1.42/1.16

Table B.5: continued from previous page

	20.3 GPa*	23.7 GPa	24.7 GPa
Crystal data			
$a(\text{Å})$	11.1744(8)	11.0813(8)	11.0496(4)
$b(\text{Å})$	9.0919(6)	9.0709(6)	8.9893(3)
$c(\text{Å})$	12.813(9)	12.678(9)	12.716(5)
$V(\text{Å}^3)$	1301.8(4)	1274.3(9)	1263.0(5)
$\alpha(°)$	90.0	90.0	90.0
Space group	$P2_1/c$	$P2_1/c$	$P2_1/c$
Data collection			
No. of reflections:			
measured	3255	2811	3270
independent,	1508	1474	1515
observed $(I > 3\sigma(I))$	814	1254	1315
R_{int} (obs/all)	0.0364/0.0406	0.0550/0.0553	0.0299/0.0303
Redundancy	2.158	1.907	2.158
$(\sin\theta/\lambda)_{max}(\text{Å}^{-1})$	0.789	0.789	0.790
Refinement			
No. of parameters	110	110	110
R_F(obs)(main + superlattice)	0.0807	0.0674	0.0665
R_F(obs)(main)	0.0919	0.0746	0.0708
R_F(obs)(superlattice)	0.0789	0.0664	0.0659
wR_F(all)(main + superlattice)	0.0969	0.0784	0.0789
wR_F(all)(main)	0.1087	0.1121	0.0943
wR_F(all)(superlattice)	0.0943	0.0717	0.0764
$\Delta\rho_{min}/\Delta\rho_{max}(\text{e}\text{Å}^{-3})$	-1.58/1.38	-1.91/1.70	-1.61/1.25

Table B.5: continued from previous page

	24.8 GPa*	29.9 GPa	35.4 GPa
Crystal data			
a(Å)	11.1315(3)	10.9986(2)	10.9569(3)
b(Å)	9.0170(2)	8.8988(2)	8.8396(2)
c(Å)	12.615(4)	12.5663(29)	12.4125(32)
V(Å^3)	1266.2(4)	1229.9(3)	1202.2(3)
α(°)	90.0	90.0	90.0
Space group	$P2_1/c$	$P2_1/c$	$P2_1/c$
Data collection			
No. of reflections:			
measured,	3251	3093	3052
independent,	1504	1452	1421
observed $(I > 3\sigma(I))$	790	1278	1280
R$_{int}$ (obs/all)	0.0322/0.0361	0.0323/0.0326	0.0314/0.0316
Redundancy	2.162	2.130	2.148
$(\sin\theta/\lambda)_{max}$(Å^{-1})	0.787	0.784	0.788
Refinement			
No. of parameters	110	110	110
R$_F$(obs)(main + superlattice)	0.0783	0.0747	0.0649
R$_F$(obs)(main)	0.0974	0.0879	0.0778
R$_F$(obs)(superlattice)	0.0754	0.0730	0.0629
wR$_F$(all)(main + superlattice)	0.0928	0.0855	0.0783
wR$_F$(all)(main)	0.1094	0.1085	0.0996
wR$_F$(all)(superlattice)	0.0891	0.0817	0.0744
$\Delta\rho_{min}/\Delta\rho_{max}$(eÅ^{-3})	-1.53/1.44	-2.04/1.42	-1.58/1.21

Table B.5: continued from previous page

	38.0 GPa*	41.7 GPa	45.3 GPa
Crystal data			
a(Å)	10.9243(4)	10.9331(4)	10.9154(6)
b(Å)	8.7832(4)	8.7705(4)	8.7445(5)
c(Å)	12.339(6)	12.217(5)	12.121(7)
V(Å^3)	1183.9(6)	1171.5(5)	1157.0(7)
Space group	*Pcmn*	*Pcmn*	*Pcmn*
Data collection			
No. of reflections:			
measured,	2655	2566	3052
independent,	763	780	1421
observed ($I > 3\sigma(I)$)	644	633	1280
R$_{int}$ (obs/all)	0.0322/0.0325	0.0283/0.0292	0.0314/0.0316
Redundancy	3.48	3.29	2.148
$(\sin\theta/\lambda)_{max}$(Å^{-1})	0.785	0.782	0.788
Refinement			
No. of parameters	112	112	112
R$_F$(obs)(main + superlattice)	0.0368	0.0368	0.0399
R$_F$(obs)(main)	0.0525	0.0488	0.0510
R$_F$(obs)(superlattice)	0.0350	0.0346	0.0381
wR$_F$(all)(main + superlattice)	0.0482	0.0464	0.0516
wR$_F$(all)(main)	0.0717	0.0672	0.0707
wR$_F$(all)(superlattice)	0.0446	0.0422	0.0480
$\Delta\rho_{min}/\Delta\rho_{max}$(eÅ^{-3})	-0.69/0.60	-0.72/0.79	-0.82/0.77

Table B.5: continued from previous page

	50.5 GPa
Crystal data	
$a(\text{Å})$	10.9081(9)
$b(\text{Å})$	8.7097(7)
$c(\text{Å})$	12.005(10)
$V(\text{Å}^3)$	1140(1)
Space group	$Pcmn$
Data collection	
No. of reflections:	
measured,	2809
independent,	768
observed $(I > 3\sigma(I))$	627
R_{int} (obs/all)	0.0307/0.0313
Redundancy	3.658
$(\sin\theta/\lambda)_{max}(\text{Å}^{-1})$	0.782
Refinement	
No. of parameters	112
R_F(obs)(main + superlattice)	0.0366
R_F(obs)(main)	0.0484
R_F(obs)(superlattice)	0.0345
wR_F(all)(main + superlattice)	0.0463
wR_F(all)(main)	0.0675
wR_F(all)(superlattice)	0.0421
$\Delta\rho_{min}/\Delta\rho_{max}(\text{e}\text{Å}^{-3})$	-0.72/0.81

Appendix C

Spin-Peierls distortions in TiPO$_4$

C.1   Electronic Structure Calculations

Density functional theory (DFT) electronic band structure calculations have been carried out employing the Vienna *ab initio* simulation package [172–174] with the projected augmented wave method, and the generalized gradient approximation (GGA) for the exchange and the correlation functional [175]. To account for the electron correlation associated with the Ti $3d$ state, we performed the GGA plus on-site repulsion (GGA+U) calculations [176] with an effective $U_{\text{eff}} = U$ - $J = 2$ and 3 eV on Ti. We used a plane-wave cutoff energy of 600 eV, a set of 64k points in the irreducible Brillouin zone, and the threshold of 10^{-6} eV for the self-consistent-field convergence of the total electronic energy.

C.2   X-ray diffraction

Laboratory-based signle-crystal X-ray diffraction was performed on a selected high-quality single crystal using a Marresearch MAR345dtb image-plate diffractometer with MoKα radiation from rotating anode. The software $CrysAlis^{Pro}$ [50] was used to extract lattice parameters and integrated intensities of Bragg reflections from the measured images.

Synchrotron-based single-crystal X-ray diffraction was performed at the beamline D3 of Hasylab (DESY, Hamburg). A high-quality single crystal has been glued to a carbon fiber that was placed into the closed-cycle helium cryostat mounted on a four-circle Huber diffractometer, equipped with a scintillation detector. Diffraction data were measured at selected temperatures between 10 K and room temperature. Two complete data sets were collected at 10 K and 82 K corresponding to the

commensurate and the incommensurate phases. Integrated intensities of the Bragg reflections were measured by ω-scans up to a resolution of $\sin(\theta)/\lambda = 0.7$ Å^{-1}. A monochromatic X-ray beam with wavelength of 0.5600 Å was used for the data collection at 10 K and for all temperature-dependent measurements. The data collection at 82 K was performed with radiation of wavelength of 0.5608 Å. Structure refinements were performed with JANA2006 computer program [88]. The temperature dependence of the incommensurate modulation wavevector was determined by $\mathbf{q}$-scans along $\mathbf{a}^*$ and by determination of fractional h indices of centered satellite reflections from the orientation matrix.

C.3 Thermal Expansion

A crystal of TiPO$_4$ of dimension $\sim 1.5 \times 1 \times 1$ mm^3 was selected and oriented by neutron Laue backscattering. Subsequently parallel faces perpendicular to the three crystallographic directions were polished. The length change versus temperature and magnetic field was measured with a miniature capacitance dilatometer calibrated against Cu and Ag standard samples [179].

C.4   Crystal Structures

Crystal structure at room temperature

The following Tables C.1 - C.3 contain the detalis of the data collection and structure refinement details of the laboratory based experiments.

Table C.1: Crystal data and data collection details of the room-temperature phase of TiPO$_4$.

Empirical formula	TiPO$_4$
Molar weight (g·mol^{-1})	142.85
Temperature (K)	292.0(2)
Calculated density (g·cm^{-3})	3.5616
Radiation, Wavelength (Å)	Mo-K_α, 0.71073
Absorption coefficient (mm^{-1})	3.605
Data collection mode	ϕ scans, $0 \leq \phi \leq 360°$, $\Delta\phi = 1°$
Space group	$Cmcm$
a (Å)	5.3009(1)
b (Å)	7.9116(2)
c (Å)	6.3502(1)
V (Å^3)	266.32(1)
Z	4
θ range for data collection (°)	4.6 to 39.5
Coverage at θ_{max} (%)	86.70
Limiting indices	$-9 \leq h \leq 9$; $-11 \leq k \leq 11$; $-11 \leq l \leq 11$
Measured/independent reflections	2880/404
Independent reflections with $I > 3\sigma(I)$	377
R_{int} (obs/all)	0.0225/0.0226
Redundancy	7.129
R_{obs}/R_{all}	0.0186/0.0205
wR_{obs}/wR_{all}	0.0307/0.0309
Parameters refined	22
Min./max res. electron density (e·Å^{-3})	-0.34/0.41

R is defined as $\frac{\Sigma||F_o|-|F_c||}{\Sigma|F_o|}$; weighting scheme $(\sigma^2(F) + (0.01F)^2)^{-1}$

Table C.2: Fractional coordinates and anisotropic displacement parameters (Å^2) of the atoms in $TiPO_4$ at room temperature.

atom	x/a	y/b	z/c	U_{11}	U_{22}	U_{33}	U_{12}	U_{13}	U_{23}
Ti1	0	0	0	0.00455(17)	0.0043(2)	0.00523(17)	0	0	0.00024(9)
P1	0.5	0.14995(6)	0.25	0.0036(2)	0.0043(3)	0.0043(2)	0	0	0
O1	0.5	0.25707(14)	0.05144(16)	0.0067(5)	0.0066(5)	0.0078(4)	0	0	0.0026(3)
O2	0.25936(19)	0.03733(13)	0.25	0.0045(4)	0.0060(4)	0.0064(4)	-0.0012(3)	0	0

Table C.3: Selected geometric parameters for the room-temperature phase of $TiPO_4$.

Atoms	Distance (Å)	Atoms	Distance (Å)
Ti1—Ti1^i	3.1751(1)	Ti1—O2^v	2.1208(7)
Ti1—Ti1^{ii}	3.1751(1)	Ti1—O2^{vi}	2.1208(7)
Ti1—O1^{iii}	1.9495(11)	P1—O1^{vii}	1.5192(11)
Ti1—O1^{iv}	1.9495(11)	P1—O1	1.5192(11)
Ti1—O2	2.1208(7)	P1—O2	1.5560(11)
Ti1—O2^i	2.1208(7)	P1—O2^{vii}	1.5560(11)

Atoms	Angle (°)	Atoms	Angle (°)
Ti1^i—Ti1—Ti1^{ii}	180.0	O2—Ti1—O2^v	80.82(3)
O1^{iii}—Ti1—O1^{iv}	180.0	O2—Ti1—O2^{vi}	99.18(3)
O1^{iii}—Ti1—O2	90.68(4)	O2^i—Ti1—O2^v	99.18(3)
O1^{iii}—Ti1—O2^i	89.32(4)	O2^i—Ti1—O2^{vi}	80.80(3)
O1^{iii}—Ti1—O2^v	90.68(4)	O2^v—Ti1—O2^{vi}	180.0
O1^{iii}—Ti1—O2^{vi}	89.32(4)	O1—P1—O1^{vii}	112.19(7)
O1^{iv}—Ti1—O2	89.32(4)	O1—P1—O2	108.63(3)
O1^{iv}—Ti1—O2^i	90.68(4)	O1—P1—O2^{vii}	108.63(3)
O1^{iv}—Ti1—O2^v	89.32(4)	O1^{vii}—P1—O2	108.63(3)
O1^{iv}—Ti1—O2^{vi}	90.68(4)	O1^{vii}—P1—O2^{vii}	108.63(3)
O2—Ti1—O2^i	180.0	O2—P1—O2^{vii}	110.13(6)

Symmetry codes: (i) $-x, -y, z - \frac{1}{2}$; (ii) $-x, -y, z + \frac{1}{2}$; (iii) $x - \frac{1}{2}, y - \frac{1}{2}, z$; (iv) $x - \frac{1}{2}, -y + \frac{1}{2}, -z$; (v) $-x, y, -z + \frac{1}{2}$; (vi) $x, -y, -z$; (vii) $-x + 1, y, -z + \frac{1}{2}$

Low-temperature crystal structures

The following tables (C.4-C.10) summarize data collection and structure refinement details at low temperatures as well as selected interatomic distances and angles for the possible low-temperature (10 K) models and the for incommensurate phase determined from the data collected at 82 K.

Table C.4: Crystal data and data collection details of the low-temperature phases of $TiPO_4$.

	Lock-in phase	Incommensurate phase
Empirical formula	$TiPO_4$	$TiPO_4$
Molar weight (g·mol^{-1})	142.85	142.85
Crystal size, mm^3	$0.1 \times 0.08 \times 0.06$	$0.1 \times 0.08 \times 0.06$
Temperature (K)	10.0(3)	82.00(3)
Calculated density (g·cm^{-3})	3.4945	3.4953
Wavelength (Å)	0.5600	0.5608
Absorption coefficient (mm^{-1})	1.768	1.807
Data collection mode	ω scans	ω scans
Superspace group	$Cmcm(\sigma_1 00)0s0$	$Cmcm(\sigma_1 00)0s0$
$\mathbf{q}$-vector	$(\frac{1}{2}, 0, 0)$	$(0.547, 0, 0)$
a (Å)	5.345(3)	5.340(4)
b (Å)	7.981(6)	7.979(7)
c (Å)	6.364(5)	6.369(8)
V (Å^3)	271.48(33)	271.37(50)
F(000)	276.0	276.0
Z	4	4
θ range for data collection (°)	2.5 to 23.05	2.5 to 24.80
Coverage at θ_{max} (%)	72.76	81.28
Limiting indices	$-7 \leq h \leq 5$	$-7 \leq h \leq 5$
	$-5 \leq k \leq 11$	$-5 \leq k \leq 11$
	$-4 \leq l \leq 8$	$-4 \leq l \leq 8$
	$-1 \leq m \leq 1$	$-1 \leq m \leq 1$
Main reflections	769	851
Independent main reflections	246	228
Main reflections with $I > 3\sigma(I)$	717	835
Independent main reflections with $I > 3\sigma(I)$	219	220
Satellite reflections	903	988
Independent satellite reflections	386	419
Satellite reflections with $I > 3\sigma(I)$	563	493
Independent satellite reflections with $I > 3\sigma(I)$	247	214
R$_{int}$ (obs/all)	0.0102/0.0103	0.0138/0.0139
Redundancy	2.646	2.842
Parameters refined	33	33

Table C.5: Details of the TiPO$_4$ structure refinement in superspace. Given are the agreement factors for three possible models at 10K and for the incommensurately modulated phase (IC) at 82K.

	$Pbnm$	$Pmnm$	$P2_1nm$	IC
$R_{all}(I > 3\sigma(I))$	0.0289	0.0289	0.0289	0.0302
$R_{main}(I > 3\sigma(I))$	0.0273	0.0272	0.0272	0.0287
$R_{sat}(I > 3\sigma(I))$	0.0517	0.0519	0.0518	0.0573
$wR_{all}(I > 3\sigma(I))$	0.0580	0.0581	0.0580	0.0624
$wR_{main}(I > 3\sigma(I))$	0.0599	0.0599	0.0599	0.0644
$wR_{sat}(I > 3\sigma(I))$	0.0507	0.0508	0.0508	0.0512
R_{all} (all data)	0.0345	0.0349	0.0349	0.0395
R_{main} (all data)	0.0287	0.0290	0.0290	0.0294
R_{sat} (all data)	0.1078	0.1080	0.1079	0.1941
wR_{all} (all data)	0.0590	0.0590	0.0590	0.0632
wR_{main} (all data)	0.0604	0.0604	0.0604	0.0644
wR_{sat} (all data)	0.0536	0.0538	0.0537	0.0565

R is defined as $\frac{\Sigma||F_o|-|F_c||}{\Sigma|F_o|}$; weighting scheme $(\sigma^2(F) + (0.01F)^2)^{-1}$

Table C.6: Structural parameters for the commensurate phase of $TiPO_4$ at 10K. Co-ordinates are given with respect to the average unit cell. Modulation amplitudes are recalculated in Å. Refinement was performed with $t_0 = \frac{1}{8}$, corresponding to the *Pbnm* symmetry of the $2a \times b \times c$ supercell.

	Ti1	P1	O1	O2
x/a	0	0.5	0.5	0.2591(2)
y/b	0	0.1505(7)	0.25669(14)	0.03703(13)
z/c	0	0.25	0.05079(19)	0.25
U_{11} (Å^2)	0.0045(4)	0.0041(4)	0.0049(5)	0.0034(6)
U_{22} (Å^2)	0.0044(4)	0.0053(4)	0.0056(6)	0.0094(5)
U_{33} (Å^2)	0.0053(4)	0.0051(4)	0.0076(6)	0.0071(6)
U_{12} (Å^2)	0	0	0	-0.0008(4)
U_{13} (Å^2)	0	0	0	0
U_{23} (Å^2)	-0.00015(11)	0	-0.0007(5)	0
A_x (Å)	0	0	0	-0.0147(7)
B_x (Å)	0	0.0215(4)	0.0103(7)	0.0152(7)
A_y (Å)	0.0037(3)	0.0106(4)	0.0078(7)	0.0099(8)
B_y (Å)	0	0	0	0.0031(7)
A_z (Å)	-0.0339(2)	0	-0.0025(8)	0
B_z (Å)	0	0	0	0

Table C.7: Structural parameters for the incommensurate phase of TiPO$_4$ at 82K. Coordinates are given with respect to the average unit cell. Modulation amplitudes are recalculated in Å.

	Ti1	P1	O1	O2
x/a	0	0.5	0.5	0.2591(2)
y/b	0	0.14984(7)	0.25654(15)	0.03697(15)
z/c	0	0.25	0.05215(19)	0.25
U_{11} (Å^2)	0.0041(4)	0.0036(4)	0.0062(6)	0.0038(7)
U_{22} (Å^2)	0.0036(4)	0.0042(4)	0.0062(6)	0.0053(5)
U_{33} (Å^2)	0.0057(4)	0.0040(4)	0.0035(6)	0.0075(7)
U_{12} (Å^2)	0	0	0	-0.0006(4)
U_{13} (Å^2)	0	0	0	0
U_{23} (Å^2)	-0.00071(12)	0	0.006(5)	0
A_x (Å)	0	0	0	-0.0123(8)
B_x (Å)	0	0.0166(4)	0.0078(8)	0.0117(8)
A_y (Å)	0.0039(4)	0.0094(5)	0.0065(8)	0.0078(8)
B_y (Å)	0	0	0	0.0030(8)
A_z (Å)	-0.0274(2)	0	-0.0016(9)	0
B_z (Å)	0	0	0	0

Table C.8: Selected interatomic distances (Å) and angles (°) for the *Pbnm* model of the low temperature commensurate phase at 10 K and for the incommensurate phase at 82 K. Given are the average (Ave), minimal (Min), maximal (Max) values and difference (Δ) between them. Distances and angles for the room-temperature (RT) phase are given in the last column. Standard uncertainties are in parentheses.

Atoms	10K			82K				RT
	Ave	Min	Max	Ave	Min	Max	Δ	
Ti1—Ti1	3.182(5)	3.134(5)	3.230(5)	3.1847(2)	3.1300(3)	3.2394(3)	0.1094	3.1751(1)
Ti1—O1	1.969(3)	1.968(3)	1.969(3)	1.9708(13)	1.9692(15)	1.9725(15)	0.0033	1.9495(11)
Ti1—O2	2.130(2)	2.121(2)	2.139(2)	2.130(5)	2.121(5)	2.139(5)	0.018	2.1208(7)
O2—Ti1—O2[1]	81.12(5)	79.68(5)	82.55(5)	81.02(9)	79.48(9)	82.56(9)	3.08	80.82(3)
O2—Ti1—O2[2]	98.89(5)	98.89(5)	98.89(5)	98.98(9)	98.98(9)	98.99(9)	0.01	99.18(3)
P1—O1	1.5265(19)	1.5261(19)	1.5269(19)	1.5208(14)	1.5206(15)	1.5210(15)	0.0004	1.5192(11)
P1—O2	1.5726(10)	1.5698(10)	1.5753(10)	1.571(6)	1.568(6)	1.572(6)	0.004	1.5560(11)
O1—P1—O1	112.30(6)	112.10(6)	112.49(6)	111.92(12)	111.69(12)	112.16(12)	0.47	112.19(7)
O2—P1—O2	109.93(5)	109.88(5)	109.97(5)	110.02(11)	109.90(11)	110.14(11)	0.24	110.13(6)
O1—P1—O2	108.65(2)	108.40(2)	108.90(4)	108.70(5)	108.49(6)	108.96(6)	0.47	108.63(2)

[1] Along **c**

[2] Along **a**

Table C.9: Structural parameters for three LT models of TiPO$_4$ obtained from the superspace refinement. Coordinates are given with respect to the $2a \times b \times c$ supercell.

atom	x/a	y/b	z/c	U_{11} (Å^2)	U_{22} (Å^2)	U_{33} (Å^2)	U_{12} (Å^2)	U_{13} (Å^2)	U_{23} (Å^2)
(b) *Pbnm* model. Inversion center at (000)									
Ti1	0.125	0.25033(4)	0.99624(4)	0.0045(4)	0.0044(4)	0.0053(4)	0	0	-0.00015(11)
P1	0.12642(7)	0.90108(7)	0.25	0.0041(4)	0.0053(4)	0.0051(4)	0	0	0
P2	0.62358(7)	0.89921(7)	0.25	0.0041(4)	0.0053(4)	0.0051(4)	0	0	0
O11	0.37568(6)	0.99400(14)	0.94894(19)	0.0049(5)	0.0056(6)	0.0076(6)	0	0	-0.0007(5)
O12	0.87432(6)	0.99262(14)	0.94949(19)	0.0049(5)	0.0056(6)	0.0076(6)	0	0	-0.0007(5)
O21	0.25313(11)	0.28826(14)	0.25	0.0034(6)	0.0094(5)	0.0071(6)	-0.0008(4)	0	0
O22	0.75595(11)	0.28580(14)	0.25	0.0034(6)	0.0094(5)	0.0071(6)	-0.0008(4)	0	0
O23	0.50316(11)	0.78661(14)	0.25	0.0034(6)	0.0094(5)	0.0071(6)	-0.0008(4)	0	0
O24	0.00592(11)	0.7874(14)	0.25	0.0034(6)	0.0094(5)	0.0071(6)	-0.0008(4)	0	0
(a) *Pmnm* model. Inversion center at (000)									
Ti1	0	0	0	0.0045(4)	0.0044(4)	0.0052(4)	0	0	-0.00015(11)
Ti2	0.25	0.50046(4)	0.99466(4)	0.0045(4)	0.0044(4)	0.0052(4)	0	0	-0.00015(11)
P1	0.00201(7)	0.65016(7)	0.25	0.0041(4)	0.0053(4)	0.0051(4)	0	0	0
P2	0.25	0.15148(7)	0.25	0.0041(4)	0.0053(4)	0.0051(4)	0	0	0
P3	0.75	0.14884(7)	0.25	0.0041(4)	0.0053(4)	0.0051(4)	0	0	0
O11	0.25	0.74429(14)	0.94882(19)	0.0049(5)	0.0056(6)	0.0076(6)	0	0	-0.0007(5)
O12	0.75	0.74233(14)	0.94960(19)	0.0049(5)	0.0056(6)	0.0076(6)	0	0	-0.0007(5)
O13	0.50096(7)	0.24331(14)	0.94921(19)	0.0049(5)	0.0056(6)	0.0076(6)	0	0	-0.0007(5)
O21	0.12952(11)	0.03819(14)	0.25	0.0034(6)	0.0094(5)	0.0071(6)	-0.0008(4)	0	0
O22	0.62956(11)	0.03587(14)	0.25	0.0034(6)	0.0094(5)	0.0071(6)	-0.0008(4)	0	0
O23	0.37757(11)	0.53760(14)	0.25	0.0034(6)	0.0094(5)	0.0071(6)	-0.0008(4)	0	0
O24	0.88152(11)	0.53646(14)	0.25	0.0034(6)	0.0094(5)	0.0071(6)	-0.0008(4)	0	0
(b) *P2$_1$nm* model.									
Ti1	0	0.00018(4)	0.24796(4)	0.0045(4)	0.0044(4)	0.0053(4)	0	0	-0.00015(11)
Ti2	0.25	0.50043(4)	0.24507(4)	0.0045(4)	0.0044(4)	0.0051(4)	0	0	-0.00015(11)
P1	0.00186(7)	0.65065(7)	0.5	0.0041(4)	0.0053(4)	0.0051(4)	0	0	0
P2	0.49815(7)	0.64964(7)	0.5	0.0041(4)	0.0053(4)	0.0051(4)	0	0	0
P3	0.24923(7)	0.15137(7)	0.5	0.0041(4)	0.0053(4)	0.0051(4)	0	0	0
P4	0.75077(7)	0.14893(7)	0.5	0.0041(4)	0.0053(4)	0.0053(4)	0	0	0
O11	0.25037(6)	0.74421(14)	0.19885(19)	0.0049(5)	0.0056(6)	0.0076(6)	0	0	-0.0007(5)
O12	0.74963(6)	0.74241(14)	0.19957(19)	0.0049(5)	0.0056(6)	0.0076(6)	0	0	-0.0007(5)
O13	0.50089(6)	0.24294(14)	0.19936(19)	0.0049(5)	0.0056(6)	0.0076(6)	0	0	-0.0007(5)
O14	0.99911(6)	0.24368(14)	0.19906(19)	0.0049(5)	0.0056(6)	0.0076(6)	0	0	-0.0007(5)
O21	0.12877(11)	0.03833(14)	0.5	0.0034(6)	0.0094(5)	0.0071(6)	-0.0008(4)	0	0
O22	0.63032(11)	0.03573(14)	0.5	0.0034(6)	0.0094(5)	0.0071(6)	-0.0008(4)	0	0
O23	0.86972(11)	0.96211(14)	0	0.0034(6)	0.0094(5)	0.0071(6)	-0.0008(4)	0	0
O24	0.37120(11)	0.96383(14)	0	0.0034(6)	0.0094(5)	0.0071(6)	-0.0008(4)	0	0
O25	0.37772(11)	0.53711(14)	0.5	0.0034(6)	0.0094(5)	0.0071(6)	-0.0008(4)	0	0
O26	0.88136(11)	0.53695(14)	0.5	0.0034(6)	0.0094(5)	0.0071(6)	-0.0008(4)	0	0
O27	0.11863(11)	0.46395(14)	0	0.0034(6)	0.0094(5)	0.0071(6)	-0.0008(4)	0	0
O28	0.62229(11)	0.46199(14)	0	0.0034(6)	0.0094(5)	0.0071(6)	-0.0008(4)	0	0

Atoms O1x and O2x correspond to apical and equatorial oxygen atoms respectively

Table C.10: Selected interatomic distances and angles for the *Pbnm* model of the low temperature phase at 10 K.

Atoms	Distance (Å)	Atoms	Distance (Å)
Ti1—Ti1^{i}	3.134(5)	P1—O12^{ix}	1.5269(19)
Ti1—Ti1^{ii}	3.230(5)	P1—O12^{x}	1.5269(19)
Ti1—O11^{iii}	1.968(3)	P1—O21^{xi}	1.5711(10)
Ti1—O12^{iv}	1.969(3)	P1—O24^{xii}	1.5753(10)
Ti1—O21^{v}	2.139(2)	P2—O11^{ix}	1.5261(19)
Ti1—O22^{vi}	2.121(2)	P2—O11^{x}	1.5261(19)
Ti1—O23^{vii}	2.137(2)	P2—O22^{xiii}	1.5740(10)
Ti1—O24^{viii}	2.122(2)	P2—O23	1.5698(10)

Atoms	Angle (°)	Atoms	Angle (°)
Ti1^{i}—Ti1—Ti1^{ii}	180.0	O22^{vi}—Ti1—O24^{viii}	82.55(5)
O11^{iii}—Ti1—O12^{iv}	178.6967(14)	O23^{vii}—Ti1—O24^{viii}	98.89(5)
O11^{iii}—Ti1—O21^{v}	88.737(16)	O12^{ix}—P1—O12^{x}	112.49(6)
O11^{iii}—Ti1—O22^{vi}	91.362(16)	O12^{ix}—P1—O21^{xi}	108.83(2)
O11^{iii}—Ti1—O23^{vii}	88.814(16)	O12^{ix}—P1—O24^{xii}	108.40(2)
O11^{iii}—Ti1—O24^{viii}	91.434(16)	O12^{x}—P1—O21^{xi}	108.83(2)
O12^{iv}—Ti1—O21^{v}	90.262(18)	O12^{x}—P1—O24^{xii}	108.40(2)
O12^{iv}—Ti1—O22^{vi}	89.617(17)	O21^{xi}—P1—O24^{xii}	109.88(5)
O12^{iv}—Ti1—O23^{vii}	90.185(17)	O11^{ix}—P2—O11^{x}	112.10(6)
O12^{iv}—Ti1—O24^{viii}	89.546(18)	O11^{ix}—P2—O22^{xiii}	108.48(2)
O21^{v}—Ti1—O24^{vi}	98.89(5)	O11^{ix}—P2—O23	108.90(2)
O21^{v}—Ti1—O23^{vii}	79.68(5)	O11^{x}—P2—O22^{xiii}	108.48(2)
O21^{v}—Ti1—O24^{viii}	178.5483(2)	O11^{x}—P2—O23	108.90(2)
O22^{vi}—Ti1—O23^{vii}	178.5474(2)	O22^{xiii}—P2—O23	109.97(5)

Symmetry codes: (i) $x, y, -z + \frac{3}{2}$; (ii) $x, y, -z + \frac{5}{2}$; (iii) $-x + \frac{1}{2}, y - \frac{1}{2}, z$; (iv) $-x + 1, -y + 1, -z + 2$; (v) $x, y, z + 1$; (vi) $x - \frac{1}{2}, -y + \frac{1}{2}, -z + 1$; (vii) $-x + \frac{1}{2}, y - \frac{1}{2}, -z + \frac{3}{2}$; (viii) $-x + 1, -y + 1, z + \frac{1}{2}$; (ix) $-x + 1, -y + 2, z - \frac{1}{2}$; (x) $-x + 1, -y + 2, -z + 1$; (xi) $-x + \frac{1}{2}, y + \frac{1}{2}, -z + \frac{1}{2}$; (xii) $x - 1, y, z$; (xiii) $-x + \frac{3}{2}, y + \frac{1}{2}, -z + \frac{1}{2}$

t-plots

For the analysis of the low-temperature structures we use t-plots (Fig. C.1), where atomic displacements, interatomic distances and angles can be directly compared, and correlations between them can be studied [52].

First, consider a Ti1a atom at $(0,0,0)$ in the basic structure (Fig. C.1(a)). Within the superspace description its z coordinate is defined as $z = \bar{z} + A_z \sin(2\pi(t + \mathbf{q}\bar{\mathbf{x}})) = A_z \sin(2\pi t)$. Atom Ti1b is generated from Ti1a by the reflection in the m_z plane at $(x, y, \frac{1}{4})$. Therefore, its z-coordinate can be calculated as $z(\text{Ti1b}) = 0.5 - A_z \sin(2\pi t)$. Displacements of neighboring Ti atoms along y are in-phase (and very small) and, therefore, they do not influence the intrachain Ti-Ti distances. The Ti1a-Ti1b distance is then defined by the equation:

$$d(\text{Ti1a–Ti1b}) = (0.5 - 2A_z \sin(2\pi t)) \cdot c. \tag{C.1}$$

The second nearest neighboring Ti atom along the chain (Ti1b$'$) is generated by the reflection of Ti1a in the m_z plane at $(x, y, -\frac{1}{4})$. Thus:

$$d(\text{Ti1a–Ti1b}') = (0.5 + 2A_z \sin(2\pi t)) \cdot c. \tag{C.2}$$

Results of similar calculations for atoms Ti1c-Ti1e are summarized in the Table C.11. One can notice that Ti chains separated by the C center of the basic structure (atoms Ti1c–Ti1d vs Ti1a–Ti1b in Fig. C.1(a)) are $\frac{\pi}{2}$ out of phase for the low-temperature phase, while Ti chains separated by one translation along $\mathbf{a}$ (atoms Ti1e–Ti1f vs Ti1a–Ti1b in Fig. C.1(a)) are π out of phase (Fig. C.1(b), Table C.11).

These commensurate phase relations lead to the dependence of the 3D structural model on the t-sections of the superspace. At $t = 0$, only Ti1c–Ti1d chains are dimerized, while Ti1a–Ti1b and Ti1e-Ti1f chains remain uniform. This arrangement correspond to the $Pmnm$ symmetry of a $2a \times b \times c$ supercell. At $t = \frac{1}{8}$ all chains are dimerized with alternating Ti–Ti intrachain distances equal to $(0.5 \pm \sqrt{2} A_z) \cdot c$. The t-plot for the commensurate phase is presented on the Fig.C.1(b). Vertical dashed lines are drown at $t = \frac{1}{8} + \frac{N}{4}(N = 0, 1, 2, 3)$ all leading to equivalent 3D structural models (with $Pbnm$ symmetry) different only in their origin. The model with $t = \frac{1}{16}$ corresponds to the $P2_1nm$ symmetry of the $2a \times b \times c$ supercell. It contains two types of Ti–Ti chains with different degrees of dimerization (Table C.11).

The incommensurate value of the σ_1 component of the modulation wavevector $\mathbf{q}$ leads to different phase relations. Thus, the curves on Fig. C.1 (c) don't intersect exactly at $t = \frac{1}{8} + \frac{N}{4}$. Furthermore, the phase shift different from π can be

Table C.11: Ti–Ti distances as functions of the modulation amplitude (t) and σ_1 component of the modulation wavevector $\mathbf{q}$. Distances are given related to the lattice parameter c.

Distance	General formula	$\sigma_1 = \frac{1}{2}, t = 0$	$\sigma_1 = \frac{1}{2}, t = \frac{1}{8}$	$\sigma_1 = \frac{1}{2}, t = \frac{1}{16}$	$\sigma_1 = 0.547$
Ti1a–Ti1b	$0.5 - 2A_z \sin(2\pi t)$	0.5	$0.5 - \sqrt{2}A_z$	$0.5 - 0.38A_z$	$0.5 - 2A_z \sin(2\pi t)$
Ti1a–Ti1b′	$0.5 + 2A_z \sin(2\pi t)$	0.5	$0.5 + \sqrt{2}A_z$	$0.5 + 0.38A_z$	$0.5 + 2A_z \sin(2\pi t)$
Ti1c–Ti1d	$0.5 - 2A_z \sin(2\pi(t + \frac{1}{2}\sigma_1))$	$0.5 - 2A_z$	$0.5 - \sqrt{2}A_z$	$0.5 - 1.85A_z$	$0.5 - 2A_z \sin(2\pi(t + 0.2735))$
Ti1c–Ti1d′	$0.5 + 2A_z \sin(2\pi(t + \frac{1}{2}\sigma_1))$	$0.5 + 2A_z$	$0.5 + \sqrt{2}A_z$	$0.5 + 1.85A_z$	$0.5 + 2A_z \sin(2\pi(t + 0.2735))$
Ti1e–Ti1f	$0.5 - 2A_z \sin(2\pi(t + \sigma_1))$	0.5	$0.5 + \sqrt{2}A_z$	$0.5 + 0.38A_z$	$0.5 - 2A_z \sin(2\pi(t + 0.547))$
Ti1e–Ti1f′	$0.5 + 2A_z \sin(2\pi(t + \sigma_1))$	0.5	$0.5 - \sqrt{2}A_z$	$0.5 - 0.38A_z$	$0.5 + 2A_z \sin(2\pi(t + 0.547))$

seen on Fig.C.1(d). Remaining t-plots (Fig. C.1(e)-(k)) show the variation of selected interatomic distances, bond angles and atomic displacements with the phase of modulation for the incommensurately modulated phase at 82K.

Several important structural features should be pointed out, besides the variation of Ti–Ti distances. The lack of significant variation of Ti–O and P–O bond lengths indicate that P and O atoms follow the modulation of the Ti atoms through elastic coupling. First of all, x-displacements of O2 atoms are perfectly correlated with z-displacements of the adjacent Ti atoms (Fig. C.1(i)). Since PO$_4$ tetrahedra reveal high rigidity (Fig. C.1(j),(k)), the modulations of P1 and O1 atoms are in-phase with those of the O2 atoms (Fig. C.1(h),(i)). Consequently, it explains the preference of the antiphase dimerization of Ti1a–Ti1b and Ti1e–Ti1f chains, since it minimizes the internal strain of the structure.
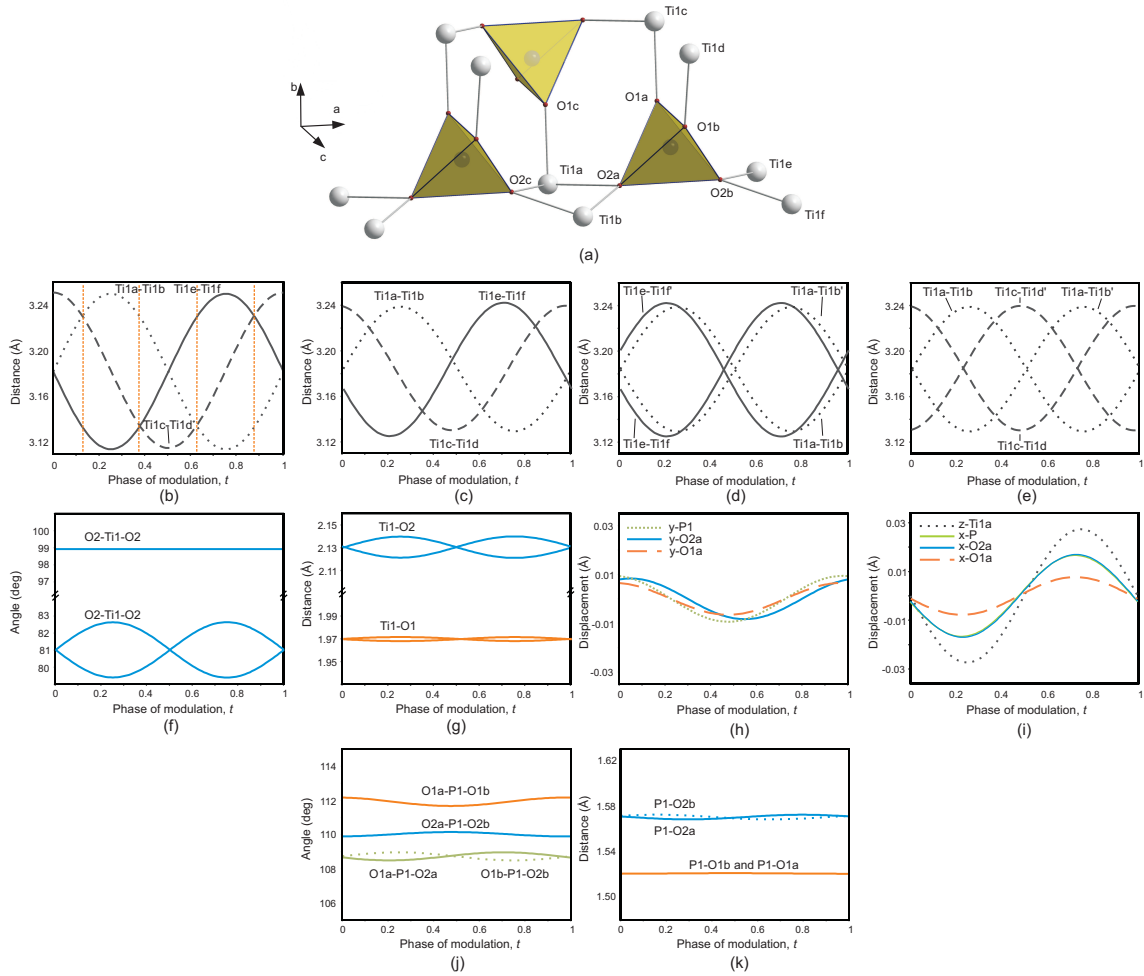
Figure C.1: (a) Fragment of the structure, showing the interchain connections through PO$_4$ tetrahedra. (b) t-plot of Ti–Ti distances for the low-temperature phase at 10 K. Vertical dashed lines indicate $t = \frac{1}{8} + \frac{N}{4}$ (c)–(k) Selected t-plots of interatomic distances, angles and atomic displacements for the IC phase at 82K. See text for explanation.

Bibliography

1. Friedrich, W., Knipping, P. & Laue, M. Interferenz-Erscheinungen bei Röntgenstrahlen. *Bayerische Akad. d. Wiss. zu München, Sitzungsber. math.-phys. Kl.* 303–322 (1912).

2. Watson, J. D. & Crick, F. H. C. Molecular Structure of Nucleic Acids: A Structure for Deoxyribose Nucleic Acid. *Nature* **171,** 737–738 (1953).

3. Kendrew, J. C. *et al.* A Three-Dimensional Model of the Myoglobin Molecule Obtained by X-Ray Analysis. *Nature* **181,** 662–666 (1958).

4. Schluenzen, F. *et al.* Structure of Functionally Activated Small Ribosomal Subunit at 3.3 Å Resolution. *Cell* **102,** 615–623 (2000).

5. Siegrist, T., Zahurak, S. M., Murphy, D. W. & Roth, R. S. The parent structure of the layered high-temperature superconductors. *Nature* **334,** 231–232 (1988).

6. Xue, Y. *et al.* Low temperature x-ray diffraction study on superconductivity. *J. Phys. Conf. Ser.* **150,** 052284 (2009).

7. Tateno, S., Hirose, K., Ohishi, Y. & Tatsumi, Y. The structure of iron in Earth's inner core. *Science* **330,** 359–361 (2010).

8. Dubrovinsky, L., Dubrovinskaia, N., Prakapenka, V. B. & Abakumov, A. M. Implementation of micro-ball nanodiamond anvils for high-pressure studies above 6 Mbar. *Nat. Commun.* **3,** 1163 (2012).

9. Goldsztaub, S. Structure cristalline de l'oxychlorare de fer. *Compt. rend.* **198,** 667–669 (1934).

10. Schäfer, H., Wittig, F. E. & Jori, M. Untersuchungen am System Fe_2O_3-$FeCl_3$-H_2O-HCl. IX. Die thermochemische Bestandigkeit des Eisenoxychlorids FeOCl. *Z. Anorg. Allg. Chem.* **287,** 61–70 (1956).

11. Schäfer, H., Wartenpfuhl, F. & Weise, E. Über Titanchloride. V. Titan(III)-oxychlorid. *Z. Anorg. Allg. Chem.* **295,** 268–280 (1958).

12. Schäfer, H. & Wartenpfuhl, F. Über das Vanadin(III)-oxydchlorid VOCl. *J. Less-Common Met.* **3,** 29–33 (1961).

13. Schäfer, H. & Wartenpfuhl, F. Das Chrom (III)-oxydchlorid CrOCl. *Z. Anorg. Allg. Chem.* **308,** 282–289 (1961).

14. Grant, R. W. Magnetic strucrure of FeOCl. *J. Appl. Phys.* **42,** 1619–1620 (1971).

15. Kostiner, E. & Steger, J. Mössbauer Effect Study of FeOCl. *J. Solid State Chem.* **3,** 273–275 (1971).

16. Christensen, A. N., Johansson, T. & Quézel, S. Preparation and Magnetic Properties of CrOCl. *Acta Chem. Scand. A* **28,** 1171–1174 (1975).

17. Adam, A. & Buisson, G. Structure magnétique cycloïdale de FeOCl. *Phys. Status Solidi A* **30,** 323–329 (1975).

18. Vénien, J. P., Palvadeau, P., Schleich, D. & Rouxel, J. Vanadium (III) oxychloride: Magnetic, optical and electrical properties; lithium and molecular intercalations. *Mater. Res. Bull.* **14,** 891–897 (1979).

19. Zhang, J. *et al.* Magnetoelastic coupling in the incommensurate antiferromagnetic phase of FeOCl. *Phys. Rev. B* **86,** 134428 (2012).

20. Angelkort, J., Wölfel, A., Schönleber, A., van Smaalen, S. & Kremer, R. K. Observation of strong magnetoelastic coupling in a first-order phase transition of CrOCl. *Phys. Rev. B* **80,** 144416 (2009).

21. Schönleber, A. *et al.* Phase transition, crystal structure, and magnetic order in VOCl. *Phys. Rev. B* **80,** 064426 (2009).

22. Halbert, T. R. & Scanlon, J. Organometallic intercalation compounds of FeOCl. *Mater. Res. Bull.* **14,** 415–421 (1979).

23. Kanatzidis, M. G., Tonge, L. M., Marks, T. J., Marcy, H. O. & Kannewurf, C. R. In Situ Intercalative Polymerization of Pyrrole in FeOCl: A New Class of Layered, Conducting Polymer-Inorganic Hybrid Materials. *J. Am. Chem. Soc.* **109,** 3797–3799 (1987).

24. Kanatzidis, M. G. *et al.* Intercalation chemistry of conducting polymers: New crystalline microlaminate phases in the polyaniline/FeOCl system. *Adv. Mater.* **2,** 364–366 (1990).

25. Wu, C.-G. *et al.* Reaction of Aniline with FeOCl. Formation and Ordering of Conducting Polyaniline in a Crystalline Layered Host. *J. Am. Chem. Soc.* **117,** 9229–9242 (1995).

26. Kargina, I. & Richeson, D. Diamine Intercalates of Titanium and Vanadium Oxychloride. Evidence for the Subsequent Substitution Reactions of TiOCl with Amines. *Chem. Mater.* **8,** 480–485 (1996).

27. Jarrige, I. *et al.* Charge transfer in FeOCl intercalation compounds and its pressure dependence: An x-ray spectroscopic study. *Phys. Rev. B* **82,** 165121 (2010).

28. Zhao, X., Zhao-Karger, Z., Wang, D. & Fichtner, M. Metal oxychlorides as cathode materials for chloride ion batteries. *Angew. Chem.* **52,** 13621–13624 (2013).

29. Coïc, L., Spiesser, M., Palvadeau, P. & Rouxel, J. Chromium (III) oxyhalides: Magnetic and optical properties. Lithium intercalation. *Mater. Res. Bull.* **16,** 229–236 (1981).

30. Clough, S., Palvadeau, P. & Venien, J. P. Dynamics of molecules intercalated in vanadium oxychloride: X-rays, NMR line widths and inelastic neutron scattering studies. *J. Phys. C: Solid State Phys.* **15,** 641–655 (1982).

31. Armand, M., Coic, L., Palvadeau, P. & Rouxel, J. The M-O-X transition metal oxyhalides: A new class of lamellar cathode material. *J. Power Sources* **3,** 137–144 (1978).

32. Sakaebe, H., Higuchi, S., Kanamura, K., Fujimoto, H. & Takehara, Z. Preparation of a FeOCl derivative with pyrrole and its performance as a cathode material in a secondary lithium battery system. *J. Power Sources* **56,** 165–169 (1995).

33. Kanatzidis, M. G., Marcy, H. O., McCarthy, W. J., Kannewurf, C. R. & Marks, T. J. In situ intercalative polymerization chemistry of FeOCl. Generation and properties of novel, highly conductive inorganic/organic polymer microlaminates. *Solid State Ionics* **32-33,** 594–608 (1989).

34. Seidel, A., Marianetti, C. A., Chou, F. C., Ceder, G. & Lee, P. A. S=1/2 chains and spin-Peierls transition in TiOCl. *Phys. Rev. B* **67,** 020405(R) (2003).

35. Saha-Dasgupta, T., Valentí, R., Rosner, H. & Gros, C. TiOCl, an orbital-ordered system? *Europhys. Lett.* **67,** 63–69 (2004).

36. Shaz, M. *et al.* Spin-Peierls transition in TiOCl. *Phys. Rev. B* **71,** 100405(R) (2005).

37. Schönleber, A., van Smaalen, S. & Palatinus, L. Structure of the incommensurate phase of the quantum magnet TiOCl. *Phys. Rev. B* **73,** 214410 (2006).

38. Komarek, A. C. *et al.* Strong magnetoelastic coupling in VOCl: Neutron and synchrotron powder x-ray diffraction study. *Phys. Rev. B* **79,** 104425 (2009).

39. Schönleber, A., van Smaalen, S., Kremer, R. K. & Senyshyn, A. *Incommensurate to commensurate magnetic ordering in antiferromagnetic CrOCl.* Unpublished. 2015.

40. Goodenough, J. B. *Magnetism and the Chemical Bond* (John Wiley & Sons, Inc., 1963).

41. Goodenough, J. Metallic oxides. *Prog. Solid State Chem.* **5,** 145–399 (1971).

42. Beynon, R. J. & Wilson, J. A. TiOCl, TiOBr - are these RVB d^1, S=1/2 materials? The results of scandium substitution set in the context of other S=1/2 systems of current interest for high-temperature superconductivity and the metal-insulator transition. *J. Phys. Condens. Matter* **5,** 1983–2000 (1993).

43. Kuntscher, C. A. *et al.* Possible pressure-induced insulator-to-metal transition in low-dimensional TiOCl. *Phys. Rev. B* **74,** 184402 (2006).

44. Forthaus, M. K., Taetz, T., Möller, A. & Abd-Elmeguid, M. M. Effect of pressure on the electrical transport and structure of TiOCl. *Phys. Rev. B* **77,** 165121 (2008).

45. Zhang, Y.-Z., Jeschke, H. O. & Valentí, R. Two Pressure-Induced Transitions in TiOCl: Mott Insulator to Anisotropic Metal. *Phys. Rev. Lett.* **101,** 136406 (2008).

46. Kuntscher, C. *et al.* Mott-Hubbard gap closure and structural phase transition in the oxyhalides TiOBr and TiOCl under pressure. *Phys. Rev. B* **78,** 035106 (2008).

47. Blanco-Canosa, S. *et al.* Enhanced Dimerization of TiOCl under Pressure: Spin-Peierls to Peierls Transition. *Phys. Rev. Lett.* **102,** 056406 (2009).

48. Blanco-Canosa, S. *et al.* High-pressure magnetic and structural properties of TiOX (X=Cl, Br). *J. Magn. Magn. Mater.* **322,** 1069–1071 (2010).

49. Ebad-Allah, J. *et al.* Two pressure-induced structural phase transitions in TiOCl. *Phys. Rev. B* **82,** 134117 (2010).

50. *Xcalibur/SuperNova CCD system, CrysAlisPro Software system, Version 1.171.36.28* Agilent Technologies UK Ltd. (Oxford, UK, 2012).

51. McMahon, M. I. & Nelmes, R. J. High-pressure structures and phase transformations in elemental metals. *Chem. Soc. Rev.* **35,** 943–963 (2006).

52. van Smaalen, S. *Incommensurate crystallography* (Oxford University Press, 2007).

53. Law, J. M. *et al.* Spin-Peierls transition in the S = 1/2 compound TiPO$_4$ featuring large intrachain coupling. *Phys. Rev. B* **83,** 180414(R) (2011).

54. Ekin, J. *Experimental techniques for low-temperature measurements: cryostat design, material properties and superconductor critical-current testing* (Oxford University Press, 2006).

55. *Closed Cycle Cryocooler Principles of Operation* Advanced Research Systems, 2014. <http://www.arscryo.com/tech-notes/cryocooler-principle-of-operation.html>.

56. Bassett, W. A. Diamond anvil cell, 50$^{\text{th}}$ birthday. *High Pressure Res.* **29,** 163–186 (2009).

57. *Schematics of the core of a diamond anvil cell.* 2009. <http://en.wikipedia.org/wiki/Mineral_physics#mediaviewer/File:DiaAnvCell1.jpg>.

58. Spain, I. & Dunstan, D. The technology of diamond anvil high-pressure cells: II. Operation and use. *J. Phys. E: Sci. Instrum.* **22,** 923–933 (1989).

59. Boehler, R. & de Hantsetters, K. New anvil designs in diamond-cells. *High Pressure Res.* **24,** 391–396 (2004).

60. Kantor, I. *et al.* BX90: a new diamond anvil cell design for X-ray diffraction and optical measurements. *Rev. Sci. Instrum.* **83,** 125102 (2012).

61. Kurnosov, A. *et al.* A novel gas-loading system for mechanically closing of various types of diamond anvil cells. *Rev. Sci. Instrum.* **79,** 045110 (2008).

62. Forman, R. A., Piermarini, G. J., Barnett, J. D. & Block, S. Pressure measurement made by the utilization of ruby sharp-line luminescence. *Science* **176,** 284–285 (1972).

63. Mao, H. K., Xu, J. & Bell, P. M. Calibration of the ruby pressure gauge to 800 kbar under quasi-hydrostatic conditions. *J. Geophys. Res.* **91,** 4673 (1986).

64. Fei, Y. *et al.* High-Pressure Geoscience Special Feature: Toward an internally consistent pressure scale. *Proc. Natl. Acad. Sci. U.S.A.* **104,** 9182–9186 (2007).

65. Angel, R. J. in *Advances in High-Pressure Technology for Geophysical Applications.* 371–396 (Elsevier B. V., Amsterdam, The Netherlands, 2005).

66. King, H. E. & Finger, L. W. Diffracted beam crystal centering and its application to high-pressure crystallography. *J. Appl. Crystallogr.* **12,** 374–378 (1979).

67. Wölfel, A. *Superstructures of magnetic materials* PhD thesis (University of Bayreuth, 2013).

68. Rothkirch, A. *et al.* Single-crystal diffraction at the Extreme Conditions beamline P02.2: procedure for collecting and analyzing high-pressure single-crystal data. *J. Synchrotron Radiat.* **20,** 711–720 (2013).

69. *Xcalibur/SuperNova CCD system, CrysAlisPro Software system, Version 1.171.37.31* Agilent Technologies UK Ltd. (Oxford, UK, 2013).

70. Bykova, E. *Single-crystal X-ray diffraction at extreme conditions in mineral physics and material sciences* PhD thesis (University of Bayreuth, 2015).

71. Meyer, M. *Construction of a multi-purpose X-ray CCD detector and its implementation on a 4-circle kappa goniometer* PhD thesis (Faculté des Sciences de l'Université de Lausanne, 1998).

72. Duisenberg, A. J. M. Indexing in single-crystal diffractometry with an obstinate list of reflections. *J. Appl. Crystallogr.* **25,** 92–96 (1992).

73. *International Tables for Crystallography Vol. F, first edition* (eds Rossmann, M. & Arnold, E.) (Kluwer Academic Publishers, Dordrecht, 2001).

74. Blessing, R. H. Outlier Treatment in Data Merging. *J. Appl. Crystallogr.* **30,** 421–426 (1997).

75. Friese, K., Grzechnik, A., Posse, J. M. & Petricek, V. Refinement of high pressure single-crystal diffraction data using Jana2006. *High Pressure Res.* **33,** 196–201 (2013).

76. McMahon, M. I. in *Advanced X-ray crystallography* 69–109 (Springer-verlag Berlin, 2012).

77. Pasternak, M. P. *et al.* Pressure-Induced Metallization and the Collapse of the Magnetic State in the Antiferromagnetic Insulator NiI_2. *Phys. Rev. Lett.* **65,** 790–793 (1990).

78. Patterson, J. R. *et al.* Pressure-induced metallization of the Mott insulator MnO. *Phys. Rev. B* **69,** 220101(R) (2004).

79. Takano, M. *et al.* Pressure-induced high-spin to low-spin transition in $CaFeO_3$. *Phys. Rev. Lett.* **67,** 3267–3270 (1991).

80. Chen, X.-J. *et al.* Enhancement of superconductivity by pressure-driven competition in electronic order. *Nature* **466,** 950–953 (2010).

81. Manjón, F. J. & Errandonea, D. Pressure-induced structural phase transitions in materials and earth sciences. *Phys. Status Solidi B* **246,** 9–31 (2009).

82. Dera, P., Nisar, J., Ahuja, R., Tkachev, S. & Prakapenka, V. B. New type of possible high-pressure polymorphism in NiAs minerals in planetary cores. *Phys. Chem. Miner.* **40,** 183–193 (2012).

83. Sowa, H., Steurer, W. & de Boer, J. L. Pressure-induced phase transitions in Mo_8O_{23}. *Phase Transitions* **47,** 1–8 (1994).

84. Palmer, D. C. & Finger, L. W. Pressure-induced phase transition in cristobalite: an X-ray powder diffraction study to 4.4 GPa. *Am. Mineral.* **79,** 1–8 (1996).

85. Janssen, T., Ghapuis, G. & de Boissieu, M. *Aperiodic Crystals. From Modulated Phases to Quasicrystals* (Oxford University Press, 2007).

86. Wagner, T. & Schönleber, A. A non-mathematical introduction to the superspace description of modulated structures. *Acta Crystallogr. B* **65,** 249–268 (2009).

87. Palatinus, L. & Chapuis, G. SUPERFLIP a computer program for the solution of crystal structures by charge flipping in arbitrary dimensions. *J. Appl. Crystallogr.* **40,** 786–790 (2007).

88. Petricek, V., Dusek, M. & Palatinus, L. *Jana 2006. The crystallographic computing system* Institute of Physics (Praha, Czech Republic, 2006).

89. Schreurs, A. M. M., Xian, X. & Kroon-Batenburg, L. M. J. EVAL15: a diffraction data integration method based on ab initio predicted profiles. *J. Appl. Crystallogr.* **43,** 70–82 (2009).

90. Perez-Mato, J. M. *et al.* Apparently Complex High-Pressure Phase of Gallium as a Simple Modulated Structure. *Phys. Rev. Lett.* **97,** 115501 (2006).

91. Pérez-Mato, J. M., Orobengoa, D. & Aroyo, M. I. Mode crystallography of distorted structures. *Acta Crystallogr. A* **66,** 558–590 (2010).

92. Schönleber, A., Meyer, M. & Chapuis, G. NADA – a computer program for the simultaneous refinement of orientation matrix and modulation vector(s). *J. Appl. Crystallogr.* **34,** 777–779 (2001).

93. Stokes, H. T., Campbell, B. J. & van Smaalen, S. Generation of $(3 + d)$-dimensional superspace groups for describing the symmetry of modulated crystalline structures. *Acta Crystallogr. A* **67,** 45–55 (2011).

94. van Smaalen, S., Campbell, B. J. & Stokes, H. T. Equivalence of superspace groups. *Acta Crystallogr. A* **69,** 75–90 (2013).

95. *International Tables for Crystallography Vol. A, fifth edition* (ed Hahn, T.) (Kluwer Academic Publishers, Dordrecht, 2002).

96. Kuntscher, C. A. *et al.* Pressure-induced metallization and structural phase transition of the Mott-Hubbard insulator TiOBr. *Phys. Rev. B* **76,** 241101 (2007).

97. Kuntscher, C. A., Klemm, M., Horn, S., Sing, M. & Claessen, R. Possible metallization of the Mott insulators TiOCl and TiOBr: Effects of doping and external pressure. *Eur. Phys. J. Special Topics* **180,** 29–42 (2010).

98. Prodi, A., Helton, J. S., Feng, Y. & Lee, Y. S. Pressure-induced spin-Peierls to incommensurate charge-density-wave transition in the ground state of TiOCl. *Phys. Rev. B* **81,** 201103 (2010).

99. Zhang, Y.-Z., Opahle, I., Jeschke, H. O. & Valentí, R. Pressure-driven phase transitions in TiOCl and the family $(Ca,Sr,Ba)Fe_2As_2$. *J. Phys. Condens. Matter* **22,** 164208 (2010).

100. Kim, S.-H., Kang, J.-K., Hwang, S. & Kim, H. A theoretical study on the electronic structures of MOCl (M = Ti, V and Fe) and their relationship wih physical properties. *Bull. Korean Chem. Soc.* **16,** 299–304 (1995).

101. Bringley, J. F., Fabre, J.-M. & Averill, B. A. Intercalation of bis(ethylenedithio) tetrathiafulvalene (ET) into iron oxychloride: a highly conducting low-dimensional system. *J. Am. Chem. Soc.* **112,** 4577–4579 (1990).

102. Sagua, A. *et al.* Lithium intercalation in FeOCl revisited. *Int. J. Inorg. Mater.* **3,** 293–301 (2001).

103. Doudin, B. & Heine, V. The origin of the gamma incommensurate structure in n-propylammonium tetrachlorometallates. *J. Phys. Condens. Matter* **2,** 3237–3246 (1990).

104. Hammersley, A. P., Svensson, S. O., Hanfland, M., Fitch, A. N. & Hausermann, D. Two-dimensional detector software: From real detector to idealised image or two-theta scan. *High Pressure Res.* **14,** 235–248 (1996).

105. Prescher, C., McCammon, C. & Dubrovinsky, L. S. MossA: a program for analyzing energy-domain Mössbauer spectra from conventional and synchrotron sources. *J. Appl. Crystallogr.* **45,** 329–331 (2012).

106. Klotz, S., Chervin, J.-C., Munsch, P. & Le Marchand, G. Hydrostatic limits of 11 pressure transmitting media. *J. Phys. D: Appl. Phys.* **42,** 075413 (2009).

107. Birch, F. Finite Elastic Strain of Cubic Crystals. *Phys. Rev.* **71,** 809–824 (1947).

108. Angel, R. J. Equations of state. *Rev. Mineral. Geochem.* **41,** 35–60 (2000).

109. Fausti, D. *et al.* Symmetry disquisition on the TiOX phase diagram (X = Br,Cl). *Phys. Rev. B* **75,** 245114 (2007).

110. Janssen, T., Janner, A., Looijenga-Vos, A. & de Wolff, P. M. in *International Tables for Crystallography Vol. C* (ed Prince, E.) 907–955 (Kluwer Academic Publishers, Dordrecht, 2006).

111. Lind, M. D. Refinement of the crystal structure of iron oxychloride. *Acta Crystallogr. B* **26,** 1058–1062 (1970).

112. Campbell, B. J., Stokes, H. T., Tanner, D. E. & Hatch, D. M. ISODISPLACE: a web-based tool for exploring structural distortions. *J. Appl. Crystallogr.* **39,** 607–614 (2006).

113. Dai, Y. D. *et al.* Mössbauer studies on the spiral antiferromagnetic coupling in iron oxychloride. *Chem. Phys. Lett.* **358,** 473–478 (2002).

114. Dusing, E. F., Grosshans, W. A. & Holzapfel, W. B. Equation of state of solid chlorine and bromine. *J. Phys.* **45,** 203–206 (1984).

115. Rozenberg, G. K. *et al.* Pressure-induced structural, electronic, and magnetic phase transitions in $FeCl_2$ studied by x-ray diffraction and resistivity measurements. *Phys. Rev. B* **79,** 214105 (2009).

116. Glawion, S. *et al.* Electronic structure of the two-dimensional Heisenberg antiferromagnet VOCl: A multiorbital Mott insulator. *Phys. Rev. B* **80,** 155119 (2009).

117. Schwarz, U. Metallic high-pressure modifications of main group elements. *Z. Kristallogr.* **219,** 376–390 (2004).

118. Gregoryanz, E. *et al.* Structural diversity of sodium. *Science* **320,** 1054–1057 (2008).

119. Loa, I., Nelmes, R. J., Lundegaard, L. F. & McMahon, M. I. Extraordinarily complex crystal structure with mesoscopic patterning in barium at high pressure. *Nat. Mater.* **11,** 627–632 (2012).

120. Guillaume, C. L. *et al.* Cold melting and solid structures of dense lithium. *Nat. Phys.* **7,** 211–214 (2011).

121. Neaton, J. & Ashcroft, N. Pairing in dense lithium. *Nature* **400,** 141–144 (1999).

122. Ravy, S. *et al.* High-pressure X-ray diffraction study of 1T-TaS$_2$. *Physica B* **407,** 1704–1706 (2012).

123. Ritschel, T. *et al.* Pressure dependence of the charge density wave in 1T-TaS$_2$ and its relation to superconductivity. *Phys. Rev. B* **87,** 125135 (2013).

124. Kedyulich, V. M, Slivka, A. G., Gerzanich, E. I. & Shusta, V. S. p,T,E - diagram of $Sn_2P_2S_6$ ferroelectric with high-pressure incommensurate phase. *Condens. Matter Phys.* **3,** 851–856 (2000).

125. Gesi, K. Effect of hydrostatic pressure on the lock-in transitions in tetramethylammonium tetrahalogenometallic compounds, $(N(CH_3)_4)_2XY_4$. *Ferroelectrics* **66,** 269–286 (1986).

126. Bykov, M., Bykova, E., Hanfland, M., Liermann, H.-P. & van Smaalen, S. Superspace approach to high pressure superstructures. *High Pressure Res.* **33,** 501–510 (2013).

127. Bykov, M. *et al.* High-pressure behavior of FeOCl. *Phys. Rev. B* **88,** 014110 (2013).

128. Moggach, S. A. & Parsons, S. High pressure crystallography of inorganic and organometallic complexes. *Spectrosc. Prop. Inorg. Organomet. Compd.* **40,** 324–354 (2009).

129. Allen, F. H. The Cambridge Structural Database: a quarter of a million crystal structures and rising. *Acta Crystallogr. B* **58,** 380–388 (2002).

130. Mínguez Espallargas, G. *et al.* Noncovalent interactions under extreme conditions: high-pressure and low-temperature diffraction studies of the isostructural metal-organic networks (4-chloropyridinium)$_2$[CoX$_4$] (X = Cl, Br). *J. Am. Chem. Soc.* **130,** 9058–9071 (2008).

131. González-Alvarez, M. *et al.* Comparison of protective effects against reactive oxygen species of mononuclear and dinuclear Cu(II) complexes with N-substituted benzothiazolesulfonamides. *Inorg. Chem.* **44,** 9424–9433 (2005).

132. Marchetti, F., Pampaloni, G. & Zacchini, S. The interaction of molybdenum pentachloride with carbonyl compounds. *Dalton Trans.* **42,** 2477–2487 (2013).

133. Hoang, N. N., Valach, F. & Dunaj-Jurco, M. Bis(2-chloro-6-fluorobenzoato)bis (nicotinamide)copper(II). *Acta Crystallogr. C* **51,** 1095–1097 (1995).

134. Lee, G.-H. *et al.* Heterostructures based on inorganic and organic van der Waals systems. *APL Mater.* **2,** 092511 (2014).

135. Petricek, V., Dusek, M. & Palatinus, L. Crystallographic Computing System JANA2006: General features. *Z. Kristallogr.* **229,** 345–352 (2014).

136. Merlini, M. & Hanfland, M. Single-crystal diffraction at megabar conditions by synchrotron radiation. *High Pressure Res.* **33,** 511–522 (2013).

137. Hess, N. J. & Schiferl, D. Comparison of the pressure-induced frequency shift of Sm:YAG to the ruby and nitrogen vibron pressure scales from 6 to 820 K and 0 to 25 GPa and suggestions for use as a high-temperature pressure calibrant. *J. Appl. Phys.* **71,** 2082 (1992).

138. *International Tables for Crystallography Vol. A1, second edition* (eds Wondratschek, H. & Müller, U.) (Kluwer Academic Publishers, Dordrecht, 2010).

139. Haase, A. & Brauer, G. Vanadium oxychloride. *Acta Crystallogr. B* **31,** 2521–2522 (1975).

140. Macovez, R. *et al.* Hybridization, superexchange, and competing magnetoelastic interactions in TiOBr. *Phys. Rev. B* **76,** 205111 (2007).

141. Bykov, M. *et al.* Spin-Peierls distortions in $TiPO_4$. *Phys. Rev. B* **88,** 184420 (2013).

142. Piñeiro, A. *et al.* Study of the pressure effects in TiOCl by ab initio calculations. *J. Magn. Magn. Mater.* **322,** 1072–1075 (2010).

143. Khomskii, D. I. *Transition Metal Oxides* (Cambridge University Press, 2014).

144. Pen, H., van den Brink, J., Khomskii, D. & Sawatzky, G. Orbital Ordering in a Two-Dimensional Triangular Lattice. *Phys. Rev. Lett.* **78,** 1323–1326 (1997).

145. Schmidt, M. *et al.* Spin Singlet Formation in $MgTi_2O_4$: Evidence of a Helical Dimerization Pattern. *Phys. Rev. Lett.* **92,** 056402 (2004).

146. Radaelli, P. G. *et al.* Formation of isomorphic Ir^{3+} and Ir^{4+} octamers and spin dimerization in the spinel $CuIr_2S_4$. *Nature* **416,** 155–158 (2002).

147. Dagotto, E. Complexity in Strongly Correlated Electronic Systems. *Science* **309,** 257–262 (2005).

148. Lee, P. A. From high temperature superconductivity to quantum spin liquid: progress in strong correlation physics. *Rep. Prog. Phys.* **71,** 012501 (2008).

149. Buzdin, A. I. & Bulaevskii, L. N. Spin-Peierls transition in quasi-one-dimensional crystals. *Sov. Phys. Usp.* **23,** 409–417 (1980).

150. Bray, J. W. *et al.* Observation of a Spin-Peierls Transition in a Heisenberg Antiferromagnetic Linear-Chain System. *Phys. Rev. Lett.* **35,** 744–747 (1975).

151. Jacobs, I. S. *et al.* Spin-Peierls transitions in magnetic donor-acceptor compounds of tetrathiafulvalene (TTF) with bisdithiolene metal complexes. *Phys. Rev. B* **14,** 3036–3051 (1976).

152. van Bodegom, B., Larson, B. C. & Mook, H. A. Diffuse x-ray and inelastic neutron scattering study of the spin Peierl's transition in N-methyl-N-ethyl-morpholinium bistetracyanoquinodimethane [MEM(TCNQ)$_2$]. *Phys. Rev. B* **24,** 1520 (1981).

153. Hase, M., Terasaki, I. & Uchinokura, K. Observation of the spin-Peierls transition in linear Cu^{2+} (spin-1/2) chains in an inorganic compound $CuGeO_3$. *Phys. Rev. Lett.* **70,** 3651–3654 (1993).

154. Richards, P. M. Critical temperatures of Heisenberg magnets by second-order Green's-function theory: Application to $S = \infty$ cubic lattices and quasi-one-dimensional systems. *Phys. Rev. B* **10,** 4687–4689 (1974).

155. Pisani, L., Valentí, R., Montanari, B. & Harrison, N. M. Density functional study of the electronic and vibrational properties of TiOCl. *Phys. Rev. B* **76,** 235126 (2007).

156. Palatinus, L., Schönleber, A. & van Smaalen, S. The twofold superstructure of titanium(III) oxybromide at T = 17.5 K. *Acta Crystallogr. C* **61,** i47–i48 (2005).

157. Schönleber, A., Shcheka, G. & van Smaalen, S. Normal-to-incommensurate phase transition in the spin-Peierls compound TiOCl: An x-ray diffraction study. *Phys. Rev. B* **77,** 094117 (2008).

158. van Smaalen, S., Palatinus, L. & Schönleber, A. Incommensurate interactions and nonconventional spin-Peierls transition in TiOBr. *Phys. Rev. B* **72,** 020105(R) (2005).

159. Rückamp, R. *et al.* Zero-Field Incommensurate Spin-Peierls Phase with Interchain Frustration in TiOCl. *Phys. Rev. Lett.* **95,** 097203 (2005).

160. Glaum, R., Reehuis, M., Stüßer, N., Kaiser, U. & Reinauer, F. Neutron Diffraction Study of the Nuclear and Magnetic Structure of the $CrVO_4$ Type Phosphates $TiPO_4$ and VPO_4. *J. Solid State Chem.* **126,** 15–21 (1996).

161. Wright, J. P., Attfield, J. P., David, W. I. F. & Forsyth, J. B. High-resolution powder neutron diffraction study of helimagnetic order in $CrP_{1-x}V_xO_4$ solid solutions. *Phys. Rev. B* **62,** 992–997 (2000).

162. Attfield, J. P., Battle, P. D. & Cheetham, A. K. The spiral magnetic structure of β-chromium(III) orthophosphate (β-$CrPO_4$). *J. Solid State Chem.* **57,** 357–361 (1985).

163. Battle, P. D., Gibb, T. C., Hu, G., Munro, D. C. & Attfield, J. P. The magnetic properties of the high pressure phase of ferric phosphate, $FePO_4$-II. *J. Solid State Chem.* **65,** 343–350 (1986).

164. Isasi, M. J., Sáez-Puche, R., Veiga, M. L., Pico, C. & Jerez, A. Synthesis and magnetic properties of crystalline $CrVO_4$. *Mater. Res. Bull.* **23,** 595–601 (1988).

165. Koo, H.-J., Whangbo, M.-H. & Lee, K.-S. Investigation of the Spin Exchange Interactions and Magnetic Structures of the $CrVO_4$-type Transition Metal Phosphates, Sulfates, and Vanadates by Spin Dimer Analysis. *Inorg. Chem.* **42,** 5932–5937 (2003).

166. Law, J. M. *et al.* Quasi-one-dimensional antiferromagnetism and multiferroicity in $CuCrO_4$. *Phys. Rev. B* **84,** 014426 (2011).

167. Kinomura, N., Muto, F. & Koizumi, M. Preparation of transition metal orthophosphates, MPO_4, and their magnetic properties. *J. Solid State Chem.* **45,** 252–258 (1982).

168. Glaum, R. & Gruehn, R. Beitrage zum thermischen Verhalten wasserfreier Phosphate. *Z. Kristallogr.* **198,** 41–47 (1992).

169. Law, J. M. *Identification and investigation of new low-dimensional quantum spin systems* PhD thesis (Loughborough University, 2011).

170. Braden, M. *et al.* Structural analysis of $CuGeO_3$: Relation between nuclear structure and magnetic interaction. *Phys. Rev. B* **54,** 1105 (1996).

171. Glaum, R. & Hitchman, M. A. On the Bonding Behaviour of Transition Metal Ions in Inorganic SolidsOptical and EPR Spectroscopic Studies on Anhydrous Phosphates and Phosphate-Silicates of Ti^{3+}. *Aust. J. Chem.* **49,** 1221–1228 (1996).

172. Kresse, G. & Hafner, J. *Ab initio* molecular dynamics for liquid metals. *Phys. Rev. B* **47,** 558(R) (1993).

173. Kresse, G. & Furthmüller, J. Efficiency of *ab initio* total energy calculations for metals and semiconductors using a plane-wave basis set. *Comput. Mater. Sci.* **6,** 15–50 (1996).

174. Kresse, G. & Furthmüller, J. Efficient iterative schemes for ab initio total-energy calculations using a plane-wave basis set. *Phys. Rev. B* **54,** 11169–11186 (1996).

175. Perdew, J. P., Burke, K. & Ernzerhof, M. Generalized Gradient Approximation Made Simple. *Phys. Rev. Lett.* **77,** 3865 (1996).

176. Dudarev, S. L., Botton, G. A., Savrasov, S. Y., Humphreys, C. J. & Sutton, A. P. Electron-energy-loss spectra and the structural stability of nickel oxide: An LSDA+U study. *Phys. Rev. B* **57,** 1505 (1998).

177. Angel, R. J, Alvaro, M. & Gonzalez-Platas, J. EosFit7c and a Fortran module (library) for equation of state calculations. *Z. Kristallogr.* **229,** 405–419 (2014).

178. Forsberg, H.-E. On the Structure of CrOCl. *Acta Chem. Scand.* **16,** 777 (1962).

179. Rotter, M., Muller, H., Gratz, E., Doerr, M. & Loewenhaupt, M. A miniature capacitance dilatometer for thermal expansion and magnetostriction. *Rev. Sci. Instrum.* **69,** 2742–2746 (1998).

Acknowledgements

First of all, I would like to thank my supervisor Prof. Dr. Sander van Smaalen who patiently guided my work and life during the PhD period. I would like to thank my dear wife Elena Bykova, who supported me not only as a wife, but also made a lot of effort to make my experiments feasible. This work would not be possible without the efforts of Alfred Suttner, who has synthesized perfect crystals of transition metal oxychlorides. I would like to thank Prof. Dr. Leonid Dubrovinsky, who kindly shared his ideas, equipment and synchrotron beam times with me.

Meinen besonderen Dank möchte ich gegenüber Privat Dozent Dr. Andreas Schönleber ausdrücken, welcher mein Lehrer für aperiodische Kristallographie war und der mich immer, während meiner gesamten Zeit am Lehrstuhl für Kristallographie, ermutigt hat an meinem Projekt weiter zu arbeiten.

Many thanks to Prof. Dr. Natalia Dubrovinskaia for her class "Physical properties of materials", which helped me a lot in entering the mysterious world of materials science. I can not imagine my stay in Bayreuth without the assistance of Denise Kelk-Huth. Apart from doing a tremendous everyday paperwork, she helped me in arranging my life in Bayreuth.

I would like to thanks all colleagues from the Laboratory of Crystallography and from the Bavarian Geoinstitute Franz Fischer, Alexander Wölfel, Jian Zhang, Leila Noohinejad, Swastik Mondal, Somnath Dey, Prathapa Siriyara Jagannatha, Imran Sk Ali, Christian Hübschle, Leyla Ismailova, Natalia Solopova, Ines Collings, Guoming Hao, Jeanette Held, Gleb Parakhonskiy, Ilya Kupenko, Alexander Kurnosov, Svyatoslav Shcheka, Clemens Prescher, Catherine McCammon, Valerio Cerantola for a nice working atmosphere, help with experiments and useful discussions.

Publications

Parts of this thesis published in the scientific literature or will be submitted for publication:

Chapter 4:
M. Bykov, E. Bykova, M. Hanfland, H.-P. Liermann, and S. van Smaalen. Superspace approach to high-pressure superstructures. *High Press. Res.* **33**, 501 (2013).

Chapter 5:
M. Bykov, E. Bykova, S. van Smaalen, L. Dubrovinsky, C. McCammon, V. Prakapenka, and H.-P. Liermann. High-pressure behavior of FeOCl. *Phys. Rev. B* **88**, 014110 (2013).

Chapter 6:
M. Bykov, E. Bykova, L. Dubrovinsky, M. Hanfland, H.-P. Liermann and Sander van Smaalen. Pressure-induced normal-incommensurate and incommensurate-commensurate phase transitions in CrOCl. *submitted to Scientific Reports*

Chapter 7:
M. Bykov, E. Bykova, L. Dubrovinsky, M. Hanfland, and Sander van Smaalen. Pressure-induced phase transitions in MOCl (M = Sc, V, Ti). *to be submitted to Phys. Rev. Lett.*

Chapter 8:
M. Bykov, J. Zhang, A. Schonleber, A. Wölfel, S.I. Ali, S. van Smaalen, R. Glaum, H.-J. Koo, M.-H. Whangbo, P.G. Reuvekamp, J.M. Law, C. Hoch, and R.K. Kremer. Spin-Peierls distortions in $TiPO_4$. *Phys. Rev. B* **88**, 184420 (2013).

Erklärung

Hiermit versichere ich an Eides statt, dass ich die vorliegende Arbeit selbstständig verfasst und keine anderen als die von mir angegebenen Quellen und Hilfsmittel verwendet habe. Zusätzlich erkläre ich hiermit, dass ich keinerlei frühere Promotionsversuche unternommen habe. Weiterhin erkläre ich, dass ich die Hilfe von gewerblichen Promotionsberatern bzw. -vermittlern oder ähnlichen Dienstleistern weder bisher in Anspruch genommen habe, noch künftig in Anspruch nehmen werde.

Maxim Bykov

Bayreuth, den 20.01.2015